Laboratory and Field Studies of Oblique Rifting

by

Amy E. Clifton

A Dissertation submitted to the

Graduate School-New Brunswick

Rutgers, The State University of New Jersey

in partial fulfillment of the requirements

for the degree of

Doctor of Philosophy

Graduate Program in Geological Sciences

written under the direction of

Dr. Roy W. Schlische

and approved by

_____

_____

_____

_____

_____

New Brunswick, New Jersey

May, 2000

ABSTRACT OF THE DISSERTATION

Laboratory and Field Studies of Oblique Rifting

By Amy E. Clifton

Dissertation Director:

Dr. Roy W. Schlische

This thesis examines the manner in which fault population systematics vary as a function of rift obliquity and how fault populations evolve through time in oblique rift zones. Rift obliquity is related to the acute angle, α, between the rift trend and the displacement direction of the rift walls, so that the value of α is inverse to the degree of obliquity. I used scaled experimental models to simulate fault growth in oblique rift zones and analyzed photographs of the model surfaces to determine their fault population statistics. First I examined a single displacement increment for a whole suite of models where α is varied in 15° increments between 90° and 0°. Results show increases in the range of azimuths as rift obliquity increases; the length of the longest faults, the sum of fault lengths, and the width of the deformed zone all increase as rift obliquity decreases. Major changes in fault population statistics occur between α = 45° and 30°, when the stress state changes from both horizontal stresses being tensional to one becoming compressional. Next I used scaled clay models to study the temporal evolution of fault populations in experiments of moderately oblique (α= 60°) and highly oblique (α= 30°)

conditions, with CAI formation earlier and in more restricted regions of the nebula and chondrule formation later and more widespread.

Acknowledgements and Dedication

Completion of this thesis would not have been possible without the always careful and caring guidance of Roy W. Schlische. I thank Roy for drawing me to Rutgers, encouraging me to pursue my own interests during the development of this project and supporting me every step of the way. I am especially grateful to Roy for traveling with me to Iceland for three weeks of intense field work on Reykjanes Peninsula, for introducing me to Martha Withjack and for teaching me the art of experimental clay modeling. Roy, I can't thank you enough for all you have done for me these past three and a half years. Thank you for providing me with confidence-boosting pep talks when they were needed most. Thank you most of all for being a wonderful human being and a good friend. I look forward to continued collaborative work with you as my professional career progresses.

I would like to thank the Rutgers members of my committee for supporting and encouraging me from the very beginning of this project. In particular, I thank Peter Rona for informing me about the RIDGE/NORDVULK Summer School on Mid-Ocean Ridge Processes and for always making sure I was thinking about the right questions concerning mid-ocean ridges. I thank Martha Withjack for sharing with me just a little of her extensive knowledge about experimental modeling and oblique rifting, for arranging my use of the Mobil modeling laboratory, for providing a role model as a successful and competent woman geologist, for showing me the Witchita Mountains of Oklahoma and for being a supportive friend and colleague. Special thanks go to Mike Carr for acting as my surrogate advisor during Roy's sabbatical year, for encouraging me in my

volcanological pursuits, for always providing concise and honest constructive criticism, for cheering me on in his own mysterious and subtle way, and for being a friend. Mike, I am truly honored to have earned your respect and support. Thank you.

During the past year, Freysteinn Sigmundsson has played an instrumental role in the completion of this thesis and in helping me to chart the future course of my career. Freysteinn, thank you for teaching me to look at the Reykjanes Peninsula in a new way and for providing me with such a welcoming environment in which to work. Your input has been invaluable and your confidence in me has made the last stages of this project just a little easier to bear.

I would like to thank the entire faculty of the Department of Geological Sciences at Rutgers, New Brunswick for providing an atmosphere of collegiality and scientific excellence in which to work. You have shown me that it is possible for a diverse group of scientists to be supportive of each other and to find myriad ways to do collaborative work without the fierce sense of competition that is all too common in the world of scientific research. It has been an honor and a pleasure to be part of this department for three and a half years and I owe you my gratitude for that. Special thanks are owed to Delores Daley who always looked after me and made sure things were going smoothly. Thanks Dee and Charlotte Holland for assisting me with grant proposals and filling out forms and for always being so friendly and helpful.

Thanks are owed to the (former) Mobil Technology Company for allowing me access to their modeling laboratory in Farmer´s Branch, Texas. Thanks to Gloria Eisenstadt for sharing some of her time in the lab. Thanks to the American Association of Petroleum Geologists, Geological Society of America and Sigma Xi for providing

financial support for two seasons of field work in Iceland. Thanks also to the National Science Foundation for their support. Thanks to the U.S. Fulbright Commission for bringing me to Iceland for these last six months, and to Stella Hálfdánarsdóttir, director of the Icelandic Fulbright Office, for smoothing the way for me here.

Many people have helped to improve the quality of this thesis. Special thanks go to Karen Bemis for the countless hours she has spent with me discussing statistical and analytical methods, for teaching me the secrets of Microsoft Excel, and for assisting me in the use of MatLab. Thank you for the long walks we took and for being a valuable and supportive friend. I am eternally grateful for that and more. Thanks go to Rolf Ackermann for encouraging me to apply to Rutgers in the first place, and for the many hours we spent discussing fault populations, experimental modeling and life as a grad student. Thanks as well for the time you spent teaching and helping me in the modeling lab in Dallas and for providing a comfortable and welcoming place to stay while performing the modeling experiments. Jaime Whitlock has earned my gratitude for being an outstanding field assistant and wonderful companion during three difficult weeks of field work on Reykjanes Peninsula. Jaime, thanks for your keen eyes and unending stamina, and for singing with me in the pouring rain. Thanks are owed to Kristján Sæmundsson for providing a vehicle for my use during two summer field seasons in Iceland and for sharing his knowledge of Reykjanes Peninsula. Thanks as well to Gunna and Lilja at Farfuglaheimalið Strönd in Innri-Njarðvík, for providing a comfortable place to live during those two summers and for giving me my first lessons in Icelandic. Ég tala Íslensku núna. Thanks to Professor Robert Berk of the Department of Statistics at Rutgers for taking the time to help me begin to understand the many implications and aspects of

cumulative frequency distributions. Thanks also to Jyhming Shoung for the time he spent struggling with my cumulative frequency data.

Many people deserve thanks for helping me keep my sanity at Rutgers. Thanks to Lina Patino for helping me through the first rough year back in grad school and for a friendship that provides constant intellectual stimulation and comraderie. Thanks to Tim Reilly for a special friendship that I will always value. Thanks to Dan Deocampo, Ben Cramer, Steph Gaswirth, and Cindy Liutkus for accepting me as a friend and for enjoyable nights at Doll´s Place. Special thanks to Gabriela Hristescu for her support and friendship and for being the best roommate ever for two years in a row.

Thank you to all of my friends and colleagues at the Nordic Volcanological Institute in Reykjavik, for making me feel at home in Iceland and for supporting me and cheering me on as I approached the "finish line". Special thanks to Anna Eíriksdóttir for being my Christmas angel and my good friend.

Several friends deserve special thanks for encouraging me to begin this most recent journey. Thanks to Martha Brackeen-Harris, Gretchen Hathaway, Beverly Fitzsousa and Pat Clark for believing in me long before I believed in myself.

Finally, thanks to all of the members of my family who helped me in so many ways, big and small, tangible and intangible, over these past four years since my return to school. To my sons, Simon and Benjamin, thanks for your understanding and love. You are my gold. To my father, Simon, thanks for hanging in there and cheering me on. To my sisters, Lucy and Elvy, I hope you know how grateful I am for everything you have done to help me. Thank you for being there. To Lee, Dennis, Allie, Jess, Jen, Julia,Mari, Matt, Curt and baby Jessie. I love you all.

This dissertation is dedicated to two very special people. To my mother, Sophie Stepinoff, who taught me the most important things in life. Mom, I feel your presence always. To my dear friend Kirby, the catalyst who set this work in motion. You showed me the wonders of Iceland and inspired me to follow my dream. Your friendship and support has meant so much to me.

Table of Contents

Abstract.....ii

Acknowledgements and Dedication.....iiii

List of Tables.....xii

List of Illustrations.....xiii

Chapter 1 - Influence of rift obliquity on fault-population systematics: results of experimental clay models.....1

1.1. Abstract.....1

1.2. Introduction.....2

1.3. Experimental Procedure.....4

1.4. Data collection.....5

1.5. Data.....8

1.5.1. Description of fault trace maps.....8

1.5.2. Fault geometry.....9

1.5.3. Spatial pattern of faults.....10

1.5.4. Fault-related strain.....12

1.5.5. Fault length.....13

1.5.6. Cumulative Frequency of lengths.....15

1.6. Discussion.....17

1.6.1. Fault linkage.....17

1.6.2. Spatial pattern of faults.....18

1.6.3. Cumulative frequency distribution.....20

1.6.4 . Geological examples: continental rifts.....21

1.6.5 . Geological examples: oblique mid-ocean ridge segments 22

1.7. Summary and Conclusions.....25

Chapter 2 - Nucleation, growth and linkage of faults in oblique rift zones: results from experimental clay models.....49

2.1. Abstract.....49

2.2. Introduction.....49

2.3. Methods.....51

2.4. Data.....53

2.4.1. $\alpha = 60°$.....53

2.4.2. $\alpha = 30°$.....54

2.5. Discussion: Comparison of two models.....56

2.5.1. Fault nucleation.....56

2.5.2. Fault growth.....57

2.6. Summary and conclusions.....60

Chapter 3 – Population systematics of fractures on the Reykjanes Peninsula, Iceland: comparison with experimental clay models of oblique rifting.....76

3.1. Abstract.....76

3.2. Introduction.....76

3.3. Tectonic Setting and Geologic Background.....79

3.4. Previous Work.....82

3.5. Data collection.....83

3.5.1. Air photos.....83

3.5.2. Field data.....85

3.6. Data.....86

3.6.1. Geological Descriptions.....86

3.6.1.1.Vogar.....86

3.6.1.2. Grindavik.....88

3.6.1.3. Stora-Sandvik/Reykjanes.....88

3.6.2. Fracture azimuth.....91

3.6.3. Fracture density.....92

3.6.4. Fracture length distribution.....93

3.6.5. Segment length.....94

3.7. Comparison with models.....95

3.7.1. Large-scale spacing of fissure swarms.....95

3.7.2 Spatial distribution of fractures.....97

3.8. Discussion.....102

3.9. Summary and Conclusions.....106

Epilogue.....137

Appendix A.....140

Bibliography.....142

Curriculum Vita.....151

Lists of tables

Table 1. Differences between experimental model and Reykjanes Peninsula.....109

List of illustrations

Fig. 1.1. (a) Experimental apparatus. (b) Detail of apparatus surface.....28

Fig. 1.2. Photographs of model surfaces showing lighting conditions.....29

Fig. 1.3. Fault trace maps for all models.....30

Fig. 1.4. Criteria for identifying segment boundaries.....31

Fig. 1.5. Histograms of fault azimuth for all models.....32

Fig. 1.6. Fault length vs. azimuth for all models.....33

Fig. 1.7. Variation in width of the deformed zone with α.....34

Fig. 1.8. Bar graph of mean fault spacing and standard deviation of fault spacing.....35

Fig. 1.9. Examples of map patterns with different fractal dimensions.....36

Fig. 1.10. Graph of the capacity dimension (D_c) and information dimension (D_i) as a function of α.....37

Fig. 1.11. Graph showing how imposed extensional strain compares with fault related strain for $\alpha \geq 45°$.....38

Fig. 1.12. (a) Diagram showing hanging-wall and footwall cutoffs along a segmented fault. (b) Diagram defining fault tortuosity 39

Fig. 1.13. Variation of average tortuosity with α.....40

Fig. 1.14. Graphs showing how (a) the length of the fault at the 95th percentile of lengths (b) summed fault length and (d) number of faults vary with α. (c) summed fault length per unit area. e) number of faults per unit area.....41

Fig. 1.15. Graphs showing cumulative frequency of lengths for whole faults and for fault segments.....42

Fig. 1.16. Graph showing variation in characteristic length (L_c) with α for whole faults and fault segments.....43

Fig. 1.17. Graph showing how imposed extensional strain at the base of the model varies with α at different displacement increments during fault population evolution.....44

Fig. 1.18. Detail from a photograph of the α=45° model showing the zone of complex faulting that forms where dip domains of opposite polarity meet.....45

Fig. 1.19. Location map showing field examples of oblique rift zones.....46

Fig. 1.20. Comparison of map patterns of faults in oblique continental rift basins with fault trace map of our clay model.....47

Fig. 1.21. Comparison of map patterns of faults on oblique mid-ocean ridge segments with fault trace maps of our clay models.....48

Fig. 2.1. Fault trace maps for α = 60°.....62

Fig. 2.2. Enlarged view of fault growth and linkage for α = 60° model between 2.5 and 3.5 cm of displacement.....64

Fig. 2.3. Histograms of azimuths for α = 60° models.....65

Fig. 2.4. Plots of length vs. azimuth for α = 60° models.....66

Fig. 2.5. Fault trace maps for α = 30° models.....67

Fig. 2.6. Histograms of azimuths for α = 30° models.....69

Fig. 2.7. Enlarged view of fault growth and linkage for α = 30° model between 1.75 and 3.5 cm of displacement.....70

Fig. 2.8. Plots of length vs. azimuth for α = 30° models.....71

Fig. 2.9. Summary plot showing how the number of faults changes in each model with

increasing displacement.....72

Fig. 2.10. a) Summary plot showing how the summed length of faults changes through time in each model. b) Summary plot showing how the 95th percentile of lengths changes with increasing displacement in each model.....73

Fig. 2.12. Summary plot showing how tortuosity changes with increasing displacement in each model.....74

Fig. 2.13. Cartoon demonstrating the style of fault growth in each model.....75

Fig. 3.1. a) Map showing the location of Iceland along the Mid-Atlantic Ridge. b) Map showing the geometry of ridge segments on Iceland.....110

Fig. 3.2. Tectonic map of Reykjanes Peninsula.....111

Fig. 3.3. Volcanic systems of Reykjanes Peninsula.....112

Fig. 3.4. Shaded Digital Elevation Model of Reykjanes Peninsula.....113

Fig. 3.5. Map of Reykjanes Fissure Swarm, showing field locations from this study....114

Fig. 3.6. Histograms of azimuth for structures in the Reykjanes Fissure Swarm.....115

Fig. 3.7. Criterion used during field mapping at Molvik to distinguish an ordinary cooling joint from a tectonic fracture.....116

Fig. 3.8. Fracture trace map for the Vogar photomosaic.....117

Fig. 3.9. Air photo sub-image of normal fault in the southwestern part of the Vogar photomosaic.....118

Fig. 3.10. a) Field photo and b) air photo sub-image of fracture in the northeastern part of the Vogar photomosaic.....119

Fig. 3.11. Fracture trace map for the Grindavik photomosaic.....120

Fig. 3.12. a) Field photo of a typical normal fault in the area covered by the Grindavik

photomosaic. b) Air photo sub-image from the Grindavik photomosiac showing a typical array of fissures.....121

Fig. 3.13. Fracture trace map for the Stora-Sandvik/Reykjanes photomosaic.....122

Fig. 3.14. a) Field photo and b) air photo sub-image of complex interaction between normal fault striking 080° and graben structure striking 040° at Stora-Sandvik.....123

Fig. 3.15. a) Map of right lateral oblique-slip fault at Reykjanes. b) Sub-image from Stora-Sandvik/Reykjanes air photo showing segments 2 and 3 from map. c) Map of strike-slip fault in SISZ showing right-lateral offset of 2.4 m.....124

Fig. 3.16. Histograms of azimuth for data from air photos and $\alpha = 30°$ model.....125

Fig. 3.17. Plots of length vs. azimuth for data from air photos.....126

Fig. 3.18. a) Histogram of azimuths for data from Molvik. b) Plot of length vs. azimuth for data from Molvik. c) Histogram of azimuth for fractures at Molvik greater than 4 meters in length.....127

Fig. 3.19. Graph showing fracture spacing and standard deviation of fracture spacing for the Vogar photomosaic.....128

Fig 3.20. Log-log plots of cumulative frequency of fracture lengths for data from air photos and field data.....129

Fig. 3.21. Plot of segment length vs. total fracture length for the three longest fractures on each air photo.....130

Fig. 3.22. Tectonic map of Reykjanes Peninsula and fault trace map for $\alpha = 30°$ after 2.5 cm of displacement and rotated 15° clockwise.....131

Fig. 3.23. Fault trace maps for the $\alpha = 30°$ model showing clustering.....132

Fig. 3.24. Summary of tectonic trends for the $\alpha = 30°$ model and Reykjanes Peninsula.....133

Fig. 3.25. Close-up of flexure forming in the $\alpha = 30°$ model.....134

Fig. 3.26. Detail from fault trace maps for the $\alpha = 30°$ model between 2.25 and 3.5 cm of displacement.....135

Fig. 3.27. Photograph of a) a thin fissure-erupted lava flow (approximately 2000 ybp) and b) a thick pahoehoe flow from the Sandfellshaed shield (approximately 12,500 ybp), both cut by a northeast striking normal fault.....136

Chapter 1 - Influence of rift obliquity on fault-population systematics: results of experimental clay models[1]

1.1. Abstract

We use clay models to simulate how fault population systematics vary as a function of rift obliquity. Rift obliquity is related to the acute angle, α, between the rift trend and the displacement direction, so that the value of α is inverse to the degree of obliquity. The range of azimuths in a fault population increases as rift obliquity increases (i.e., as α decreases). The length of the longest faults, the sum of fault lengths, and the width of the deformed zone all increase as rift obliquity decreases (i.e., as α increases). The majority of faults in our models are segmented and have highly tortuous traces. Tortuosity is maximum when $\alpha = 30°$ as segments of widely varying azimuth link during fault growth. Significant changes occur in the fault patterns between $\alpha = 30°$ and $\alpha = 45°$. At $\alpha = 30°$ two fault populations of equal importance develop in the center of the rift zone, one approximately rift-parallel and the other displacement-normal. Between $\alpha = 30°$ and 45°, the number of faults more than doubles, and between $\alpha = 45°$ and 60°, summed fault length more than doubles. Fault patterns for all models are fractal, with fractal dimensions that increase with increasing α and that are comparable to those found in the field. Fault populations are not multi-fractal because the cumulative frequency distributions of fault lengths do not generally follow a power-law relationship. An exponential distribution best describes the data for whole faults, with the characteristic length increasing with increasing α. Segment lengths also follow an exponential

---

[1] This chapter is excerpted from Clifton, A.E., Schlische, R.W., Withjack, M.O. and Ackermann, R.V., 2000, Influence of rift obliquity on fault-population systematics: results of experimental clay models. Journal of Structural Geology (in press).

distribution with characteristic length varying very little with α. The fault patterns in our models resemble the spatial pattern of brittle deformation observed at oblique mid-ocean ridge segments and are similar in geometry to those in oblique continental rift basins. At the rift margins, tensional stresses are modulated and reoriented by a secondary stress field related to a change in boundary conditions, resulting in the formation of two distinct sub-populations of faults during oblique rifting.

1. 2. Introduction

During the past 10 years, numerous studies have led to a new and better understanding of how faults grow and how fault populations evolve in extensional tectonic settings (Cowie and Scholz, 1992; Cowie et al., 1993a; Dawers, 1996; Ackermann and Schlische, 1997; Ackermann et al., 1997; Cowie, 1998a). Most previous studies have focused on simple orthogonal extension in order to determine the basic mechanical processes at work during fault population evolution. This study applies many of the same techniques to oblique extension. With oblique extension, the trend of the deformed zone (referred to hereafter as rift trend) is oblique to the displacement direction. The acute angle, α, between the rift trend and the displacement is inversely related to the degree of obliquity, so that a highly oblique rift has a low value of α (Fig.1.1) (Withjack and Jamison, 1986).

Quantifying brittle deformation during oblique extension is important to understand how fracture populations evolve in a range of tectonic settings. Rift basins commonly localize along a pre-existing tectonic fabric that is oriented obliquely to the absolute displacement direction (e.g., Lindholm, 1978; Angelier and Bergerat, 1983;

Morley, 1995). Changes in the direction of plate motion may also impose oblique spreading on mid-ocean ridge segments (e.g., Dauteuil and Brun, 1993). Field studies in both continental and ocean-ridge environments describe a complex interaction between displacement-normal and rift-parallel structures in oblique rift zones such as the Gulf of California (Withjack and Jamison, 1986; Umhoefer and Stone, 1996), the Gulf of Aden (Withjack and Jamison, 1986), the Hartford basin of eastern North America (Clifton, 1987; DeBoer and Clifton, 1988), the Malawi rift of east Africa (Chorowicz and Sorlein, 1992), the Reykjanes ridge south of Iceland (Murton and Parson, 1993; McAllister et al., 1995), the Mohns Ridge north of Jan Mayen (Dauteuil and Brun, 1996), and several grabens in the northern North Sea (Færseth et al., 1997). In rifts oriented sub-perpendicular to the displacement direction, some fault populations have a fractal scaling that can be described by a power-law size distribution (Cowie et al., 1993b). Studies by Hatton et al. (1994) and Ackermann et al. (1997) indicate a lower and upper limit to fractal scaling, respectively. Preliminary work on experimental models of oblique extension suggest that the size distribution of faults varies with α (Clifton and Schlische, 1997; Clifton et al., 1998).

Although they are not perfectly scaled reproductions of geological conditions (e.g. they are relatively homogeneous and isotropic whereas rock is relatively heterogenous and anisotropic), results from analyses of experimental models can be used to guide and support real world investigations. Experimental models are ideal for studying oblique extension because the boundary conditions can be precisely known and controlled. Experimental models allow us to observe and record the temporal evolution of deformation, whereas in nature only the final deformation state is observable.

Experimental models also allow us to examine the entire (visible) population of faults resulting from specific boundary conditions. Previous experimental modeling studies of oblique extension have focused on the geometry and spatial distribution of the resulting fault patterns in clay, sand, and sand over putty (Withjack and Jamison, 1986; McClay and White, 1995; Tron and Brun, 199, respectively). Fault geometries produced in these experiments were quite similar despite differences in the modeling media and experimental setup. This study quantifies changes in fault-population systematics as the rift angle decreases from $\alpha = 90°$ (pure extension) to $\alpha = 0°$ (pure strike slip). We obtained a large (>200) number of faults in each model, enabling us to accurately characterize the fault populations by integrating data on strain accommodation, fault geometries, scaling relationships, and the size and spatial distribution of faults.

1.3. Experimental Procedure

The modeling apparatus (Fig. 1.1) has a stationary base plate and four vertical walls, three fixed and one moveable. The dimensions of the apparatus are approximately 61 cm x 60 cm prior to deformation. Following Withjack and Jamison (1986), a metal plate is attached to the moving wall. The geometry of the metal plate varies in the models to simulate a range of oblique extension. In this series of models, the angle, α, between the rift axis (oriented parallel to the edge of the metal base plate) and the direction of displacement is varied in 15° increments between 0° (left-lateral strike slip) and 90° (pure extension). A latex sheet 6 cm wide is centered over the edge of the metal plate and the base plate and is securely attached. A 2.5 cm thick layer of wet clay overlies the metal plate, latex sheet and base plate. The clay (40% water by weight) is composed of

powdered kaolin ≤0.1 mm in diameter. Its density is approximately 1.65 g/cm^3 , it has a low cohesion (~50 Pa), and it has a coefficient of internal friction of about 0.5.

The cohesion and coefficient of internal friction of the wet clay are appropriate to insure dynamic similarity between the models and natural analogs (e.g., Hubbert, 1937). The cohesion of rock is about 10^4 to 10^5 greater than that of the modeling materials. The dimensions of the model are scaled down by a factor of 10^{-4} to 10^{-5} from those in the real world, such that 1 cm in the models is equivalent to 100 to 1000 m in nature. The wet clay represents strong rock that deforms by both distributed cataclasis and localized cataclastic faulting (i.e., upper crustal conditions; Withjack and Callaway, 2000).

For each model run, the moving wall is displaced a total of 6 cm at a constant rate of 3 cm/hr. As the wall moves, the attached metal plate also moves and the latex stretches uniformly, imposing distributed deformation to the overlying layer of wet clay, and producing a rift zone slightly wider than the latex sheet. We photographed the model surface, using at least two different lighting directions, every 0.25 cm of displacement. In this paper, we present results of the analysis at a single displacement increment (3.5 cm) to determine how fault attributes vary with rift angle. The temporal evolution of the α = 30° and α = 60° models are discussed in Chapter 2.

1.4. Data collection

We selected a rectangular study area of 650 cm^2 centered on the rift zone for each model. The size and position of the study area were chosen to eliminate edge effects caused by the outer walls of the apparatus and the short ends of the latex sheet. Defining the edge effect was based solely on visual inspection. The edge effect was considered

absent or minimal when the fault pattern became consistent. Use of photographic images of the model surfaces with two different lighting directions permitted accurate tracing of both the hanging-wall and footwall cutoffs of brightly lit fault scarps (see Fig. 1.2). We drew fault trace maps for each model at the 3.5 cm displacement increment (Fig. 1.3). At this displacement, fault populations on all models are sufficiently large to perform statistical analyses. Data collected from the fault trace maps for each α angle consist of the fault trend (measured from tip to tip), tip-to-tip length, and fault trace perimeter.

In analyzing the images of the model surfaces, as is also true in interpretting field and seismic data, determining the true length of faults can be problematic. In our experiments the uncertainty is primarily a result of photographic resolution which leads to three problems: 1) Faults smaller than 0.2 to 0.3 cm in length do not show up clearly on the images so that data for cumulative frequency of fault lengths are truncated at the small end. 2) On the black and white images, fault scarps facing the lighting direction appear white, whereas the area around the majority of fault tips appears gray. In many cases, we interpret the aureole of light gray at the fault tip as either a damage zone or a fold propagating in advance of the fault (Fig. 4d). The transition from white fault tip to gray aureole is commonly subtle on the images, indicating that a portion of the dataset for fault lengths is censored. However, in the majority of cases, using images from both lighting directions enabled us to confidently identify fault tips. 3) Image quality varies somewhat from one model run to the next and even within the study area of a given model. Where hanging-wall blocks have experienced considerable rotation or where grabens have formed on the model, some areas are in shadow from both lighting directions and small faults cannot be seen.

Uncertainty is greatest when determining the lengths of faults on the $\alpha \leq 15°$ models. The predominantly strike-slip faults in these models have significantly less vertical displacement than the normal faults, making them more difficult to distinguish on the images. Therefore, it is quite possible that faults on these models were undersampled at all scales. As is also the case with field data, there is no way to be certain that we are sampling the maximum dimension of any given fault, and it is likely that some faults that are smaller than the thickness of the model have not yet broken through to the surface.

Observation of the models as they evolved confirmed that most faults grow primarily by linkage. As a result, the majority of faults in this study are segmented (e.g., Trudgill and Cartwright, 1994). During the generation of fault trace maps, segment boundaries were identified using the following criteria: 1) abrupt changes in fault strike (Fig. 1.4d), 2) abrupt changes in fault displacement profiles resulting in displacement deficit in the middle of a fault (Fig. 1.4c), 3) abandoned splays (Fig. 1.4b), and 4) stranded footwall or hanging-wall rider blocks (Fig. 1.4a). Any of these criteria alone, except for the first criteria, can indicate a segment boundary. Inspection of images from consecutive displacement increments shows that, when faults grow by tip propagation, the fault tip may bend into the damage zone and abrupt changes in strike commonly result. Therefore, the first criterion must be used in conjunction with other criteria. Field and laboratory studies (e.g. Schlische and Anders, 1996; Withjack, unpublished data) indicate that the displacement deficit incurred during fault linkage is commonly preserved during subsequent fault growth. Consequently, we were able to identify fault segment boundaries with a high degree of confidence.

Sense of slip along faults in the models was determined qualitatively by visual

inspection during growth of the models and by offset of passive markers (e.g., linear scrape marks and air bubbles) on the model surface. A system of strain markers (e.g., a grid) was not placed on the model surfaces because previous work had indicated that they commonly act as anisotropies that influence the direction of fault propagation. During growth of the models, it was occassionally possible to see slickenlines on fault surfaces. Unfortunately, these do not show up on the photographic images.

1.5. Data

1.5.1. Description of fault trace maps

The pattern of faulting changes considerably as the rift zone becomes increasingly oblique, with the most noticeable change occuring between $\alpha = 45°$ and 30° (Fig. 1.3). However, there are many similarities in all of the fault-trace maps. Most faults exhibit the characteristics associated with segmented fault systems (e.g., Trudgill and Cartwright, 1994; Cartwright et al., 1995), including flat displacement profiles (3 in Fig. 1.4d), many abandoned splays (Fig. 1.4b), stranded rider blocks (Fig. 1.4a), and tortuous fault traces. Relay ramps are evident where fault tips approach each other, and horst and graben structures are also common. In most models, faults form clearly recognizable dip domains in which faults with a uniform dip direction are clustered together. At the boundaries of dip domains, the fault patterns become complex, resembling the accommodation zones described in the Gulf of Suez (e.g., Moustafa, 1996) and Mid-Atlantic Ridge (Mutter and Karson, 1992).

On all maps for $\alpha \geq 45°$, faults along the borders of the rift form a distinct zone separated in space from faults within the rift. These border-zone faults have a trend that

is slightly oblique to rift-parallel, whereas faults within the rift trend slightly oblique to the displacement-normal direction. This pattern of faulting is similar to that described at oblique mid-ocean ridge segments such as the Mohns Ridge (Dauteuil and Brun, 1996) and the Reykjanes Ridge (McAllister et al., 1995).

1.5.2. Fault geometry

The most obvious difference between oblique and orthogonal rift zones is the range of fault azimuths. We measured azimuth tip-to-tip for all continuous fault traces and obtained results that were consistent with the findings of Withjack and Jamison (1986). Our models confirm that, as α decreases from 90°, the range of fault azimuths increases steadily, with the greatest change occurring once again between $\alpha = 45°$ and 30°. Also, the predominant fault trend shifts gradually from displacement-normal to oblique with respect to both the displacement direction and the rift trend (see Fig. 1.5). When $\alpha = 45°$, the predominant fault trend lies exactly halfway between the rift trend and the displacement-normal trend. A major change occurs at $\alpha = 30°$, where two distinct peaks appear in the histogram of azimuths, indicating that there are two discrete subpopulations of faults, one approximately displacement-normal and the other striking rift-subparallel (i.e., $\leq 20°$ oblique to the rift trend). This also represents a change in the type of faulting, from exclusively dip-slip to a combination of dip-slip, oblique-slip and strike-slip faulting. As α decreases from 30° towards 0°, the distance between the peaks increases, and the relative proportion of strike-slip faulting increases.

For $\alpha \geq 45°$, the longest faults have an azimuth that coincides with the peak of the

histogram (Fig. 1.6) whereas the shortest faults span the entire range of azimuths within the model. For $\alpha = 30°$ and 15°, the longest faults have a displacement-normal trend whereas most rift-subparallel faults are short. For $\alpha = 0°$, the longest faults are approximately rift-parallel whereas the short faults range in azimuth from 000° (i.e., displacement-normal) to 345°.

1.5.3. Spatial pattern of faults

Between $\alpha = 45°$ and $\alpha = 90°$, faults with a rift-subparallel trend are found primarily at the rift margins. As α approaches 90°, these faults begin to link to form long, en-echelon border-fault arrays. At $\alpha = 90°$, a single border fault has formed (Fig. 1.3). Between $\alpha = 45°$ and $\alpha = 75°$, faults in the center of the rift zone have a trend that is oblique to displacement-normal. The obliquity of that trend decreases as α approaches 90°. For $\alpha \leq 30°$, rift-subparallel faults that strike $\leq 20°$ oblique to the rift trend are predominant both in the center of the rift and at the rift margins, and displacement-normal faults cross the rift zone. As α increases, the width of the deformed zone at the surface of the model increases (Fig. 1.7).

We measured fault spacing along scanlines oriented parallel to the displacement direction for models of $\alpha = 45°$ through 90° (Fig. 1.8). Brittle deformation in these models is dominated by faulting along displacement-normal faults. Results show that mean fault spacing increases with α. The most likely reason for this is that the longer faults in the less oblique models have larger stress-reduction shadows (e.g., Ackermann and Schlische, 1997) in which new faults cannot form. The standard deviation of spacing

also increases, indicating that spacing becomes somewhat less regular as α increases. For all models, the standard deviation is close to or greater than the mean. The high standard deviation is primarily a result of a zone of no faulting which lies between faults on the rift borders and those in the center of the rift.

The software package Benoit (TruSoft International, 1997) was used to investigate how the fractal dimension of the map pattern varies with α, and to determine whether the spatial patterns of faults in this study are multifractal. The fractal dimension is a quantification of the degree to which the map pattern is space-filling. A single straight line on a map would yield a fractal dimension of 1, whereas a completely filled map would yield a fractal dimension of 2 (Fig. 1.9). Benoit uses a box counting algorithm, which counts the number of boxes necessary to cover a dataset of points (pixels). Box size is varied geometrically within a range determined by the smallest and the largest distance between points on the fault maps. The program calculates two fractal dimensions, the capacity dimension D_c, which simply counts the number of occupied boxes, and the information dimension, D_i, which is D_c weighted by the normalized mass of points (pixels) present in each box. The log of the box size is then plotted against the log of the number of occupied boxes (or the weighted number of occupied boxes). If the data fall on a straight line, the map pattern is considered to be fractal and the slope of that line is the fractal dimension. Values for D_c and D_i in this study (Fig. 1.10) fall between 1.35 and 1.64, consistent with values found for fault patterns in the field (Aviles et al., 1987; Okubo and Aki, 1987; Hirata, 1989). Both D_c and D_i increase between $\alpha = 0°$ and $\alpha = 45°$, reflecting the fact that the fault maps become increasingly space-filling. Above $\alpha = 45°$ values of D_c and D_i level off at 1.62 and 1.64, respectively, consistent with a

theoretical D value of 1.65 derived by Takayasu (1986) for a percolating crack network and an upper limit of D = 1.6 for branching fault networks in central Japan (Hirata, 1989).

Multifractality is an indicator of spatial clustering. Cowie et al. (1995) describe a multifractal set as one which has a power-law cumulative frequency of lengths superimposed on a fractal map pattern. The closer in value that D_c and D_i are, the less multifractal the data are considered. Our oblique models cannot be considered multifractal because D_c and D_i are nearly equal for all values of α (see Fig. 1.10). This is consistent with our results for cumulative frequency distribution of fault lengths (see section 1.5.6).

1.5.4. Fault-related strain

We measured fault-related strain for models of $\alpha \geq 45°$ along scan-lines oriented parallel to the displacement direction at the model surface. The width of each fault polygon is approximately equivalent to the heave on the fault. Thus, the sum of the widths of the fault polygons can be used to calculate fault-related strain. However, for models with strike-slip faults, ($\alpha \leq 30°$), the assumption that fault heave is related to strain is not valid.

The amount of extensional strain imposed at the base of our models varies according to:

$$\varepsilon_{xx} = (d/u) \sin \alpha \qquad (1)$$

(Withjack and Jamison, 1986), where ε_{xx} represents extensional strain in the displacement direction, u is the original width of the rift and d is the distance that the rift

edge has been displaced. Despite the increase in imposed strain with increasing α, the amount of strain attributable at the surface to brittle faulting remains almost constant and only represents between 30% and 50% of the imposed strain (Fig. 1.11). These results are consistent with conclusions of Kautz and Sclater (1988), who observed that as much as 50% or more of strain is accommodated by faults that fall below the resolution of detection methods. They suggest that the amount of "hidden extension" is a function of both the minimum amount of observable slip and the grain size of the deformed material. In our clay models, this represents over two orders of magnitude of fault size on which slip is occurring below the detection limit. Our results suggest that the amount of hidden extension is greater in rifts with higher α values, but it is not clear whether this is due to differences in the amount of extensional strain, differences in fault geometry or both. Future work is required to seek the answer.

1.5.5. Fault length

Any continuous fault trace on the model surface is considered to be a single fault whose length can be measured as either trace length or tip-to-tip length (Fig.1.12a). The measurement of trace length is more sensitive to resolution than the tip-to-tip length. Therefore, all length measurements in this study are made tip-to-tip. The ratio between fault trace length and tip-to-tip length is defined here as fault tortuosity (Fig. 1.12b). Tortuosity values fall between 1 for a perfectly straight line, and infinity for an infinitely tortuous fault trace. It is a function of both the degree of fault linkage and the variation of azimuth within the total population. With the exception of $\alpha = 0°$, tortuosity tends to increase with fault length within a given model. Average tortuosity is maximum when α

= 30° (Fig. 1.13). In this model, extensional strain is accommodated by two sub-populations of oblique-slip normal faults which interact, particularly in the center of the rift, by linking to form long, zigzag faults. Despite the fact that the range of azimuths is even greater in the $\alpha = 15°$ and 0° models, the two sub-populations do not link to the same degree. Instead, strain is partitioned between two sets of predominantly strike-slip faults.

Several parameters related to fault length clearly vary with α, but each in a different manner (Fig.1.14). The length of the fault at the 95th percentile of all lengths (L_{95}) increases steadily from $\alpha = 0°$ to 90°. Summed fault length rises steeply to a maximum value at $\alpha = 45°$ and then levels off. Data for the number of faults in each model rises and falls apparently unsystematically. When these parameters are normalized by the study area affected by faulting, changes in summed fault length and number of faults follow the same pattern, indicating that they are closely related. The $\alpha =$ 0° model has an anomalously high number of faults, due to the highly discontinuous nature of the strike-slip faults that occur in a very narrow deformed zone. Between $\alpha =$ 15° and 90°, both the number of faults and summed fault length increase to a maximum at $\alpha = 45°$, then decrease for $\alpha = 60°$ and 75° before increasing again at $\alpha = 90°$. This pattern is most likely related to varying degrees of nucleation vs. linkage as α increases. Faults nucleate more slowly in the highly oblique models, while at the same time, linkage is limited by fault geometry. Conversely, faults nucleate readily in the less oblique models whereas most fault growth is accomplished by linkage. In these models, rift geometry is the primary factor limiting fault growth. When $\alpha = 90°$ (i.e., pure orthogonal rifting), fault growth is relatively unrestricted.

1.5.6. Cumulative Frequency of lengths

Fault-scaling relationships have been used to estimate the relative numbers of faults that fall below the resolution of detection methods, to determine the aggregate properties of fault populations, to understand the process of fault population evolution in space and time, and to infer aspects of the underlying physical process of fault growth (Cowie et al., 1996). Previous workers have proposed that an exponential distribution of sizes with the form

$$N(L) = N_T e^{-\lambda L} \quad (2)$$

characterizes fault populations both at the earliest stages of their evolution, when nucleation of new faults exceeds growth of existing faults (Cowie et al., 1995) and again after the largest faults have exceeded the thickness of the brittle layer (Ackermann et al., 1997). N is the total number of faults with dimensions greater than or equal to some length (L), N_T is the total number of measurements, and λ is a scaling parameter that is the inverse of the characteristic length (L_c) . Between those extremes, a power-law distribution of sizes is expected such that

$$N(L) = a\, L^{-C} \quad (3)$$

where a is related to the total number of measurements and C is the power-law exponent. A power-law distribution of sizes is indicative of self-similar fault growth and scaling (Main, 1996). Sornette et al. (1990), Cowie et al. (1995) and Cladouhos and Marrett (1996) suggested that the power-law exponent of a given fault population should decrease as the population evolves and large faults accommodate increasingly more strain.

We eliminated measurements at the small end of the dataset (left-hand truncation

of Pickering et al., 1995), recognizing that too many small faults fall below the resolution of the imaging technique, and plotted the data in log-linear space. For models of $\alpha \geq 30°$ we are confident that long faults were thoroughly sampled and that, therefore, these data should not be considered censored. There is greater uncertainty of this for models of $\alpha \leq 15°$ because of the lack of vertical offset along strike-slip faults. Cumulative frequency plots for all values of α show that all of our data are better fit by an exponential distribution than by a power-law, with the possible exception of $\alpha=60°$ and 90° (Fig.1.15). However, even for those models, a power-law distribution does not describe the whole data set. In fact, there appears to be a bimodal distribution that may indicate two sub-populations that scale differently. Wojtal (1996) and Ackermann and Schlische (1997) also observed two fault subpopulations in outcrop studies that appear to be scaling differently. On the same plots, we show the cumulative frequency for fault segments (as determined by the criteria described in section 1.3). These data are fit very well by an exponential distribution for all values of α.

Not surprisingly, L_c for whole faults increases with increasing α in the same manner as does L_{95} (see Fig.1.16). Alternatively, L_c for fault segments remains approximately the same for all values of α. Some studies suggest that segment length is controlled by mechanical layer thickness (Jackson and White, 1989; Scholz and Contreras, 1998). Our results suggest that one or more of the boundary conditions or material properties may control the length of fault segments, but it is fault geometry that controls how those segments link to form longer faults.

1.6. Discussion

1.6.1. Fault linkage

Withjack and Jamison (1986) determined, both empirically and analytically, how stress and strain states vary with rift obliquity. In the analytical models, for all values of α, two of the principal stresses are horizontal and one is vertical. One of the horizontal principal stresses is tensional, and as α increases from 0° to 90°, the angle between the rift trend and the principal stress also increases. For $\alpha \geq 45°$, both of the horizontal principal stresses are tensional (the vertical principal stress is always 0); for $\alpha \leq 30°$, one of the horizontal principal stresses is tensional whereas the other principal horizontal stress is compressional. Such stress states explain why so many of the major changes occur between $\alpha = 30°$ and $\alpha = 45°$. They also provide an explanation for fault geometry and for the variation in the number and length of faults with α. The clay, like rock, is weaker under tension than compression. When $\alpha \leq 30°$, the models are in compression and it is more difficult for faults to nucleate and lengthen. Hence, fault number and summed fault length are expected to be low. When $\alpha \geq 45°$, both horizontal stresses are tensional and faults can nucleate and grow more easily. The transition from a domain of dip-slip, oblique-slip and strike-slip faulting to one of purely dip-slip faulting occurs at $\alpha = 45°$ (see Fig. 1.14). Whereas the number of faults is maximum at $\alpha = 45°$ and decreases when $\alpha = 60°$, fault length (L_{95}) almost doubles. We believe this occurs as extensional strain reaches a critical threshold after which growth by linkage dominates over growth by tip propagation, and fault nucleation either decreases considerably or

ends all together. Rifts that are less oblique (i.e., have a higher value of α) have more extensional strain at a given displacement increment than highly oblique rifts (i.e., having a lower value of α; see Fig. 1.17). By the displacement increment analyzed in this study, models for $\alpha \geq 60°$ have experienced enough extension to have passed this threshold.

The kinematics of faulting in each model also has an influence on how much linkage can occur. Faults are overwhelmingly dip-slip in these models, with little evidence of oblique-slip (i.e., slickenlines on fault surfaces show only dip-slip motion). For $\alpha = 0°$ and 15° faults are predominantly conjugate strike-slip faults, with rift-subparallel faults having left-lateral offset and displacement-normal faults having right-lateral offset. These faults cannot share a slip vector and, therefore, truncate against one another and do not interact. In the few instances where the two sub-populations of faults interact and link in the $\alpha = 15°$ model, a significant dip-slip component develops once linkage has occurred and the now normal fault exhibits a near right-angle bend. It is unclear why this should happen in a predominantly strike-slip model. One possibility is that, during linkage, faults rotate to an orientation more favorable for dip-slip motion. For $\alpha = 30°$, rift-subparallel faults exhibit left-oblique slip, whereas displacement-normal faults exhibit right-oblique slip. The geometry and kinematics of these faults allows some dip-slip motion to continue after they link. Faults in this model are highly complex and anastomosing, with many right-angle bends.

1.6.2. Spatial pattern of faults

Despite the lack of pre-existing anisotropy in our models, faults spontaneously develop in domains of uniform dip. Small faults are more abundant in the zone where

faults of opposing dips have met. This can be seen best in our $\alpha = 45°$ model (Fig. 1.18). The most likely explanation for this apparent clustering is as follows: As the fault population evolves, small faults grow by tip propagation until they interact with other faults and link to form longer faults which continue growing. However, when the tips of faults having opposing dips meet, many of the faults lock, unable to gain either length or displacement. New faults must then nucleate in order to take up the continued strain imposed on the model.

The azimuths of small faults at a given α span the full range of the population, yet the longest faults all have the dominant trend. Possible explanations include the following: 1) small faults form with a wide distribution of azimuths but only those which are favorably oriented grow to significant length; 2) at low α values, faults rotate about a vertical axis as they lengthen; 3) small faults with a rift-parallel orientation form late during population evolution and do not have a chance to grow longer; or 4) small faults of every orientation link up and attain an "average" azimuth as they lengthen. We suspect that all of these play a part. Evidence for the fourth alternative comes from the fact that the range of azimuth for segments is greater than that for whole faults. The fact that fault tortuosity has a general tendency to increase with fault length further supports this hypothesis.

In general, small faults tend to cluster both around fault tips and at the rift margins on all models where $\alpha \geq 30°$. Small faults that form at the rift margins are associated with a flexure that forms in the clay above the boundary between the latex sheet and the metal plate. This flexure becomes more pronounced as extension progresses and the center of the rift zone thins and subsides. The pattern of faulting at the rift

margins in our oblique models is in fact similar to the secondary fault pattern produced by oblique-slip over a master fault. Using experimental models, Schlische et al. (1999) observed this pattern develop as faults cut an extensional forced fold (monoclinal flexure) which forms over a basement fault experiencing oblique-slip. These authors noted that relay ramps between the faults are not breached until displacement on the master fault is large. Thus, the faults do not lengthen by linkage and remain short as a result. We believe the same thing is happening in our models, but on a smaller scale at the rift margin.

1.6.3. Cumulative frequency distribution

Before fitting our cumulative frequency distributions, we eliminated truncated data at the small size end of the distribution. We are confident that our data for models of $\alpha \geq 30°$ do not suffer from censoring at the large end of fault sizes. Because we are sampling experimental models in which we can see the entire population (above the imaging resolution), we know that there are no faults larger than the ones we can see and that we are sampling all faults present. The only faults that were not included in the analyses are those that formed in the area affected by boundary conditions at the edges of the apparatus. We believe that the manner in which the number of long faults in our models decreases is a result of boundary conditions imposed by the geometry of the rift. It is notable that, except for in the $\alpha = 90°$ model, the longest faults stop lengthening well before reaching the edge of the model and that the length of the longest faults increases with α. In fact, it is the geometry of the rift zone which limits fault length. If faults trend obliquely to the rift axis they either stop lengthening or begin to curve when they reach the rift valley walls. This may explain why a power-law size distribution is not

appropriate for our data and perhaps not appropriate for fault populations in all oblique rift zones. It may also be the reason why it is the high end of our data that diverges most from the best-fit exponential curve (see Fig. 1.15).

In oblique rift zones, the geometry of the rift and the resulting trends of the faults have the greatest influence on how faults link. Therefore, it is not surprising that the cumulative frequency distribution of lengths varies with rift obliquity. The fact that characteristic length (L_c) for fault segments does not change significantly with α implies that it is indeed how these segments combine which determines the cumulative frequency distribution for whole faults. An exponential distribution fits our data for fault segments significantly better than data for whole faults. Davy (1993) describes a similar relationship in the San Andreas fault system where he found that small fault "strands" related to the larger fault system follow an exponential distribution whereas the fault system as a whole does not.

1.6.4 . Geological examples: continental rifts

Withjack and Jamison (1986) applied results of their experimental and analytical models to successfully explain fault patterns in the Gulf of Aden and the Gulf of California. Additional, more recent detailed field data from the Gulf of California (e.g., Umhoefer and Stone, 1996) provided additional support of those models. Fault patterns similar to those in our models occur in continental rift zones that have localized along pre-existing tectonic trends oblique to the direction of absolute plate motion. The locations discussed below are shown in Figure 1.19. The Connecticut Valley rift basin localized along a northerly trending tectonic grain during Triassic rifting, when

displacement between North America and Africa was approximately NW-SE (e.g., Withjack et al., 1998; Fig. 1.20a). Two trends of normal faults were identified in the basin fill adjacent to the northerly trending border fault, one approximately 20° oblique to the trend of the border fault and the other approximately displacement normal (Clifton, 1987). De Boer and Clifton (1988) proposed that more northerly trending faults formed above weaknesses in the basement early in the basin history, and rotated slightly in response to far-field stresses as they propagated upward into the basin fill. More northeasterly trending, displacement-normal faults developed later, in the basin fill, and became the predominant fault trend in the center of the basin.

Færseth et al. (1997) offered a similar interpretation of the fault pattern in the northern North Sea (Fig.1.20b), where basins localized along northerly trending Permian structures during NW-SE extension in the Jurassic. Early basin-parallel faults formed coevally with small northeast- trending faults, but a northeast-trending fault set predominates later in basin evolution. Færseth et al. (1997) reject the notion that a change in stress direction is required to produce the two sets of faults present in the northern North Sea. Our models support their conclusion. When rotated into the same orientation as these basins, the fault geometry in our α=75° model looks similar to both of the above examples. Once again, it is a difference in boundary conditions between the rift margin and the center of the rift zone that results in two fault sets forming during oblique extension.

1.6.5 . Geological examples: oblique mid-ocean ridge segments

Scaled physical models have been used to interpret the geometry and evolution of

fracture populations that form on mid-ocean ridges during oblique extension. Dauteuil and Brun (1993, 1996) compared their sand over putty models to the Mohns Ridge, which is 45° oblique to the spreading direction. Applegate and Shor (1994) compared their fracture data for the Reykjanes Ridge to the clay models of oblique rifting of Withjack and Jamison (1986) and the sand-over-putty models of Tron and Brun (1991). All authors noted that the scaled models accurately predict the fault geometry that is present on these oblique ridge segments. Tuckwell et al. (1996) note that a transtensional model, supported by the clay models of Withjack and Jamison (1986), best matches the features of oblique ridge segments on slow-spreading ridges.

The fault patterns on our models compare well with fault patterns described on oblique mid-ocean ridge segments. Our models represent distributed deformation of a relatively thin brittle layer above a narrow discontinuity that deforms continuously. This is analogous to the deformation observed at mid-ocean ridges which comprises normal faults, opening mode fissures, and dike-induced grabens narrowly distributed over a volcanic zone. Although all brittle deformation in our models is accommodated by normal faults, the geometry and distribution of fractures is comparable to that at ridges. Although the models cannot reproduce the deformation resulting from magma injection, they can predict the fracture pattern that results exclusively from far-field tectonic stresses (see Chapter 3). The models are particularly useful analogues for slow-spreading ridges, where faulting contributes significantly to extension (Cowie et al., 1993a).

Dauteuil and Brun (1996) described a pattern of complex, wavy and anastomosing faults in the axial valley of the Mohns Ridge in the North Atlantic ($\alpha = 45°$ to 50°). They noted that faults along the rift valley walls are short and slightly oblique to the rift trend,

whereas faults in the rift valley are longer, less complex and trend normal to the spreading direction. They also described "spindle" and "y-type" connections resulting from linkage of faults with different azimuths. They interpret the en-echelon pattern of faults at the valley walls as evidence of strike-slip displacement but present no evidence of actual offset. Our $\alpha = 45°$ model has similar fault geometries, with short faults trending slightly oblique to rift-parallel on the margins of the deformed zone and longer displacement-normal faults in the center of the rift zone. The greatest complexity occurs where these two fault sets interact near the southern (lower) rift margin (see Fig. 1.21a and b). Faults at the rift margin exhibit en-echelon geometry, but all displacement is pure dip-slip. In fact, there is no evidence of strike-slip displacement anywhere in this model.

McAllister et al. (1995) described a wide distribution of fault azimuths along the Reykjanes Ridge ($\alpha = 60°$ to $65°$) with a spatial distribution of faults similar to our $\alpha = 60°$ model (Fig. 1.21c and d). Faults within the rift valley trend nearly normal to the spreading direction whereas faults along the rift walls are long and trend parallel to the rift axis. Histograms of fault trends on the Reykjanes Ridge (McAllister et al., 1995; see their Fig.10) show that faults at the rift margin have a wider range of azimuth than faults in the center of the rift, and that many faults are oblique to the rift trend. The authors suggested that faults form in the center of the rift as a result of plate-spreading stresses, whereas, on the edge of the rift, they form under a distinct stress system oriented perpendicular to the rift axis. They proposed that this stress develops as a result of lithospheric cooling away from the ridge axis. In our models, the zone of faulting at the rift margin has a rift-parallel trend, and the longest faults in this zone do indeed have a rift-parallel trend. However, the majority of faults are short and trend as much as 10°

oblique to the rift axis. We believe that they are forming as a result of a secondary stress system localized along the flexure that develops where the latex sheet is joined to the metal plate (i.e., where boundary conditions have changed). We agree that lithospheric cooling and resulting gravitational effects are probably responsible for the fault pattern at the walls of the Reykjanes and Mohns Ridges. We suggest that stresses related to plate motion are modulated and reoriented by a secondary stress field related to changes in topography and crustal rheology at the rift valley walls. It is the interaction of these two stress systems that causes faults to strike oblique to the rift trend rather than parallel to it (see Chapter 3 for further discussion).

1.7. Summary and Conclusions

Clay experimental models have been used to simulate fault population systematics in oblique rift zones. The following parameters of fault populations vary systematically with rift obliquity:

1) The range of fault azimuths increases as rift obliquity increases (i.e., as α decreases). For values of $\alpha \geq 45°$, faults at the rift margin are slightly oblique to the rift trend, whereas faults in the center of the rift are slightly oblique to the displacement-normal direction. All faults experience dip slip. When $\alpha \leq 30°$, two fault populations of equal importance develop in the center of the rift: one approximately rift parallel and the other approximately displacement normal. Faults in these models experience dip-slip, oblique-slip and strike-slip motion.

2) The fractal dimension of the spatial pattern of faults increases as α increases and is comparable to values derived analytically (Takayasu, 1986) and measured in the

field (Hirata, 1989).

3) The length of the longest faults and the width of the deformed zone both increase as α increases.

4) The cumulative frequency distribution of fault lengths varies with α. The cumulative frequency does not follow a power-law for any of our models, with the possible exception of $\alpha = 90°$. An exponential distribution best describes our data for whole fault and fault segment lengths. L_c for whole faults increases as α increases, but L_c for fault segments remains relatively unchanged.

Several parameters vary due to fault linkage:

1) For all oblique rifts dominated by normal faulting, fault tortuosity increases with fault length. This is a result of linkage between short fault segments with a broad range of azimuths.

2) Fault tortuosity is maximum when $\alpha = 30°$ as two subpopulations of faults link.

3) The greatest increase in fault number, at $\alpha = 45°$, is followed by almost as great a decrease at $\alpha = 60°$ and is coincident with the greatest increase in the length of the longest faults. This change occurs after a critical strain threshold is reached. Subsequently, most fault growth is accomplished by linkage. Simultaneous increase in fault length and decrease in fault number characterize such an event.

Many of the characteristics of fault populations that we observe in our models have been described at oblique segments of the Mid-Atlantic Ridge, including the Mohns Ridge and the Reykjanes Ridge. A secondary stress system forms at the rift margins in response to a change in boundary conditions. Interaction of two stress systems causes faults in that zone to stike oblique to the rift trend, whereas faults that are approximately

displacement-normal form in the center of the rift zone. Our models reproduce the geometry of faults described in continental rift zones such as the Connecticut basin and the basins of the northern North sea, which localized along pre-existing tectonic trends oblique to the direction of displacement. Our models also provide good analogs for characterizing brittle deformation at mid-ocean ridges where homogeneous, relatively thin crust is being deformed by tensional forces in a confined rift zone where the spreading vector is known. The geometry and spatial distribution of faults in oblique rift zones are predictable and are a function of the angle between the rift trend and the direction of displacement. The characteristic length of fault segments that form in the rift does not vary with α, but the manner in which those segments link to form longer faults is a function of rift obliquity.

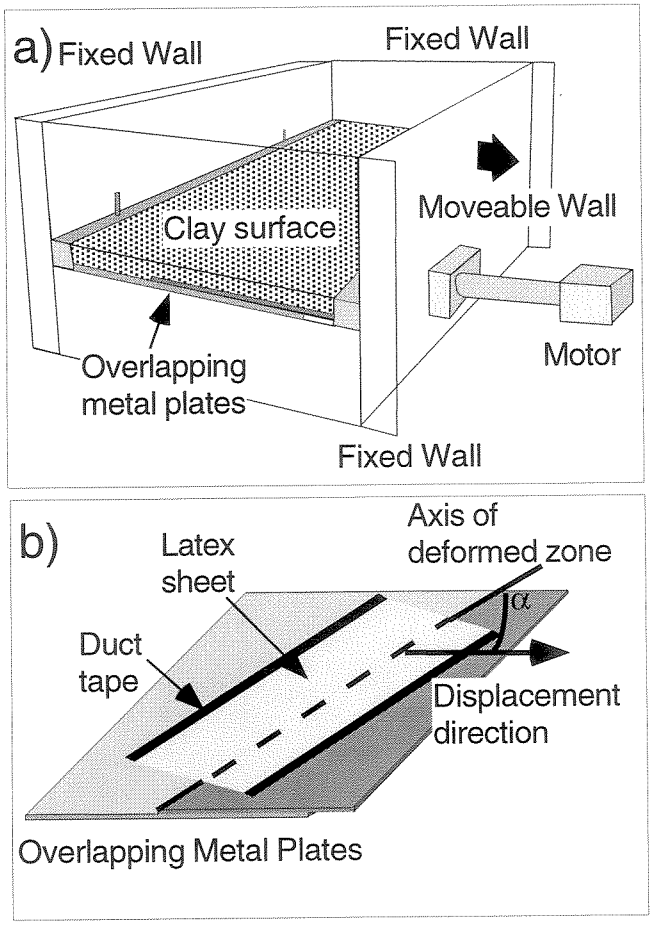


Fig. 1.1. (a) Experimental apparatus. (b) Detail of apparatus surface without clay layer, showing that α is defined as the acute angle between the rift axis and the displacement direction (Withjack and Jamison, 1986).

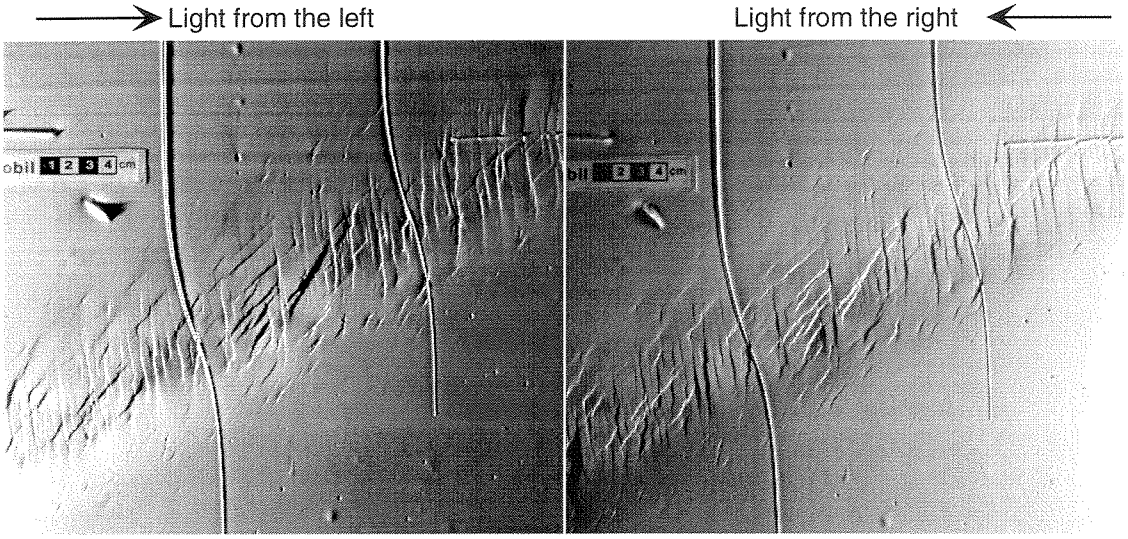


Fig. 2. Photographs of the surface of model α=30° shown for two different lighting directions. Brightly lit fault scarps face the lighting direction. The moving wall is to the right. Thick lines on model surface are trowel marks.

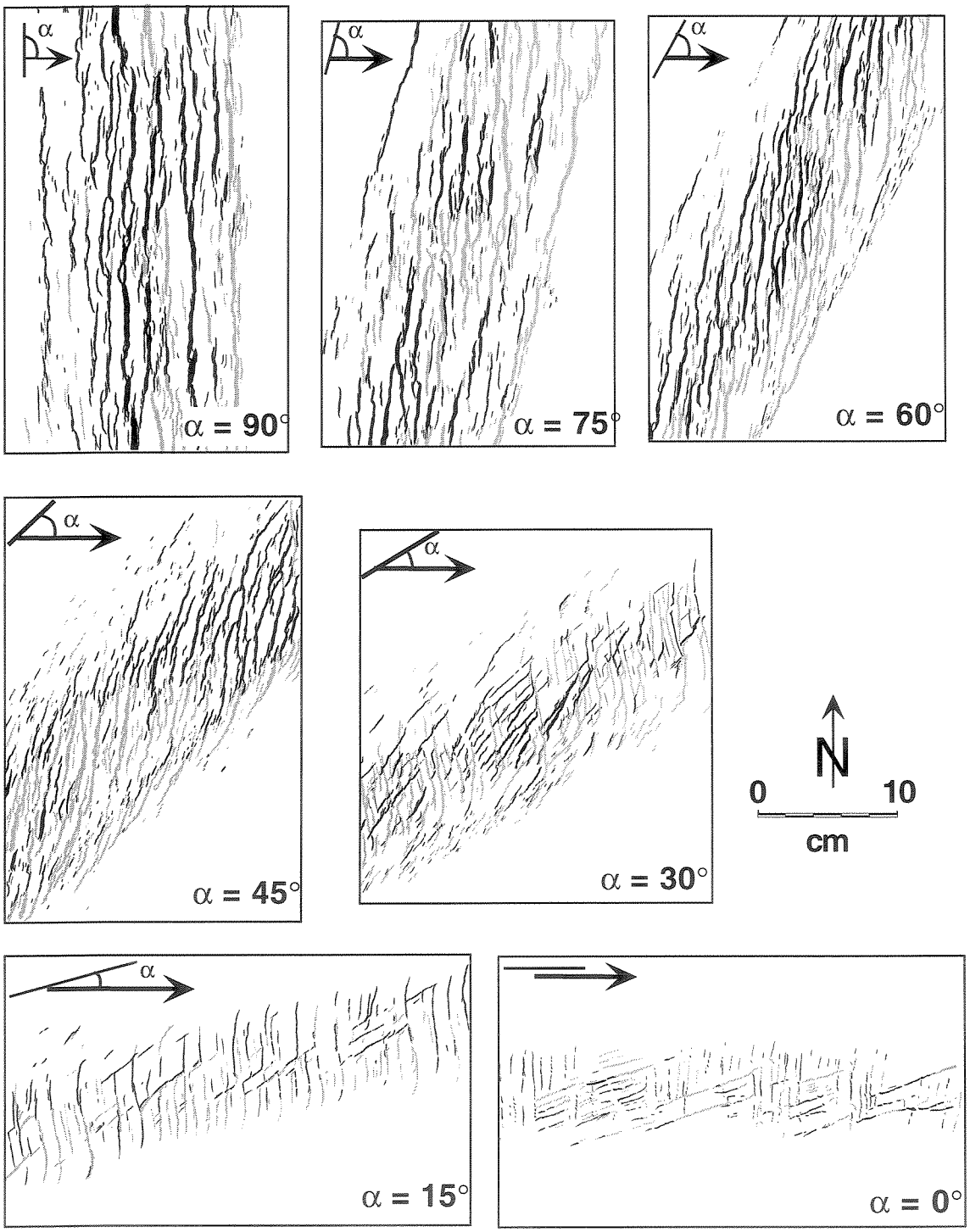


Fig. 1.3. Fault trace maps. Black fault surfaces face the moving wall and dip to the right. Gray faults face away from the moving wall and dip to the left.

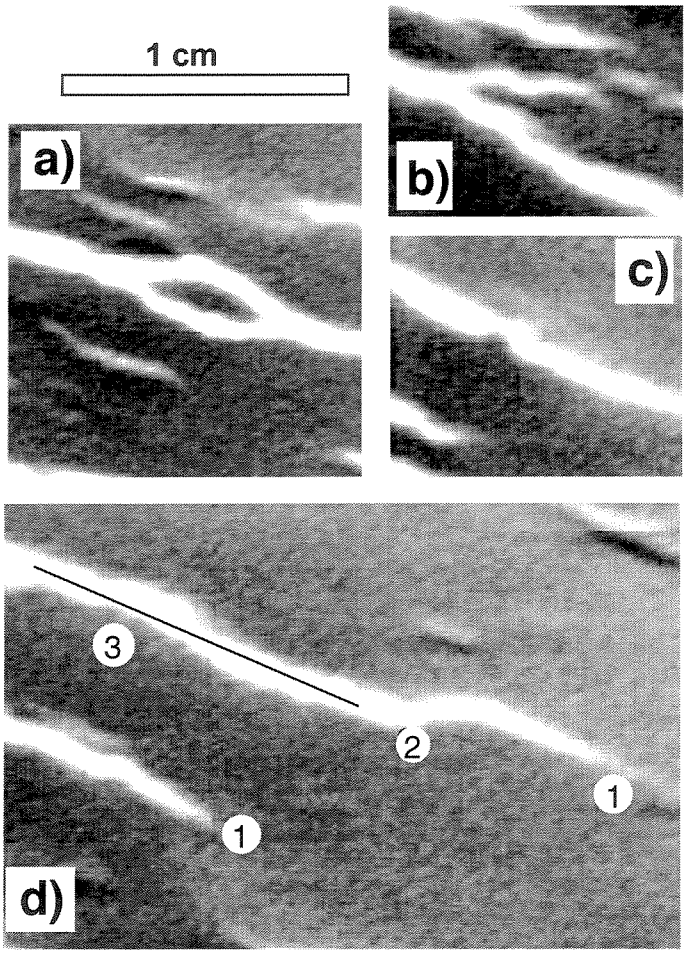


Fig. 1.4. Criteria for identifying segment boundaries: (a) abandoned rider block; (b) abandoned splay; (c) displacement deficit in the center of the fault trace; (d) trace of a long fault for which 1 denotes gray aureoles at two fault tips, 2 denotes a change in strike that may be due to tip propagation rather than linkage and 3 denotes a part of the fault trace with a flat displacement profile.

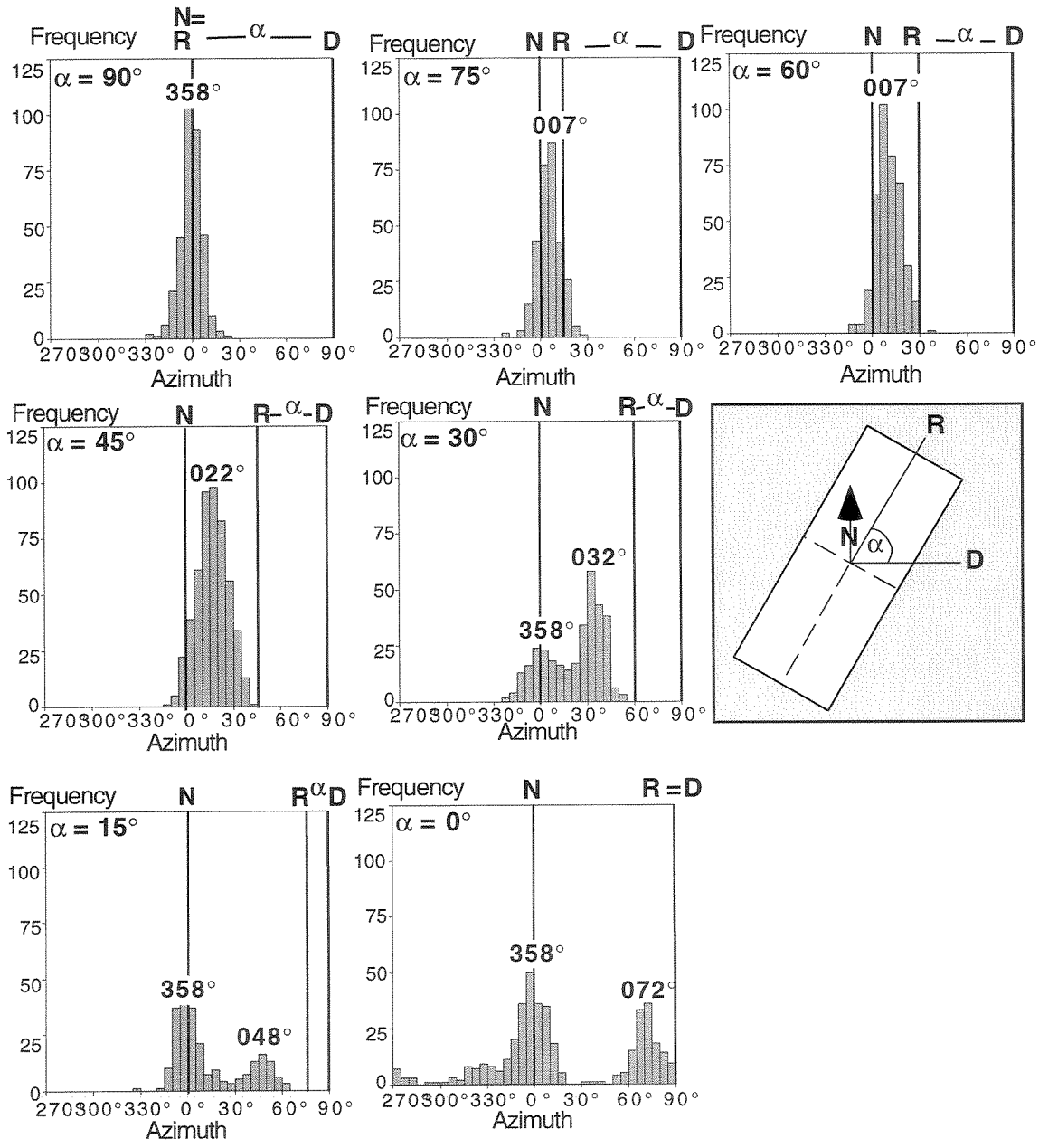


Fig. 1.5. Histograms of fault azimuth for all models. R is the trend of the rift axis for each α angle; D is the trend of the displacement direction, defined as 090°; N is the displacement-normal direction defined as 000°

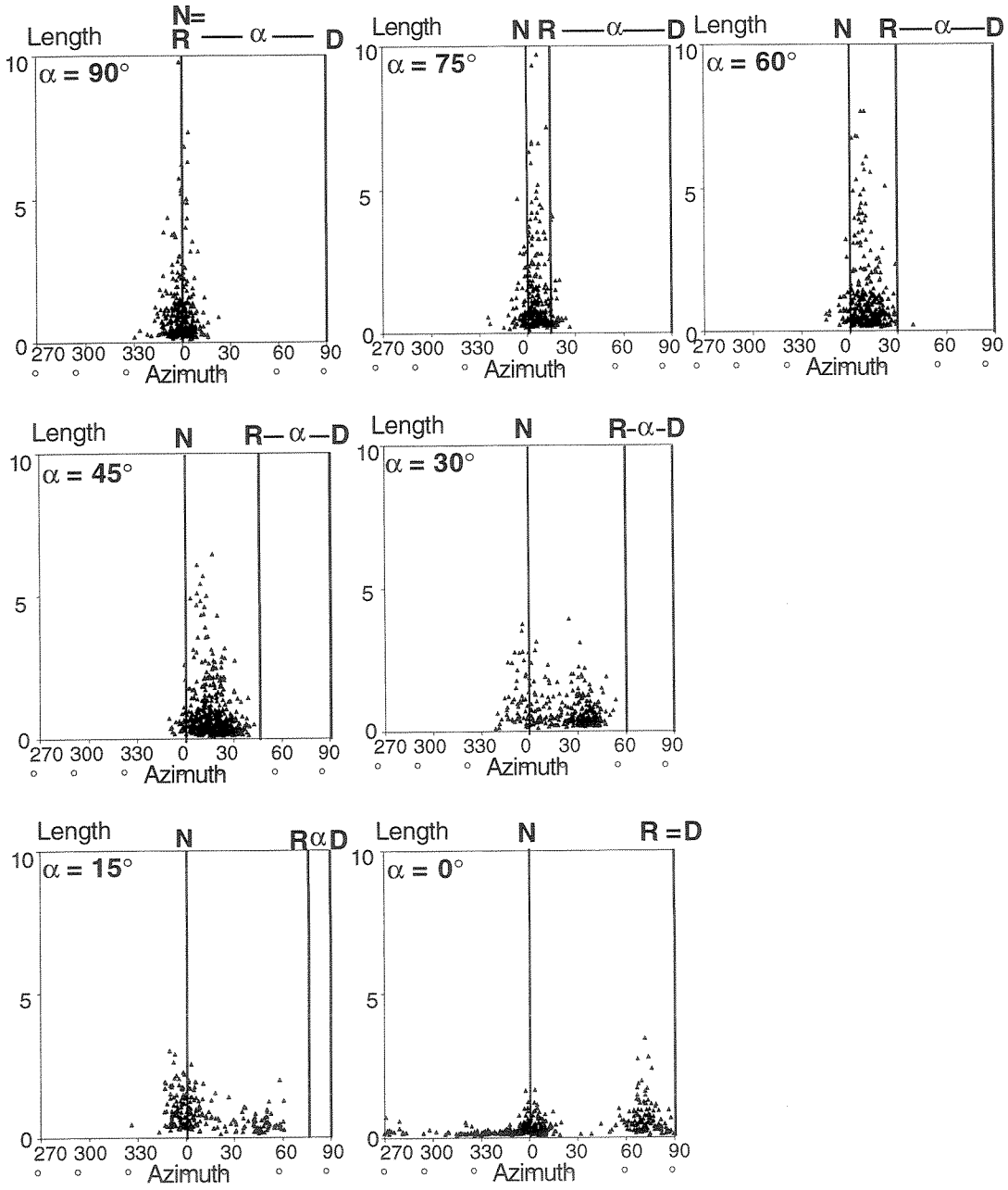


Fig. 1.6. Fault length vs. azimuth for all models. Letters the same as in Fig. 5.

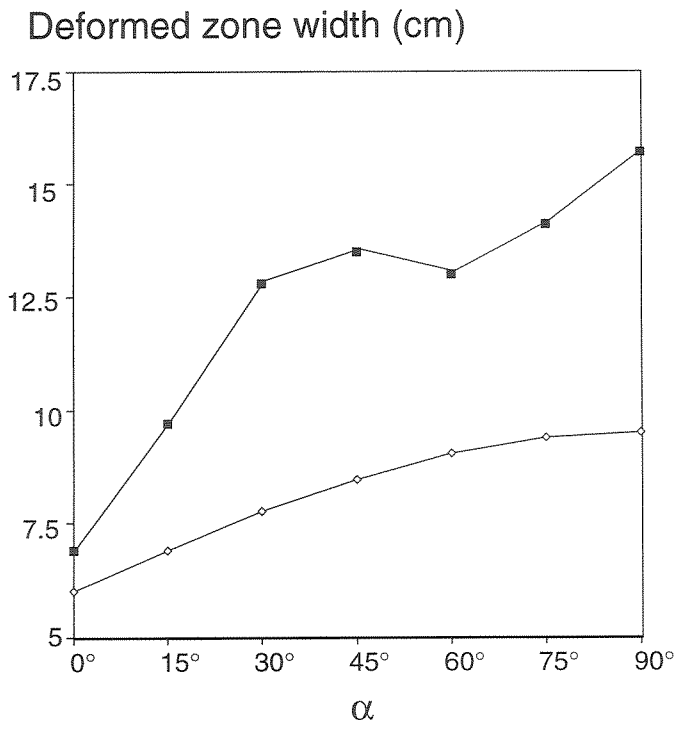


Fig. 1.7. Variation with α in width of the deformed zone at the clay surface (black squares) and at the base of the model (open diamonds) .

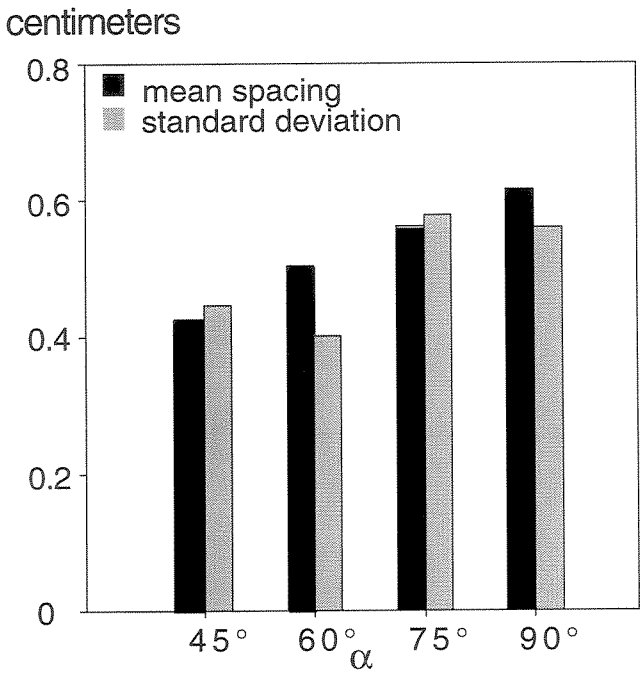


Fig. 1.8. Bar graph of mean fault spacing (black) and standard deviation of fault spacing (gray).

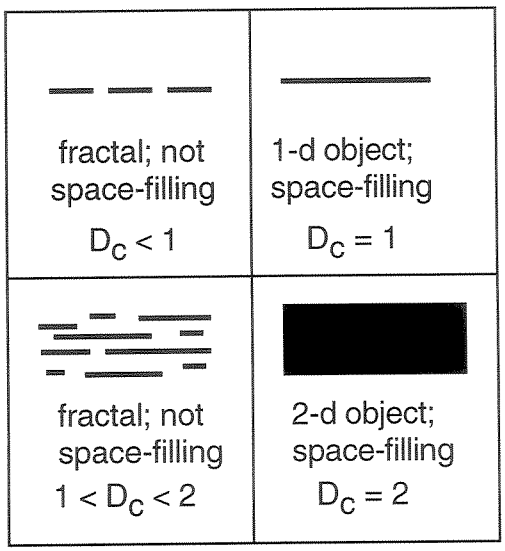


Fig. 1.9. Examples of map patterns with different fractal dimensions. Redrawn from Ackermann et al. (2000, in review)

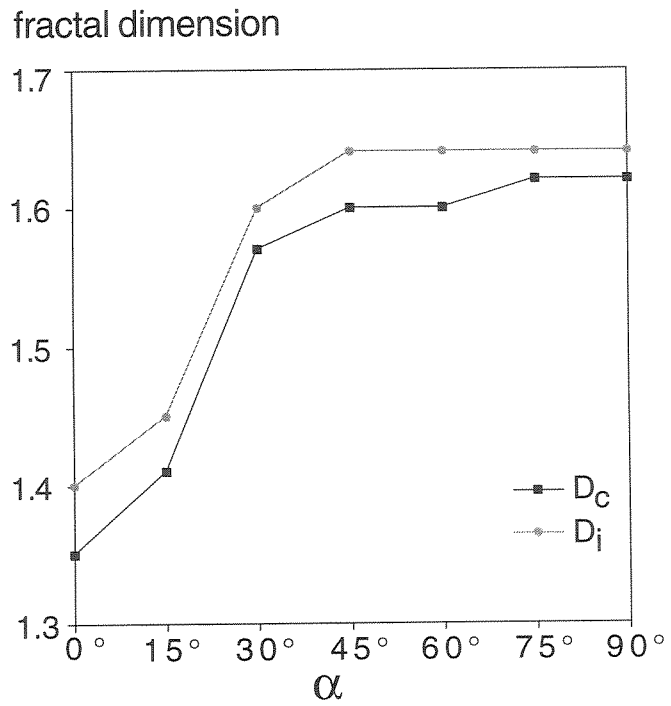


Fig. 1.10. Graph of the capacity dimension (D_c) and the information dimension (D_i) as a function of α, as calculated by Benoit software.

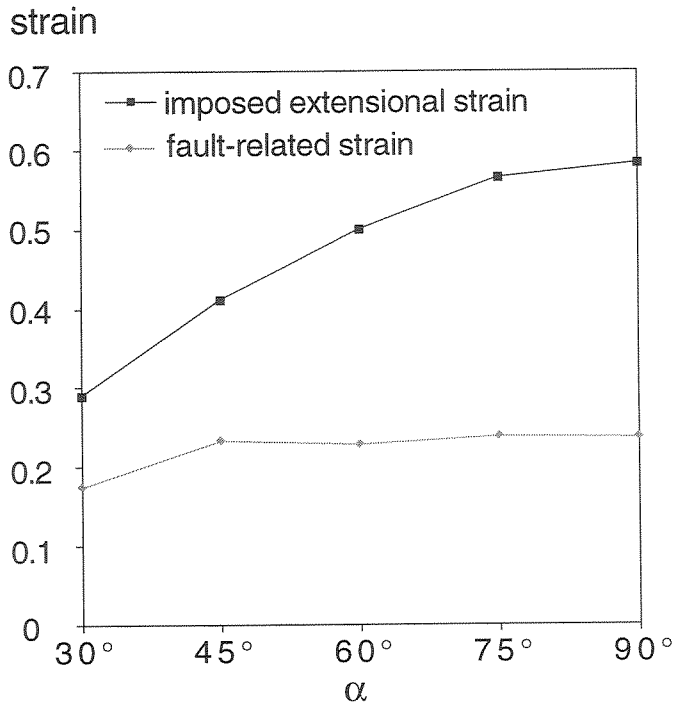


Fig. 1.11. Graph showing how imposed extensional strain in the displacement direction (square symbols) compares with fault related strain (diamond symbols) for $\alpha \geqq 30°$.

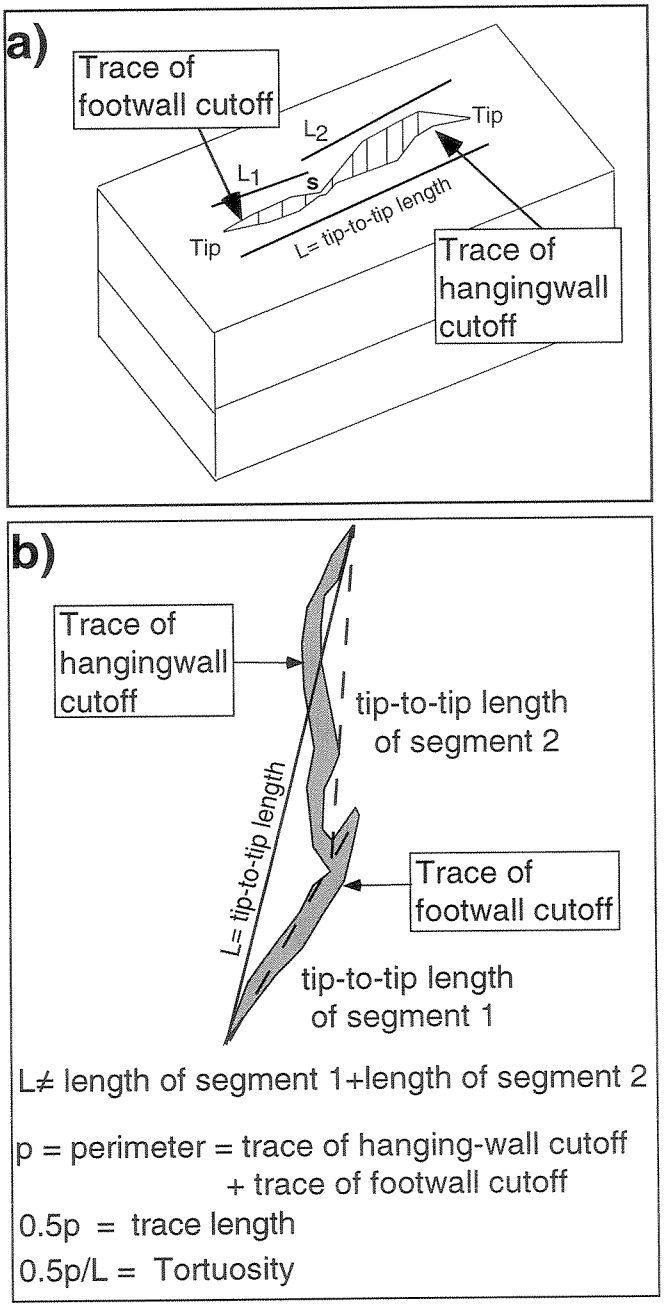


Fig. 1.12. (a) Diagram showing hanging-wall and footwall cutoffs along a segmented fault. L1 and L2 are tip-to-tip lengths of individual segments, whereas L is the tip-to-tip length of the entire fault. s is the segment boundary. Note that tip-to-tip lengths and azimuths of segments do not equal that for the entire structure. Note too that the trace lengths defined by the hanging-wall and footwall cutoffs are significantly longer than tip-to-tip lengths. Note displacement deficit at **s**. (b) Diagram defining fault tortuosity as the ratio of fault trace length to tip-to-tip length.

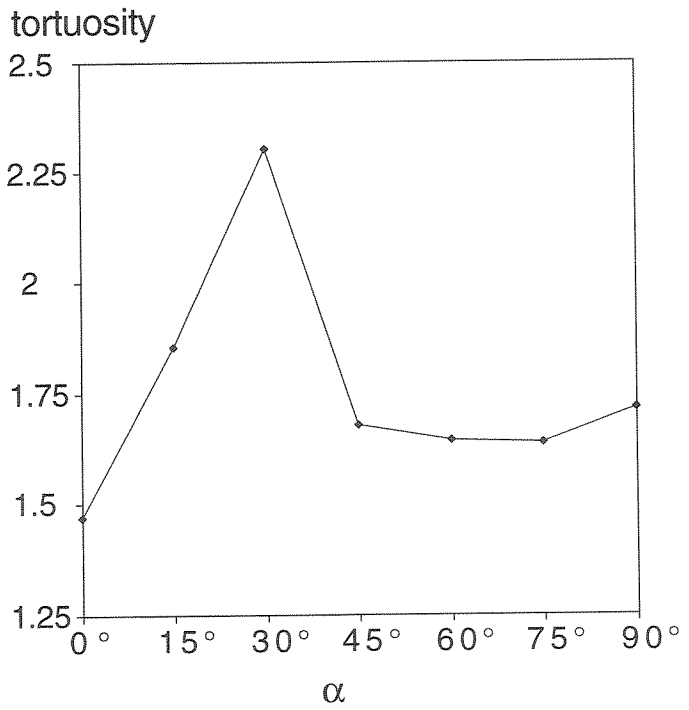


Fig. 1.13. Variation of average tortuosity with α. Values of tortuosity are normalized by fault length.

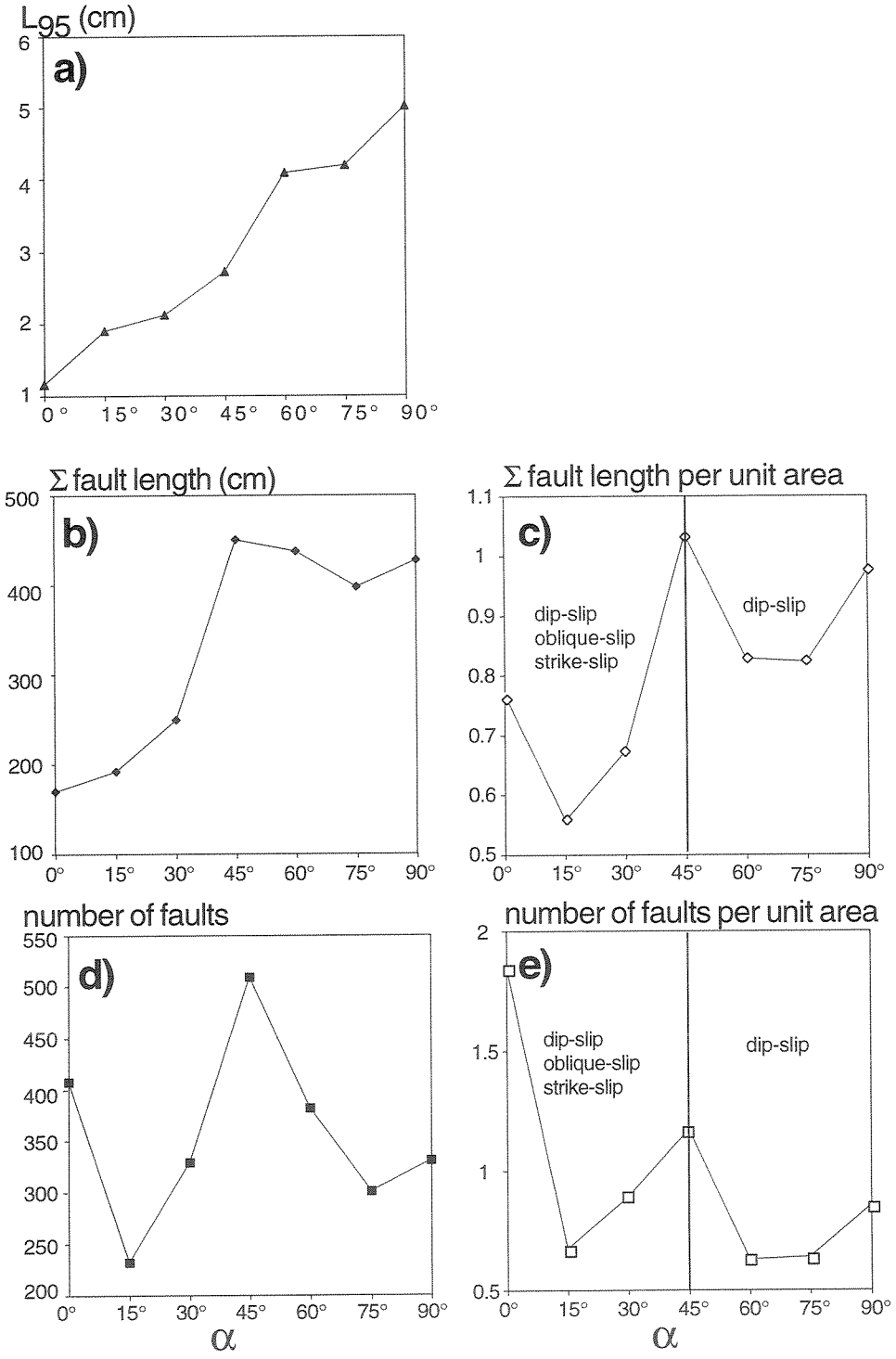


Fig. 1.14. Graphs showing how (a) the length of the fault at the 95th percentile of lengths, (b) summed fault length, and (d) number of faults vary with α. (c) Summed fault length per unit area. e) number of faults per unit area. See text for discussion.

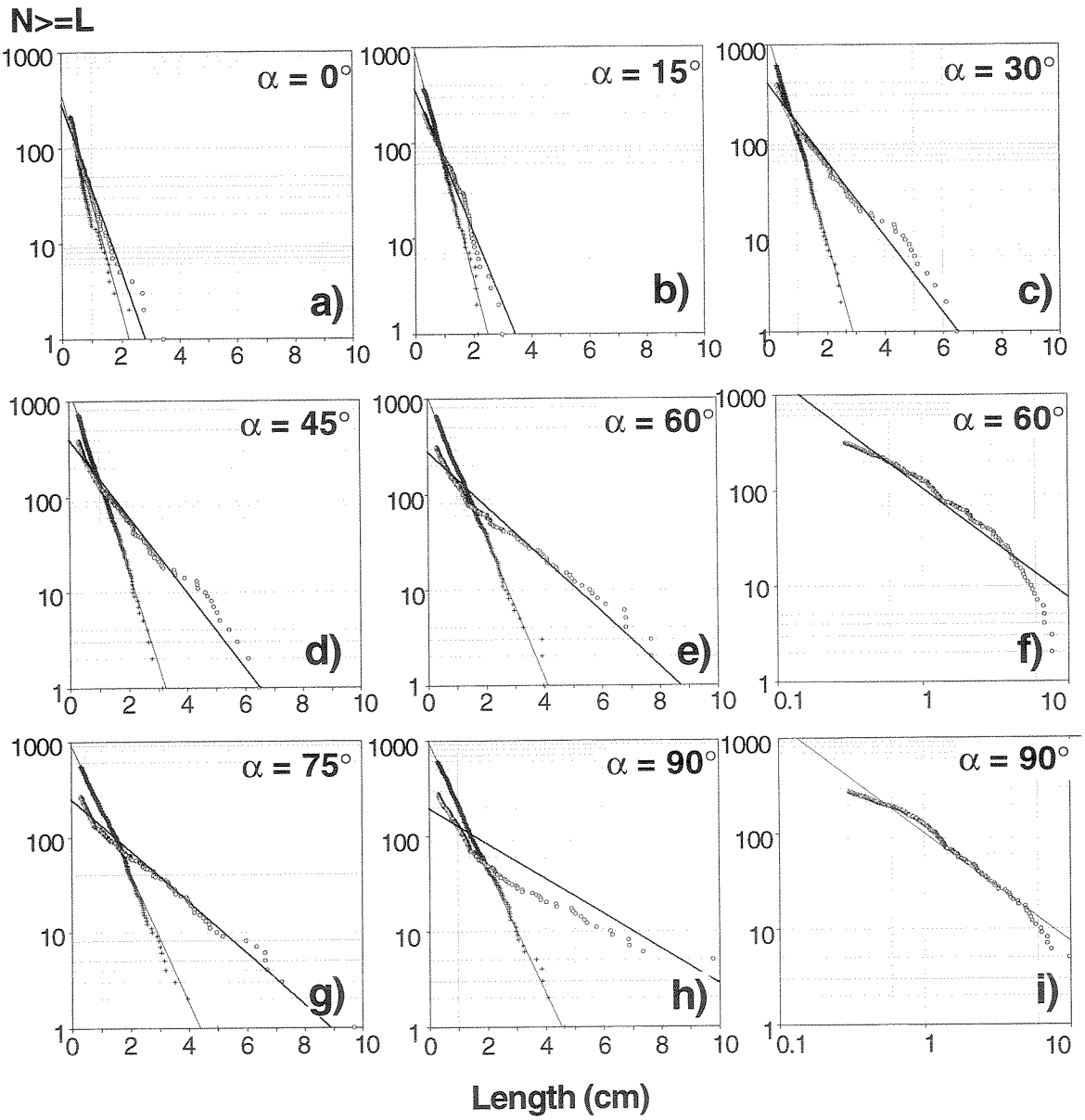


Fig. 1.15. Graphs showing cumulative frequency of lengths for whole faults (open circles) and for fault segments (crosses). a - e, g and h are log-linear plots showing exponential fits. f and i are log-log plots showing power-law fits.

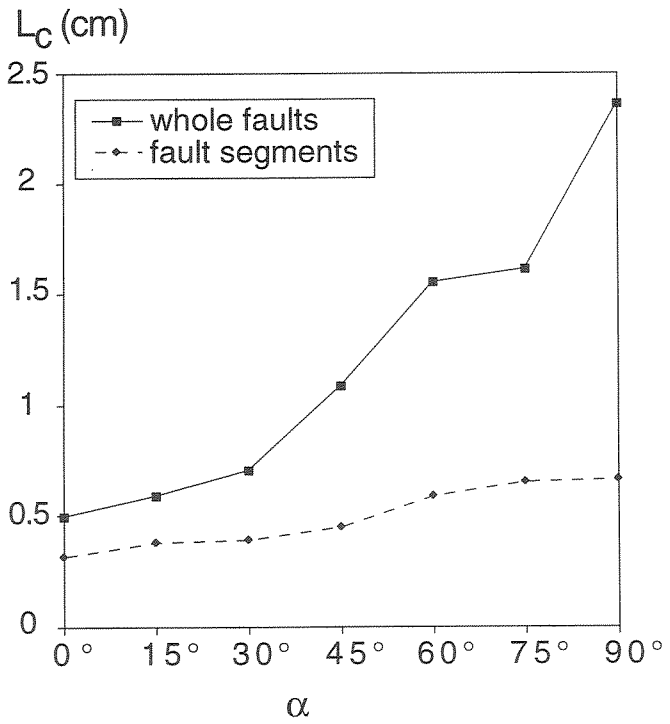


Fig. 1.16. Graph showing variation in characteristic length (L_c) with α for whole faults (large squares) and fault segments (small circles).

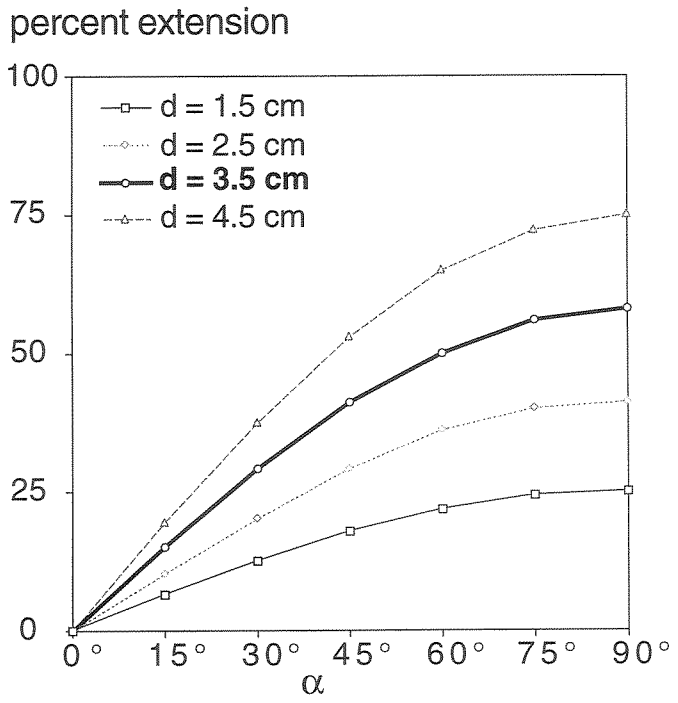


Fig. 1.17. Graph showing how imposed horizontal extensional strain in the displacement direction at the base of the model varies with α at different displacement increments during fault population evolution.

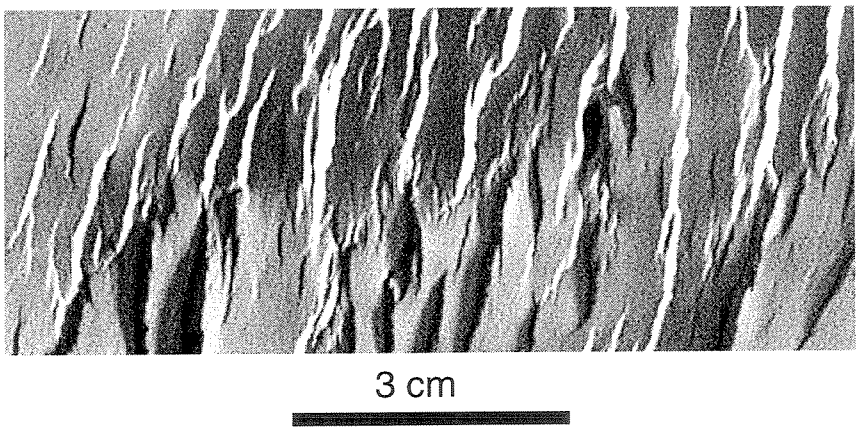


Fig. 1.18. Detail from a photograph of the α=45° model showing the zone of complex faulting that forms where dip domains of opposite polarity meet.

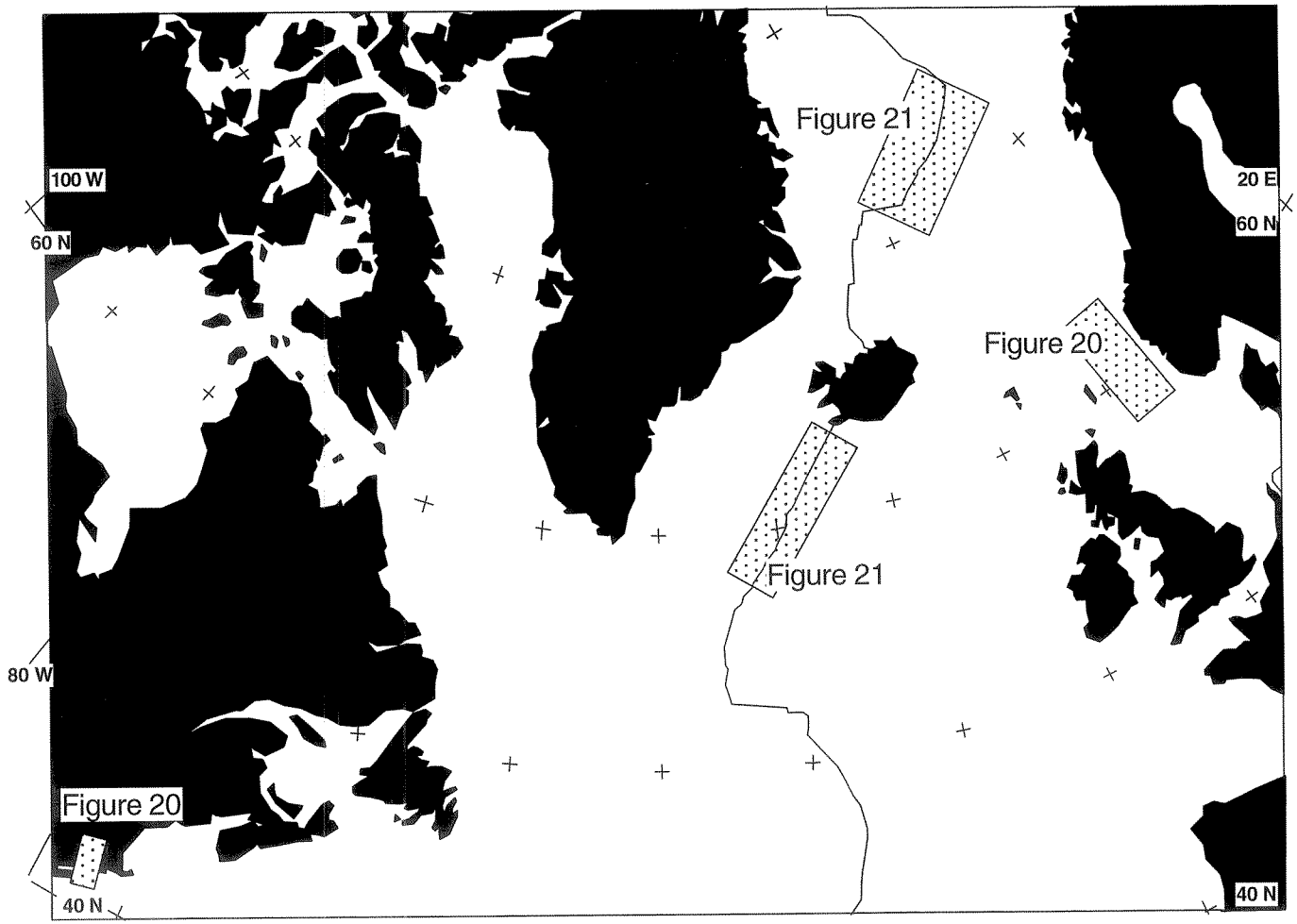


Fig. 1.19. Location map showing field examples of oblique rift zones (redrawn and simplified from Vogt, 1986)

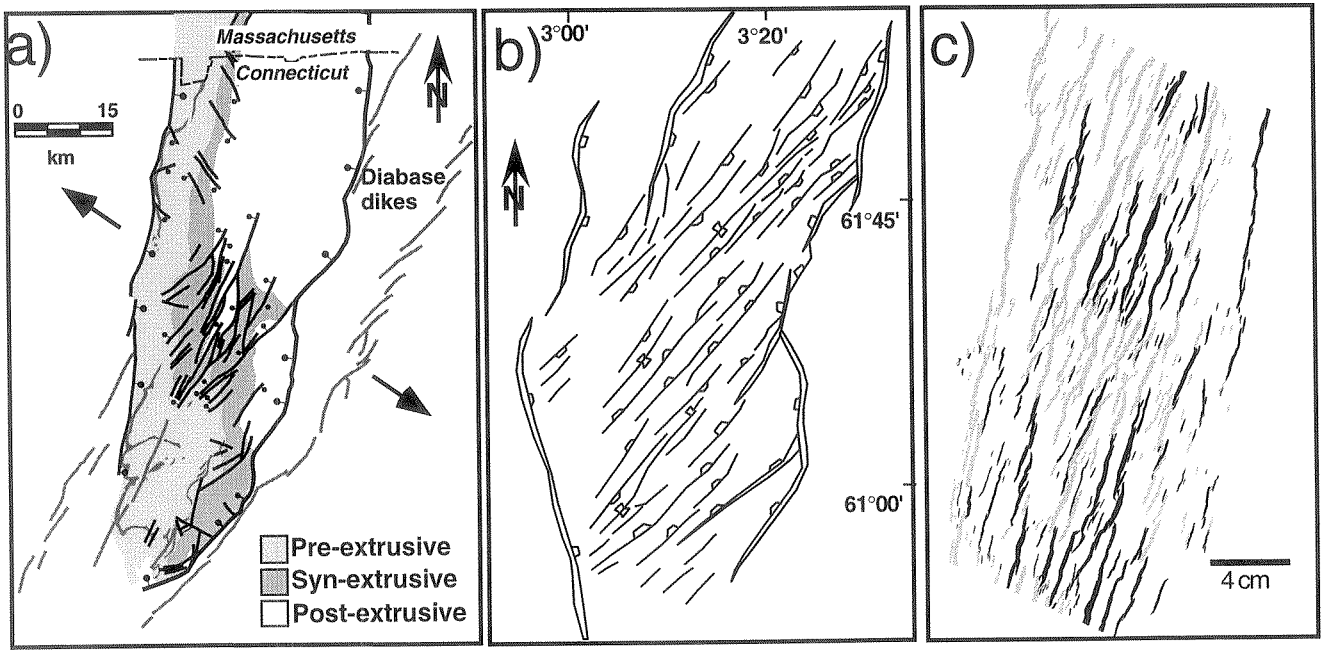


Fig. 1.20. Comparison of map patterns of faults in oblique continental rift basins with fault trace map of our clay model. (a) Faults in the Hartford sub-basin, Connecticut, simplified from Schlische (1993). (b) Faults in the Viking Graben, northern North Sea (redrawn from Færseth et al., 1997). (c) Fault trace map of our $\alpha = 75°$, flipped horizontally and rotated into the same position with respect to the displacement direction as the basins above.

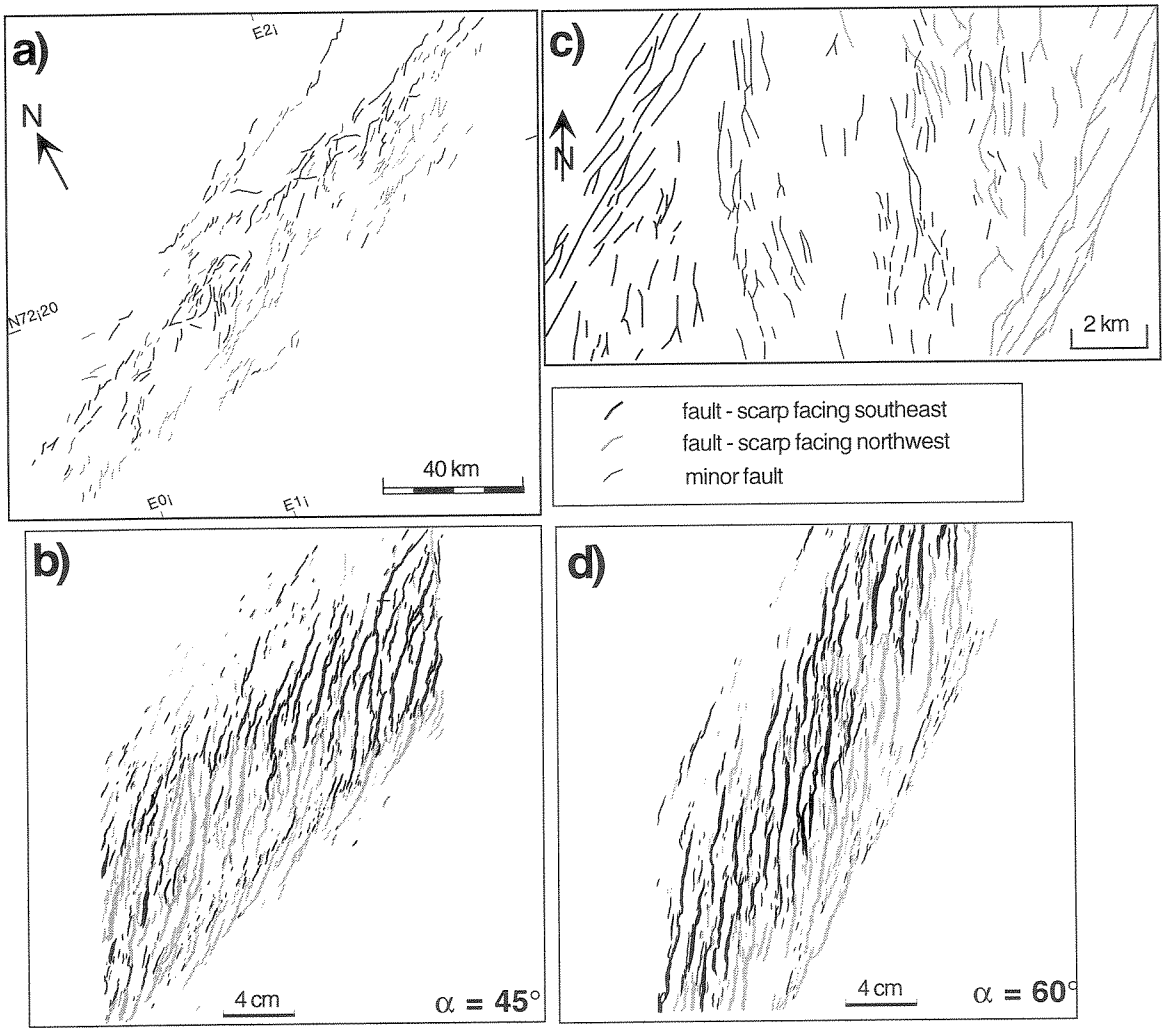


Fig. 1.21. Comparison of map patterns of faults on oblique mid-ocean ridge segments with fault trace maps of our clay models. (a) Faults on the Mohns Ridge (redrawn from Dauteuil and Brun, 1996). (b) Fault trace map for $\alpha = 45°$. (c) Faults on a small section of the Reykjanes Ridge (redrawn from McAllister et al., 1995). (d) Fault trace map for $\alpha = 60°$. All maps are oriented so that the spreading (displacement) direction is perpendicular to the side of the box.

Chapter 2- Nucleation, growth and linkage of faults in oblique rift zones: results from experimental clay models

2.1. Abstract

I have used scaled clay models to study the temporal evolution of fault populations in experiments of moderately oblique (α= 60°) and highly oblique (α= 30°) distributed extension, where α is defined as the angle between the rift axis and the direction of displacement of the moving wall. The degree of rift obliquity places constraints on the style of fault growth from the earliest stages of fault population evolution. Brittle deformation begins with the nucleation of small isolated faults around random heterogeneities in the clay. They in turn enhance the nucleation of diffuse clusters of new faults whose geometry determines the style of subsequent fault growth. In the α = 30° model, clusters of displacement-normal faults form parallel arrays, leading to fault growth dominated by tip propagation and along-strike linkage until maximum length (controlled by the width of the deformed zone) is achieved. Subsequent growth of rift-subparallel faults leads to a phase of growth characterized by linkage and formation of complex, branching faults with high tortuosity. In the α = 60° model, clusters form in a stepping geometry leading to growth dominated by linkage. Faults nucleate and grow more rapidly, and their growth is less restricted in the moderately oblique model.

2.2. Introduction

The scale of geologic time is such that we can rarely, if ever, observe a geologic process in its entirety. The events that collectively contribute to the evolution of a geologic system occur far too slowly, or result from too many successive rapid events

with long recurrence intervals. Thus, we need to infer what those events have been from the geologic record and modern analogues. A clearer understanding of these events with respect to the evolution of fault systems has immediate relevance for earthquake hazard assessment and prediction, understanding fault sealing, fluid flow and depositional patters. There is a growing realization among researchers that examining the entire fault population in a given area (e.g. a plate boundary segment) can greatly enhance our understanding of the behavior of a specific fault (Cowie, 1998a; Main, 1996; Cowie et al., 1995). In particular, considerable research in seismology during the past eight years has focused on fault interaction as a triggering mechanism for earthquakes (e.g. Jaumé and Sykes, 1992; Bowman et al., 1998; Freed and Lin, 1998; Hardebeck et al., 1998; Gupta and Scholz, 2000).

Scaled experimental models are ideal for studying the temporal evolution of geologic systems, because we know the boundary conditions and can observe a process from start to finish. With scaled clay models of brittle deformation, we can observe the entire visible population of faults that form in response to a particular stress system and chart the nucleation, growth and interaction of faults as the population evolves. Results from analyses of the models can then be used to guide and support investigations in real-world settings.

Ackermann et al. (1997; submitted) used scaled clay models of simple orthogonal extension to study the effect of certain boundary conditions on the evolution of fault populations. These studies quantified the effect of mechanical-layer thickness and width of the deforming zone on the evolution of fault population systematics in extensional tectonic settings and support the conclusions of field studies (e.g., Scholz and Contreras,

1998). This chapter examines the effect of rift obliquity on the evolution of fault populations in extensional settings. Rift obliquity is related to the angle, α, between the rift trend and the direction of displacement of the rift walls (Withjack and Jamison, 1986), so that the value of α is inversely related to the degree of obliquity. Work in oblique rift zones around the world (e.g., Umhoefer and Stone, 1996; Chorowitz and Sorlein, 1992; Dauteuil and Brun, 1996; Applegate and Shor, 1994) as well as scaled modeling experiments (e.g., Withjack and Jamison, 1986; Tron and Brun, 1991; McClay and White, 1995; Clifton et al., 2000) have shown how rift obliquity affects fault geometry and spatial distribution. However, little is known about what role this parameter plays in the temporal evolution of fault populations. In particular, this study examines how fault nucleation, growth and interaction vary with α by comparing modeling results from a moderately oblique rift ($\alpha = 60°$) and a highly oblique rift ($\alpha = 30°$).

2.3. Methods

The experimental modeling technique used in this study is fully described in Chapter 1 (see Section 1.2 and Fig.1.1). Models were subjected to different combinations of extension and shear by changing the orientation of a metal base plate attached to a moving wall which was extended at a constant rate of 3 cm/hour. A 6 cm wide latex sheet was taped so that it straddled the metal base plate and a stationary plate beneath it so that, when the moving wall was extended, it imposed distributed deformation to the overlying 2.5 cm thick layer of wet clay. In order to record the temporal evolution of the fault population, a camera was mounted over the model surface; photographs were taken after every 0.25 cm of displacement of the moving wall, from time 0 until the end of the model

run (after 5 cm of displacement; i.e. 1.5 hours). The camera was positioned over the center of the model so that the entire deformed zone could be photographed. Two lighting directions 180° apart were used to fully define fault scarps with a general dip direction toward and away from the moving wall.

Images were scanned and analyzed using the same techniques described in Chapter 1 (see Section 1.3). Care was taken to use the same study area for each displacement increment. Fault trace maps were drawn by tracing polygons around the horizontal projections of the hanging-wall and footwall cutoffs on the top surface of the models. Fault trace maps for one increment were overlain on images of the next increment to correctly position the study area boundaries and to ensure consistency in identifying faults. This technique eliminated some of the uncertainties inherent in analyzing a model at a single displacement increment (see Section 1.3). Charting the growth of each fault made it easier to identify fault tips and to distinguish a fault from a possible flaw on the image. The images analyzed here include those taken between 1 cm of displacement (when faults first appear on the models) and the 3.5 cm displacement increment used to analyze the entire α suite in Chapter 1.

Data consist of the number of faults visible on the model surface, fault trend (measured tip-to-tip), fault-trace perimeter, and tip-to-tip fault length (fault trace length is approximated by one half of the fault trace perimeter). Terms used to describe the models are defined as follows. The area of the model directly above the latex sheet is considered the rift zone. The deforming zone is wider than the latex sheet and includes the entire area where faulting has occurred. The zone of faulting outboard of the latex sheet is considered the rift margin.

2.4. Data

2.4.1. $\alpha = 60°$

For the $\alpha = 60°$ experiment (Fig. 2.1), faults begin to nucleate around random flaws (most likely small air bubbles) in the clay. The first faults to appear at the model surface are located in the center of the zone of deformation and all but one dip away from the moving wall (left-dipping). Many fractures begin as opening-mode cracks but evolve into normal faults by 1.25 cm of displacement. These first faults are relatively straight, isolated structures. As extension continues, new faults tend to nucleate close to these first faults, forming three diffuse clusters in the center of the rift. At 2.0 cm of displacement, faults appear at the rift margin closest to the moving wall. Most of these are left-dipping and are separated by a gap of 1 to 2 cm from faults in the rift zone. Coevally, right-dipping faults appear in significant numbers inside the rift zone. By 2.25 cm of displacement, distinct domains in which dip direction is uniform develop and maintain themselves throughout the rest of the model run. In general, faults dip inward toward the center of the rift zone, which is the area of maximum thinning and subsidence of the clay. After 2.5 cm of displacement, the number of new faults nucleating within the rift zone decreases dramatically; deformation is dominated by faults that lengthen along strike, gain displacement, and link with other faults (Fig. 2.2). Fault nucleation also decreases at this point along the rift margin closest to the moving wall. However, faults first appear on the margin farthest from the moving wall at 2.75 cm of displacement. Throughout the rest of the model run, new faults continue to nucleate along both margins as older faults lengthen. By 3.5 cm of displacement, the rift margin closest to the moving wall is

characterized by many long, relatively straight faults that have a rift-parallel trend. Faults on the opposite margin are shorter and strike oblique to the trend of the rift zone, but they form an en-echelon array that is rift-parallel.

Histograms of azimuths for the $\alpha = 60°$ model (Fig. 2.3) show that most of the first faults to form have a displacement-normal trend. However, even at this early stage in the model's evolution, there are a significant number of faults oblique to that trend. By 1.75 cm of displacement, the peak of the histogram is oblique to the displacement-normal trend and remains there throughout the model run. Almost from the beginning, the histogram is skewed towards the rift trend, and this skewness becomes more pronounced as extension proceeds. Plots of length vs. azimuth (Fig. 2.4) show that most faults with a rift-subparallel trend are short whereas the longest faults have a strike that is oblique to the displacement-normal direction, as is the case for the peak of the histogram of fault trends. The appearance of more rift-subparallel faults at 2.5 cm of displacement is a result of continued fault nucleation at the rift margins (see above).

2.4.2. $\alpha = 30°$

In the $\alpha = 30°$ experiment (Fig. 2.5), faults do not begin to appear at the model surface in significant numbers until 1.5 cm of displacement. From the very beginning, two sets of faults are evident. One set strikes in the displacement-normal direction and exhibits right-lateral oblique slip. The other set strikes in the rift-subparallel direction and exhibits left-lateral oblique slip. As in the $\alpha = 60°$ model, most of the first faults dip away from the moving wall. However, in contrast to the $\alpha = 60°$ model, none of the faults appear to begin as opening-mode fractures. Also, unlike the $\alpha = 60°$ model, the zone of

deformation starts out wider than the latex sheet, and faults appear to be more uniformly distributed across the width of the deformation zone. These first faults are relatively straight and have sub-vertical dips, initially showing only a small component of dip slip.

By 2.0 cm of displacement, it is apparent that faults at the rift margin have a different strike than the majority of faults in the rift center. All faults at the margin have a strike that is oblique to the rift-parallel trend, whereas the great majority of faults in the center of the rift have a strike that is displacement-normal. A subtle clustering also becomes apparent by 2.0 cm of displacement, particularly for displacement-normal faults (see section 3.7.1 in Chapter 3). Histograms of azimuth (Fig. 2.6) show a sudden increase in the number of of rift-subparallel faults by 2.5 cm of displacement. By 2.75 cm of displacement, the rift-subparallel faults form a distinct peak on the histogram; by 3.0 cm of displacement, they become more numerous than displacement-normal faults. Most faults with this trend are along the rift margins; however, by 2.5 cm of displacement, many are also present in the center of the rift zone. At first they tend to be short, isolated structures that fill the spaces between displacement-normal faults. As they increase in number, they begin to interact with displacement-normal faults, forming complex, anastomosing or branching structures (Fig. 2.7). During linkage, some rotate into an orientation that is perpendicular to the direction of maximum horizontal extension (E_{hmax}). Once in this orientation, they gain displacement rapidly (see fault shown in black in Fig. 2.7; also see section 3.7.2. in Chapter 3 for further discussion). Plots of length vs. azimuth (Fig. 2.8) reflect this interaction of two fault sets. By 3.25 cm of displacement, faults with a strike intermediate between rift-parallel and displacement-normal increase both in number and length as a result of linkage between these two sub-populations.

As in the $\alpha = 60°$ model, faults on the rift margin closest to the moving wall develop first. However, unlike the $\alpha = 60°$ model, they continue to nucleate throughout the model run and retain an average strike that is 20° oblique to the rift trend. Most fault growth on the rift margin is accomplished by tip propagation rather than linkage, so that faults here remain relatively short compared to those within the rift zone.

2.5. Discussion: Comparison of two models

The evolution of fault populations in these two models, one moderately oblique ($\alpha = 60°$) and the other highly oblique ($\alpha = 30°$), is quite different, and the differences are clearly attributable to rift geometry.

2.5.1. Fault nucleation

Because most fault nucleation occurs at some depth within the model, it cannot be observed. Therefore, the first appearance of a fault at the surface of the model lags behind nucleation by an unknown amount of time. For purposes of this study, I assume that the rate of appearance of new faults at the surface is proportional to the rate of fault nucleation. In both models, the number of faults generally increases with increasing displacement of the moving wall (Fig. 2.9). However, the rate of increase for the $\alpha = 60°$ model is much more variable than for the $\alpha = 30°$ model. The number of faults on the $\alpha = 30°$ model increases rather steadily through time, with the exception of a large jump (>100% increase) between 2.25 and 2.5 cm of displacement. In contrast, after 1.75 cm of displacement, the number of faults increases by 300% in the $\alpha = 60°$ model. Subsequent to this event, the rate of nucleation decreases, and, at 2.5 cm of displacement, it levels off.

This reflects a significant fault linkage event (see below). An increase in fault nucleation after 3.0 cm of displacement is confined to the rift margins (see above). At the same time, faults continue to nucleate at a steady rate in the $\alpha = 30°$ model, although increasingly more nucleation occurs on the rift margins as extension progresses.

2.5.2. Fault growth

The rate of fault growth is reflected in the summed length (ΣL) of faults and changes in the length of faults at the 95th percentile of length for all faults in the model (L_{95}; Fig. 2.11). Up until 1.75 cm of displacement, ΣL and L_{95} for the $\alpha = 30°$ model are approximately equal to the same data for $\alpha = 60°$. As extension proceeds, the rate of fault growth in both models becomes more rapid as a critical strain threshold is reached. This increase begins sooner and occurs at a higher rate in the $\alpha = 60°$ model. ΣL and L_{95} for this model follow a more or less parallel trend of steady increase.

For the $\alpha = 30°$ model, ΣL increases steadily throughout the model run, but L_{95} approaches its maximum value after only 2.5 cm of displacement. As discussed in Chapter 1 (Clifton et al., 2000), the angle of rift obliquity constrains the maximum length that faults can attain within the rift zone. In the early stages of evolution of the $\alpha = 30°$ model, faults with a displacement-normal trend cluster in parallel arrays. These become the longest faults on the model, but their growth is limited by the width of the rift zone. In fact, they can only become slightly longer than the width of the rift zone. These displacement-normal faults grow by tip propagation and along-strike linkage until, at 2.5 cm of displacement, they reach the edge of the rift zone where further growth is inhibited. It is only at this point that rift-parallel faults start to increase rapidly in number (see Fig.

2.6). The length of these faults is in turn limited by the presence of the long displacement-normal faults that span the width of the rift. Rift-parallel faults fill the gaps between clusters of displacement-normal faults and commonly terminate against them. In many cases, the two sets link to form complex, branching structures (Fig. 2.7). The tip-to-tip lengths of these complex faults is considerably shorter than their trace length, placing another constraint on maximum fault length. Fault tortuosity (ratio of trace length to tip-to-tip length) increases markedly for the $\alpha = 30°$ model as displacement increases (Fig. 2.12).

Fault growth in the $\alpha = 60°$ model is much less restricted. Up until 1.75 cm of displacement, growth is accomplished by tip propagation of small faults. However, because the faults in this model form diffuse clusters, they do not have to attain a very great length before linkage can begin. Through most of the model's evolution, growth is accomplished primarily by linkage of en echelon or stepping (en bayonet) arrays of faults. Faults that nucleate in parallel arrays, on the other hand, grow mainly by tip propagation and tend to remain relatively short (see Fig. 2.2). Therefore, tortuosity values do not increase very much during the course of extension (Fig.2.12). Fault geometry is such that the maximum attainable fault length is more than three times the width of the rift zone. By 2.5 cm of displacement, deformation becomes concentrated on these long faults, and nucleation of new faults is inhibited.

The growth of normal faults in extensional settings has been described as a four-step process (Peacock and Sanderson, 1991) that begins with isolated fault segments which do not overlap or interact. Segments begin to lengthen and interact via relay structures that comprise a zone of deformation connecting the footwall of one fault to the

hanging-wall of the other. As fault growth continues, relay ramps start to break down when small oblique transfer faults form along them. Eventually, a ramp is breached by a transfer fault and linkage is complete. Beyond a critical separation distance, relay ramps do not form and fault segments cannot interact (Trudgill and Cartwright,1994). The growth of segments which overlap by more than a certain amount will be limited (Aydin and Schultz, 1990). Fault growth is enhanced at the inward tips of underlapping segments, but even a small overlap will reduce the propagation tendency of fault segments (Willemse, 1997). Gupta and Scholz (2000) demonstrate that fault growth will cease on one segment when its tip propagates into the zone of maximum stress drop of the other segment.

The results presented here suggest that fault interaction begins at the earliest stages of fault population evolution, when the presence of the first faults appears to enhance nucleation of nearby faults. This effect is more pronounced and is evident sooner on the less oblique $\alpha = 60°$ model. Once diffuse clusters of small faults have formed in this model, their growth procedes in a manner similar to that descibed above. Fault tip zones interact via relay structures in the clay, but in most cases ramp breach is accomplished not by the formation of transfer faults but by the tip of one segment curving into either the hanging-wall or footwall of the other. Clusters of parallel faults form on the $\alpha = 30°$ model after about 2.0 cm of displacement. According to the fault growth models described above, not only should they not form, but their growth should be severely limited by their high percentage of overlap. Instead, these groups of parallel faults lengthen until their growth is stopped only when they reach the rift margin. Results of 3-D boundary element modeling (Willemse, 1997) suggest that overlapping faults can

continue to grow if their down-dip height is small relative to their lengths. In the case of the $\alpha = 30°$ model, maximum down-dip height is only 25% of maximum fault length.

2.6. Summary and conclusions

For both models examined in this study, fault population evolution begins with the nucleation of small isolated faults around random heterogeneities in the modeling medium. These first faults appear to enhance the nucleation of new faults close by so that a loose clustering evolves fairly early in the evolution of the fault population. However, the influence of rift obliquity is important even at this earliest stage. Clusters in the $\alpha = 30°$ model consist of a parallel arrangement of displacement-normal faults, whereas in the $\alpha = 60°$ model the clusters consist of faults arranged in a stepping fashion. This difference determines the style of growth that predominates in the model (Fig. 2.13).

Displacement-normal faults on the $\alpha = 30°$ model grow primarily by tip-propagation, with some along-strike linkage, until they span the width of the rift zone. Once those faults can no longer lengthen, the rift-subparallel faults begin to form in significant numbers, and linkage becomes an important mode of fault growth. Faults on the $\alpha = 60°$ model have to grow very little before they begin to overlap and form en-echelon arrays. This geometry enhances fault interaction and growth by linkage, and it is at this point (1.75 cm of displacement) that fault growth increases markedly. Deformation becomes localized on these long faults and nucleation of new faults slows down or ceases entirely.

Fault growth also differs on the rift margins of these two models. Fault geometry on the $\alpha = 60°$ model leads to linkage of faults that are no more than 10° oblique to the

rift trend. These become long, rift-parallel faults as extension continues. In contrast, faults on the margin of the $\alpha = 30°$ model form about 20° oblique to the rift trend and tend to remain short. In conclusion, the angle of rift obliquity places constraints on the style of fault growth from the earliest stages of fault population evolution.

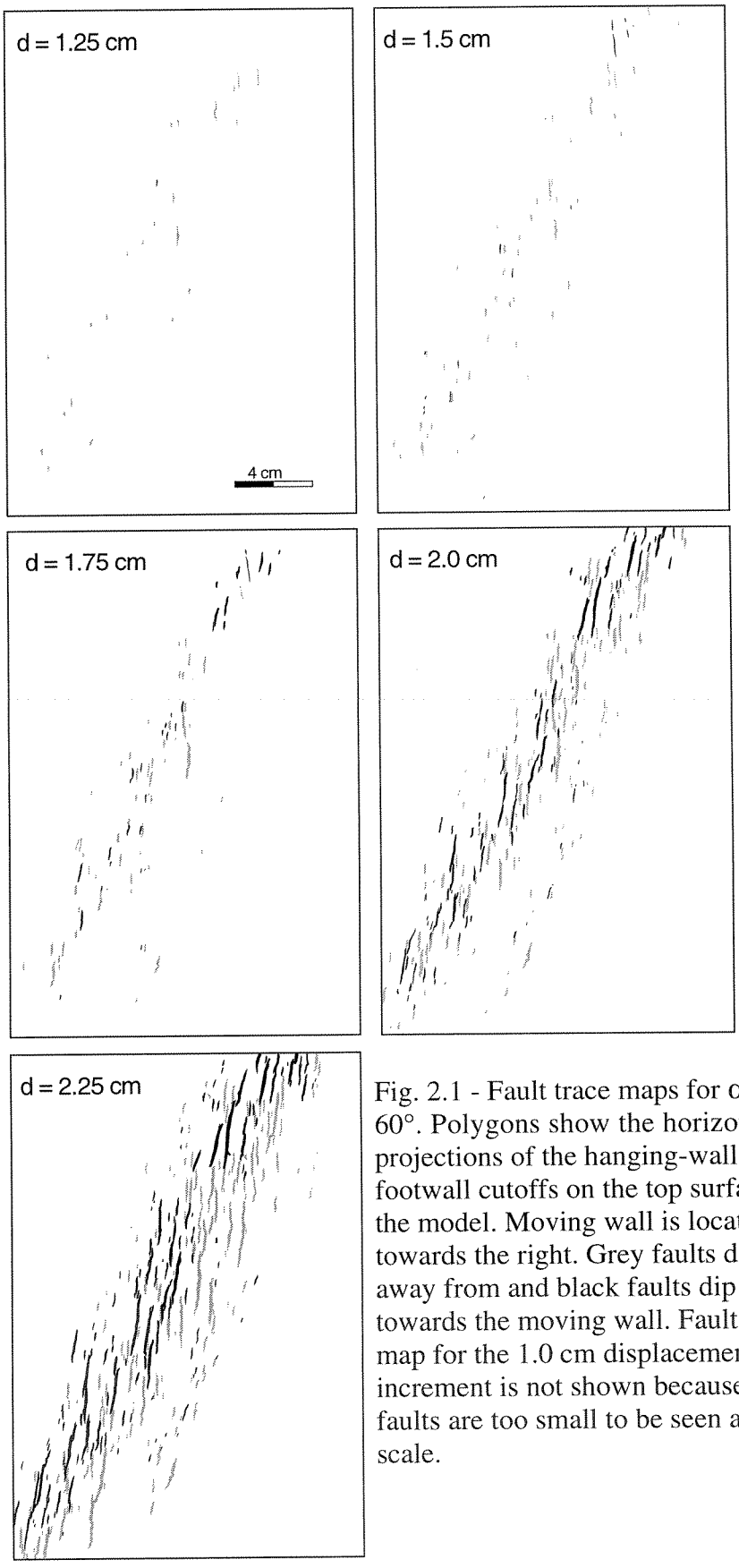


Fig. 2.1 - Fault trace maps for α = 60°. Polygons show the horizontal projections of the hanging-wall and footwall cutoffs on the top surface of the model. Moving wall is located towards the right. Grey faults dip away from and black faults dip towards the moving wall. Fault trace map for the 1.0 cm displacement increment is not shown because faults are too small to be seen at this scale.

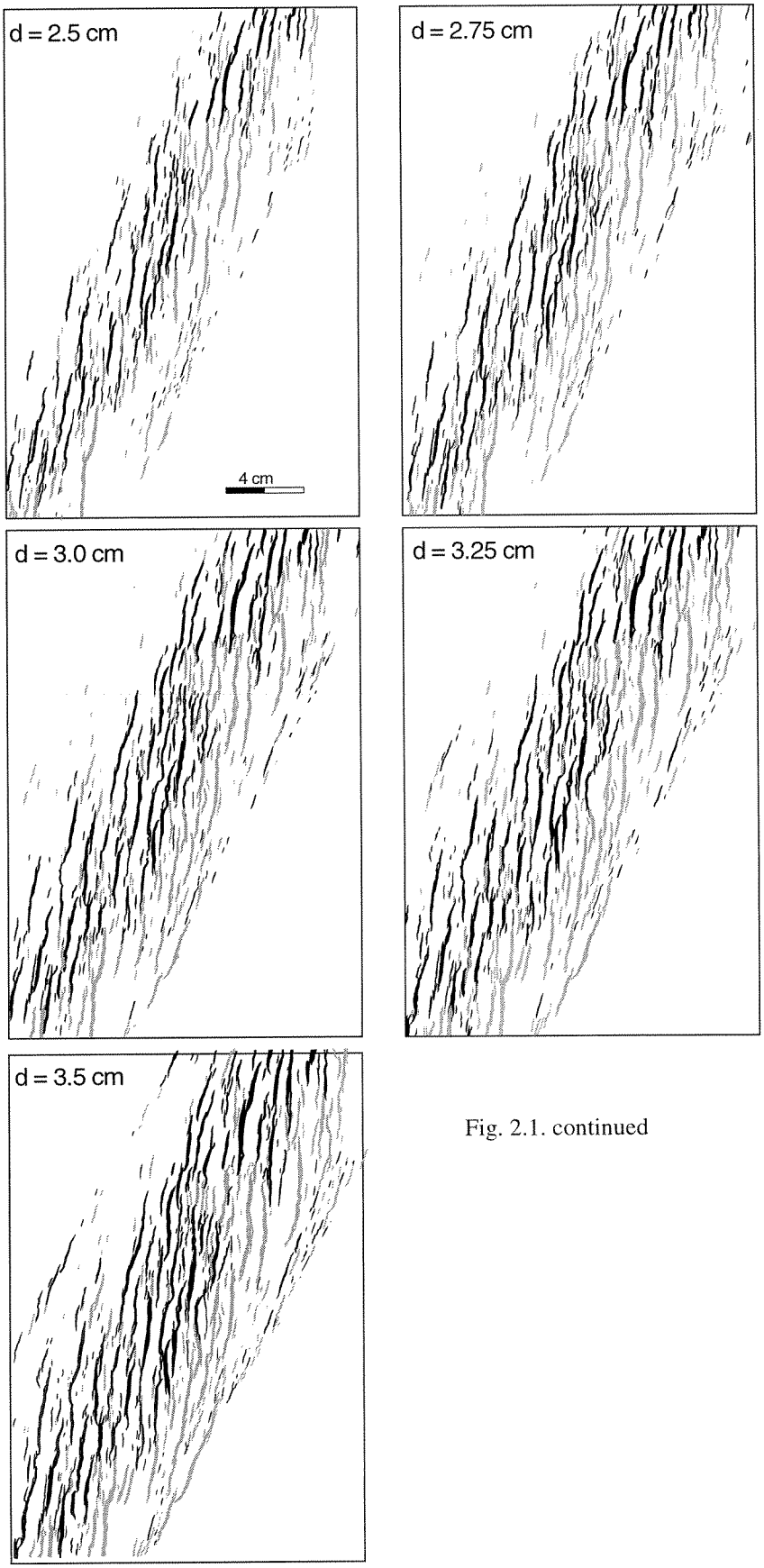


Fig. 2.1. continued

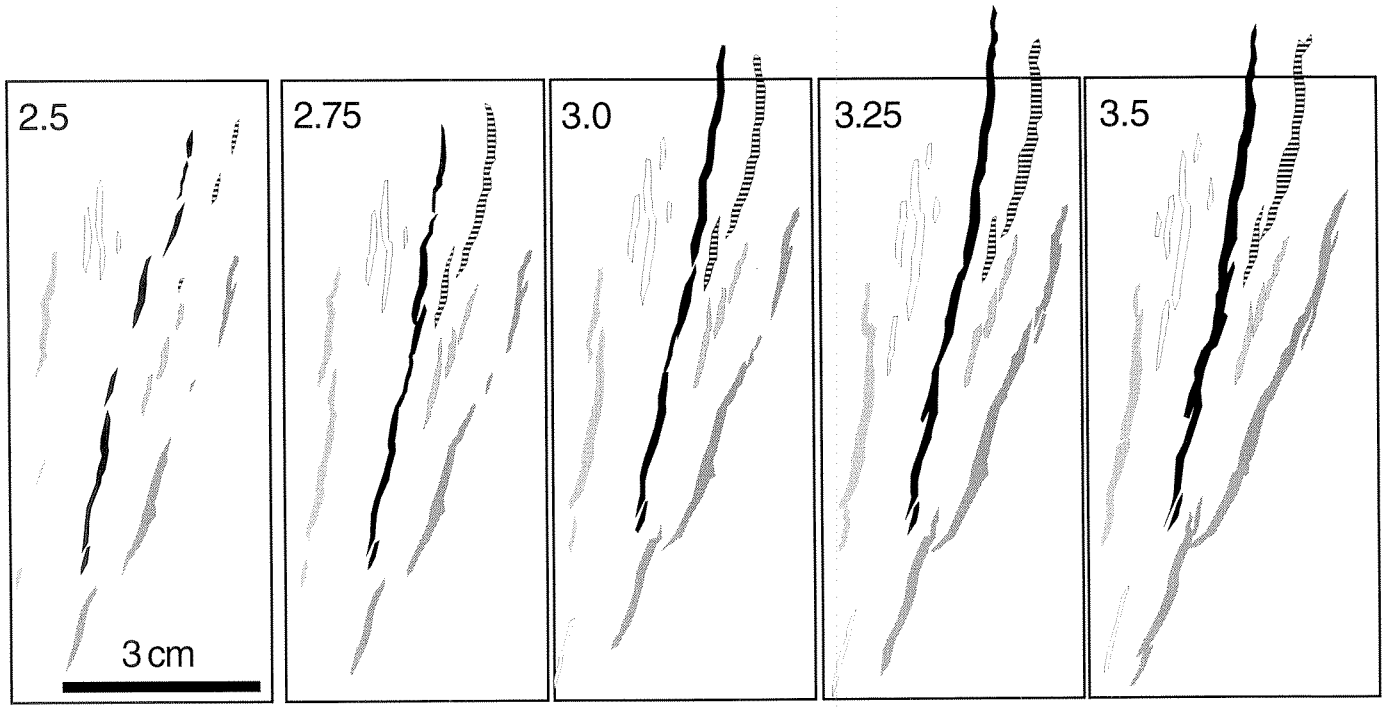


Fig. 2.2 - Enlarged view of fault growth and linkage for $\alpha = 60°$ model between 2.5 and 3.5 cm of displacement. Faults with the same color fill pattern link to form longer faults. Faults with black border and no fill pattern grow by tip propagation.

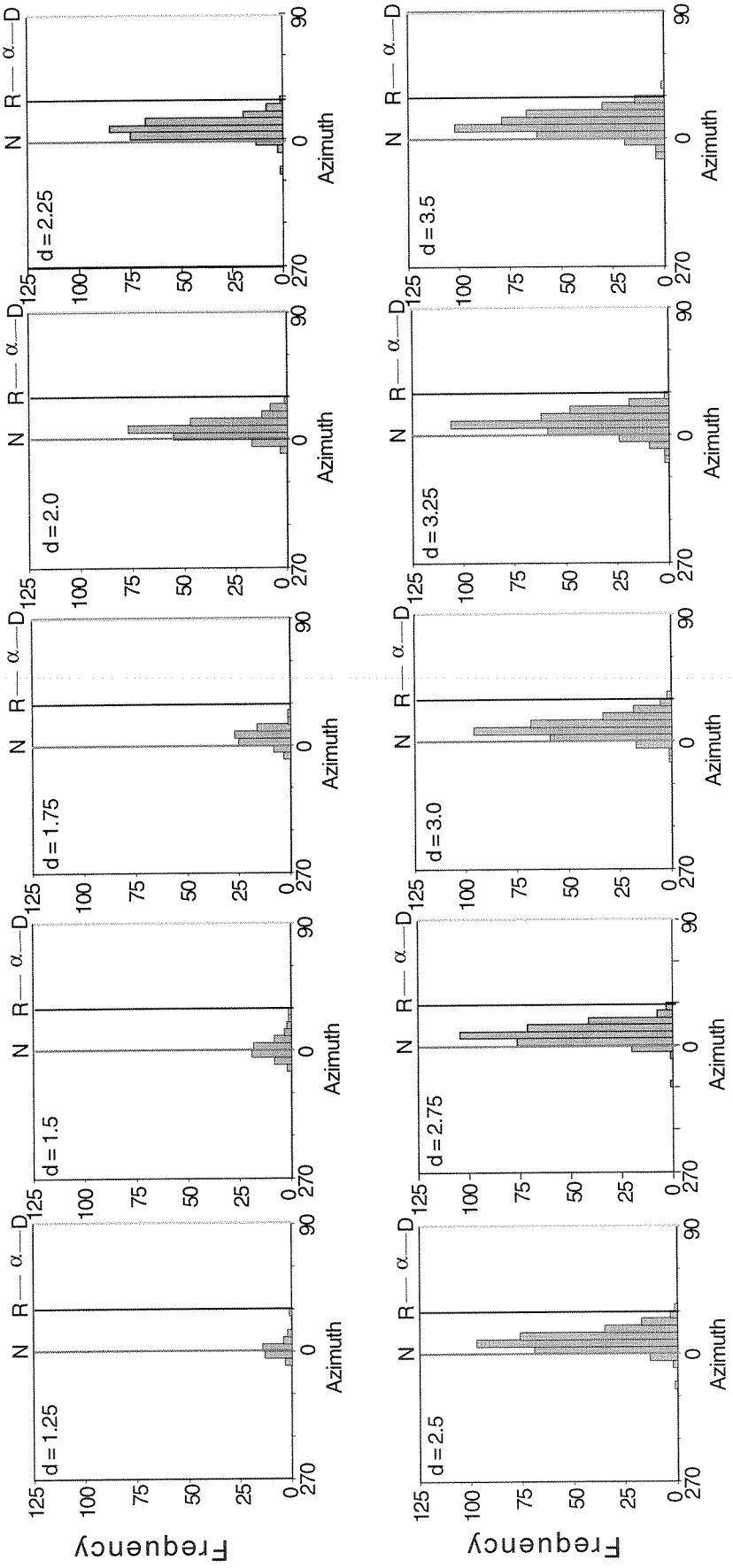


Fig. 2.3 - Histograms of azimuths for $\alpha = 60°$ models. N indicates the displacement-normal direction, R indicates the trend of the rift zone and D indicates the displacement direction.

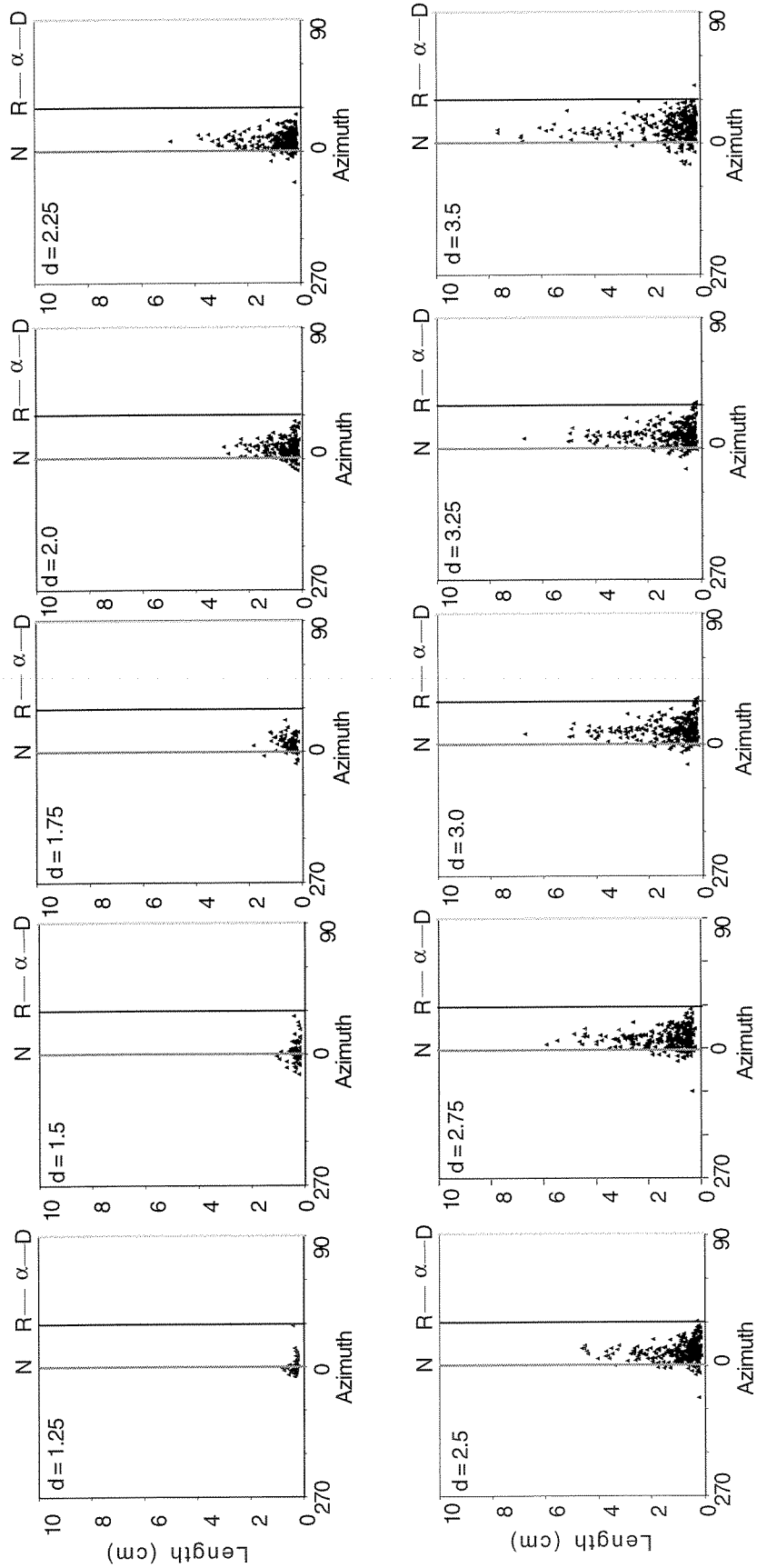


Fig. 2.4 - Plots of length vs. azimuth for $\alpha = 60°$ models. N indicates the displacement-normal direction, R indicates the trend of the rift zone and D indicates the displacement direction.

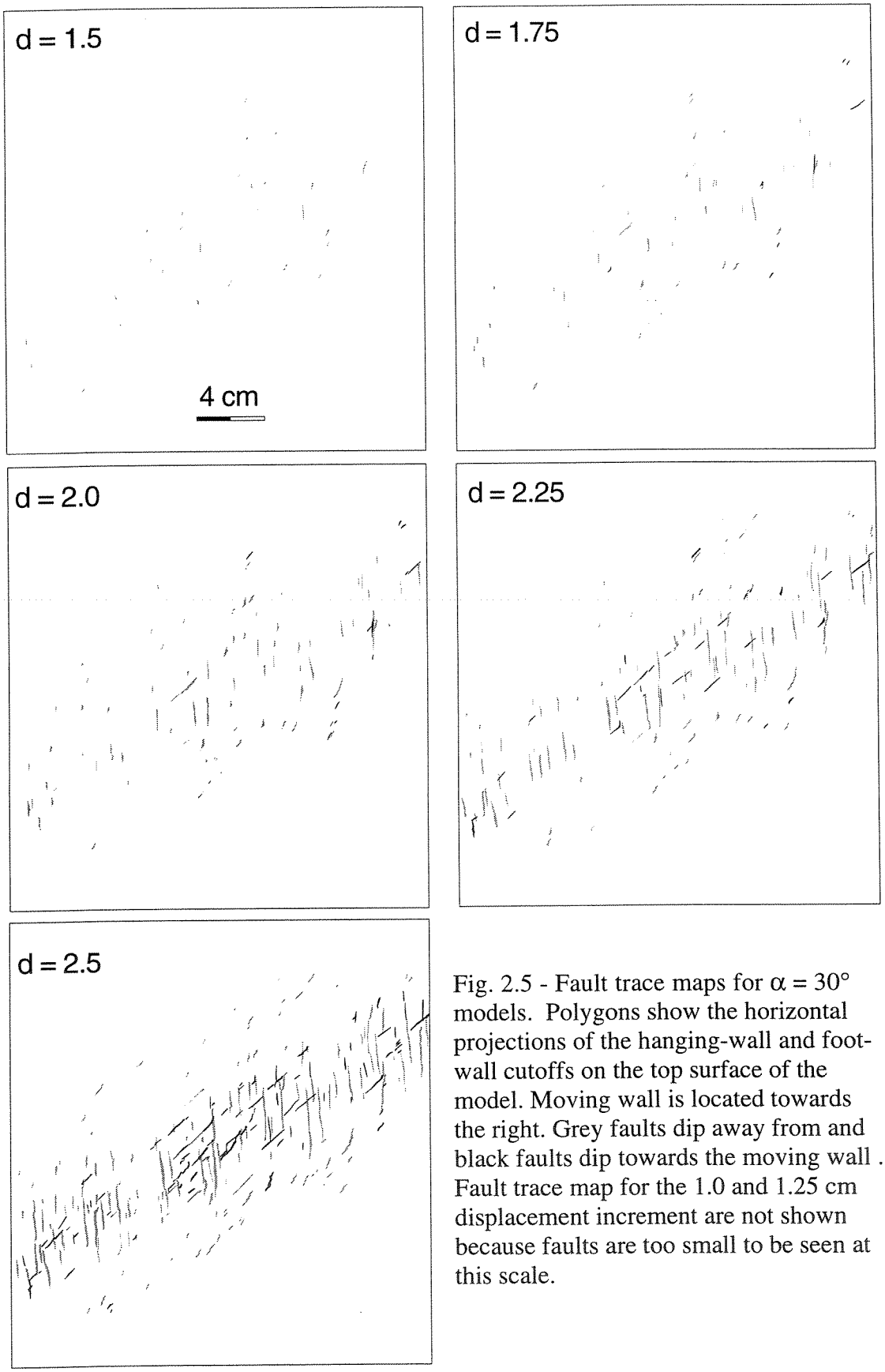


Fig. 2.5 - Fault trace maps for $\alpha = 30°$ models. Polygons show the horizontal projections of the hanging-wall and foot-wall cutoffs on the top surface of the model. Moving wall is located towards the right. Grey faults dip away from and black faults dip towards the moving wall . Fault trace map for the 1.0 and 1.25 cm displacement increment are not shown because faults are too small to be seen at this scale.

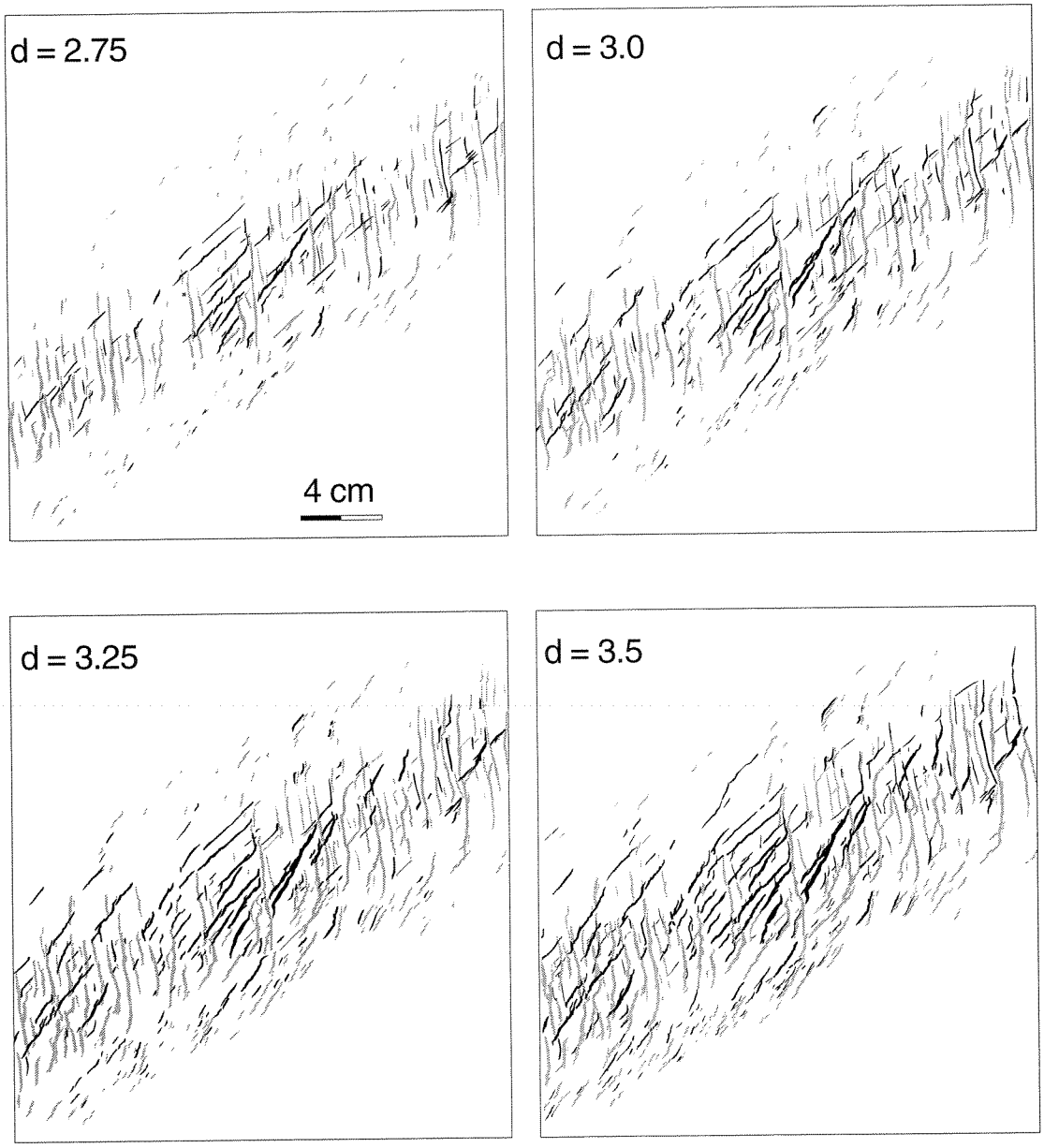


Fig. 2.5 -continued

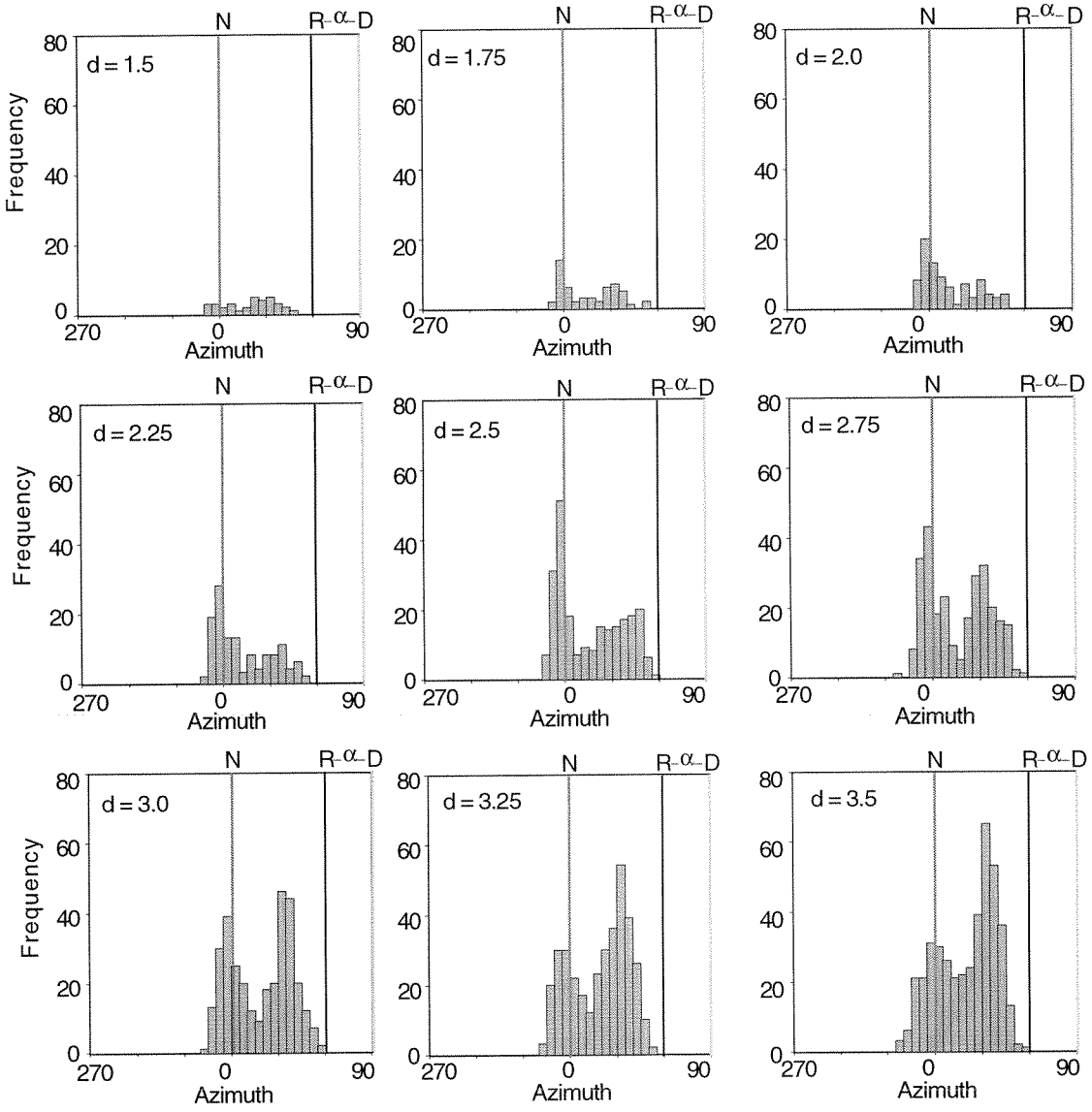


Fig. 2.6 - Histograms of azimuths for $\alpha = 30°$ models. N indicates the displacement-normal direction, R indicates the trend of the rift zone and D indicates the displacement direction.

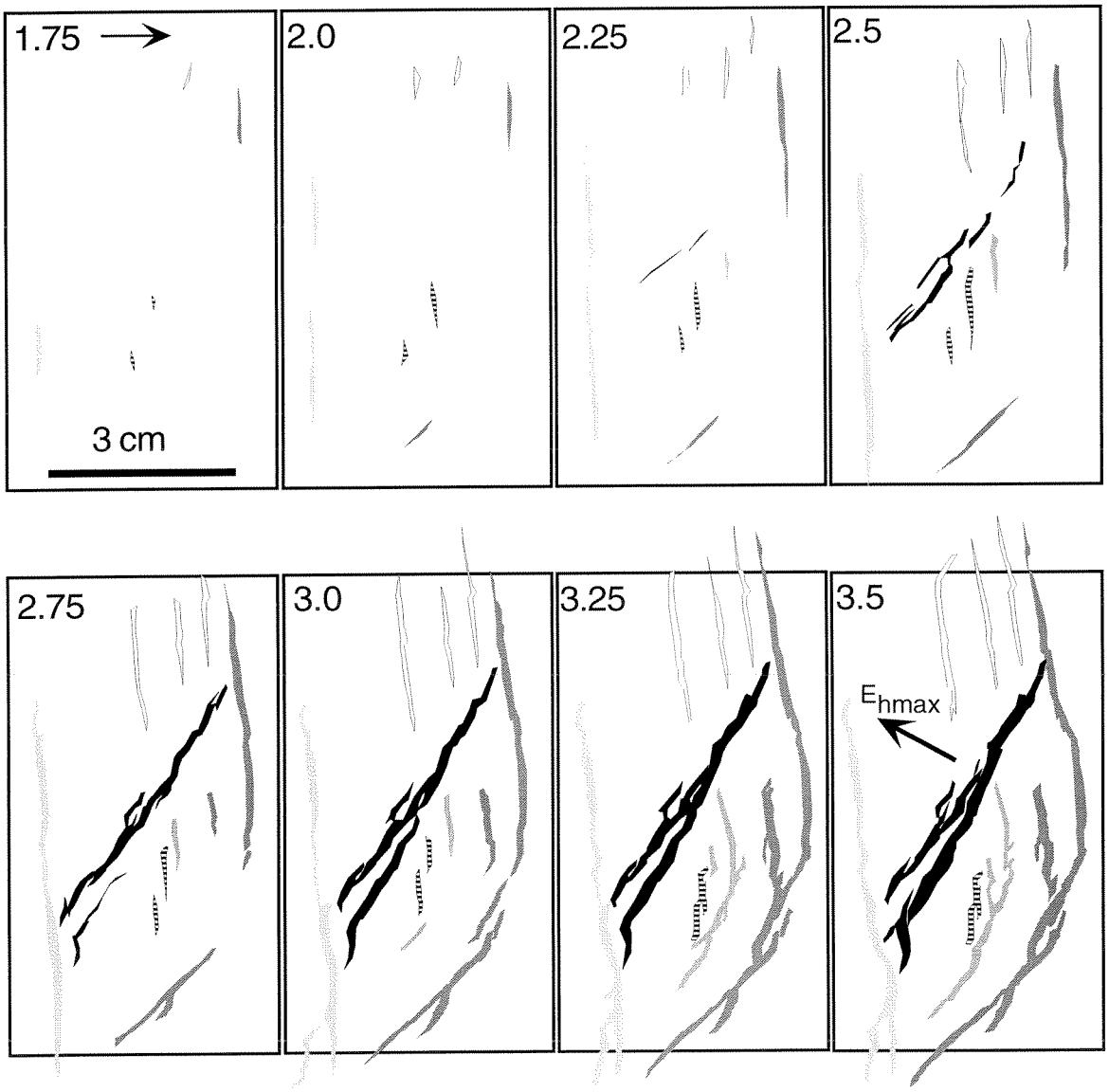


Fig. 2.7 - Enlarged view of fault growth and linkage for $\alpha = 30°$ model between 1.75 and 3.5 cm of displacement. Faults with the same color fill pattern link to form longer faults. Faults with black border and no fill pattern grow by tip propagation. Arrow shown at 1.75 cm of displacement shows the displacement direction. Arrow shown at 3.5 cm of displacement shows the direction of maximum horizontal extension (E_{hmax}).

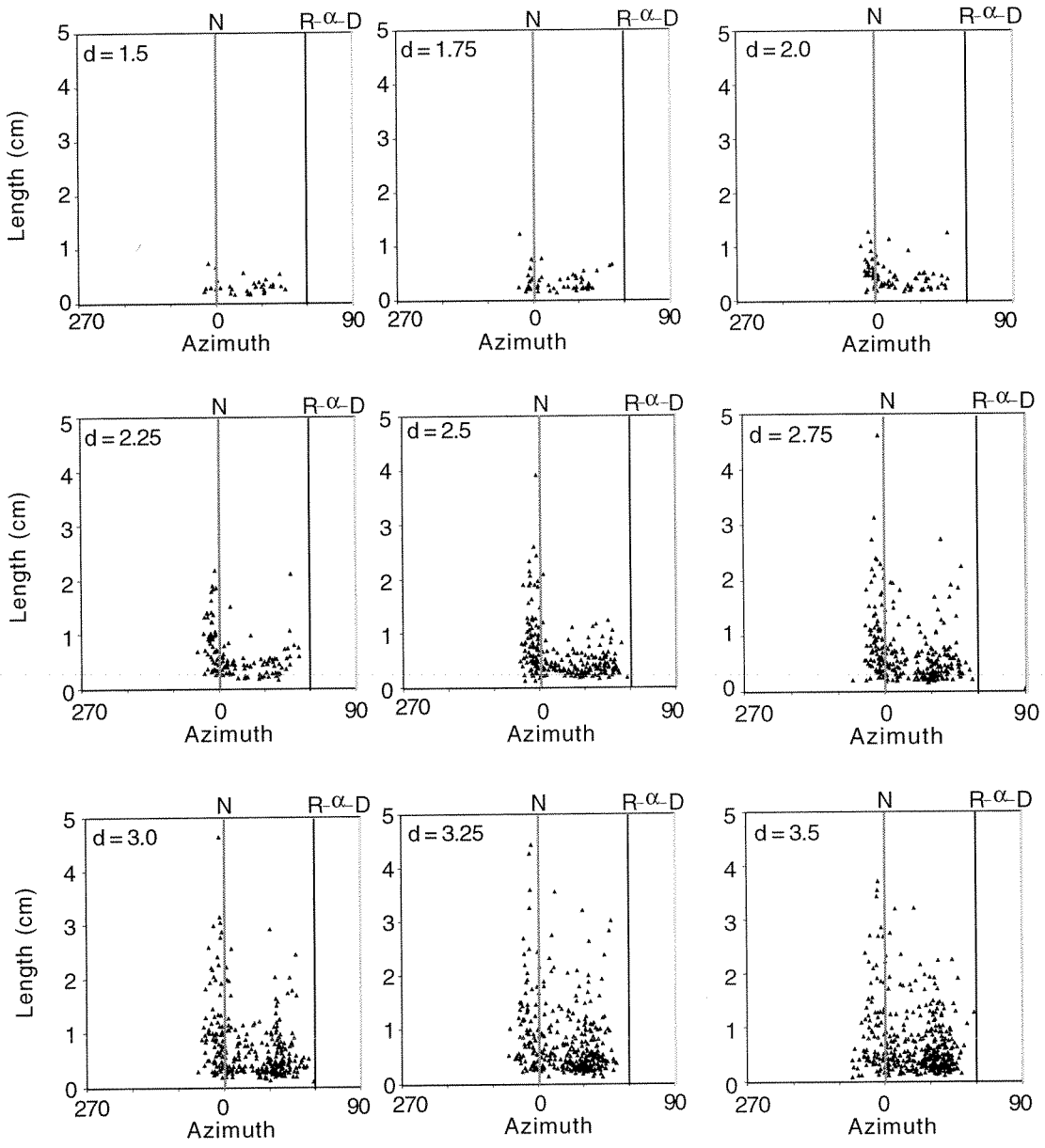


Fig. 2.8 - Plots of length vs. azimuth for $\alpha = 30°$ models. N indicates the displacement-normal direction, R indicates the trend of the rift zone and D indicates the displacement direction.

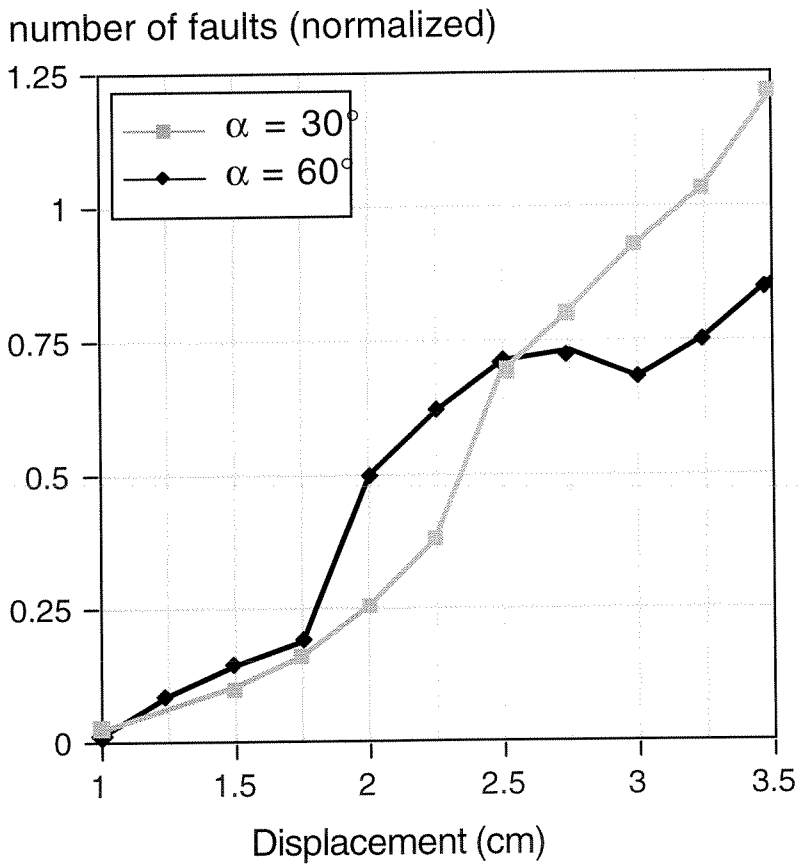


Fig. 2.9 - Summary plot showing how the number of faults changes in each model with increasing displacement. Data are normalized to the area of the deformed zone.

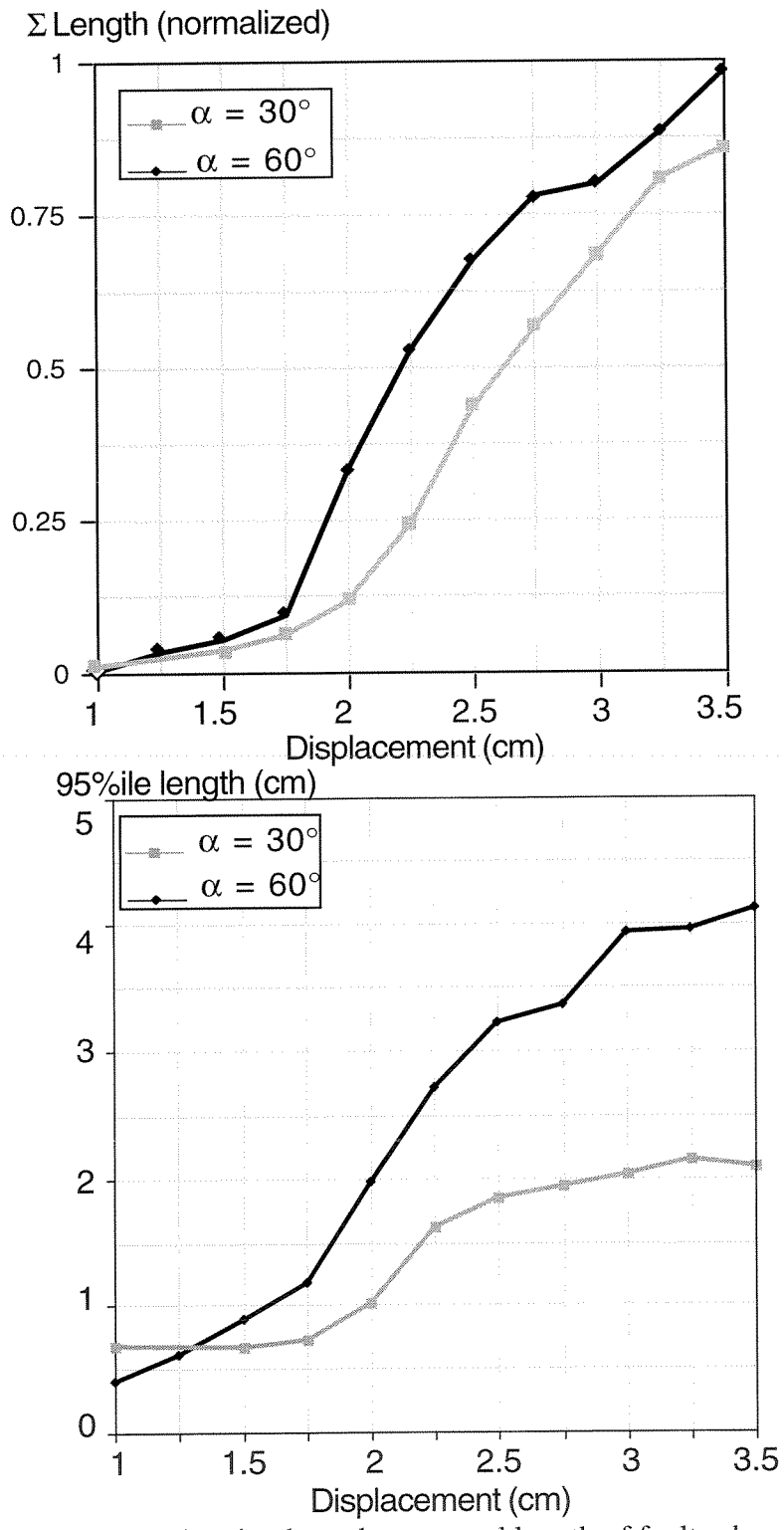


Fig. 2.10 - a) Summary plot showing how the summed length of faults changes through time in each model. Data are normalized by the area of the deformed zone. b) Summary plot showing how the 95th percentile of lengths changes with increasing displacement in each model.

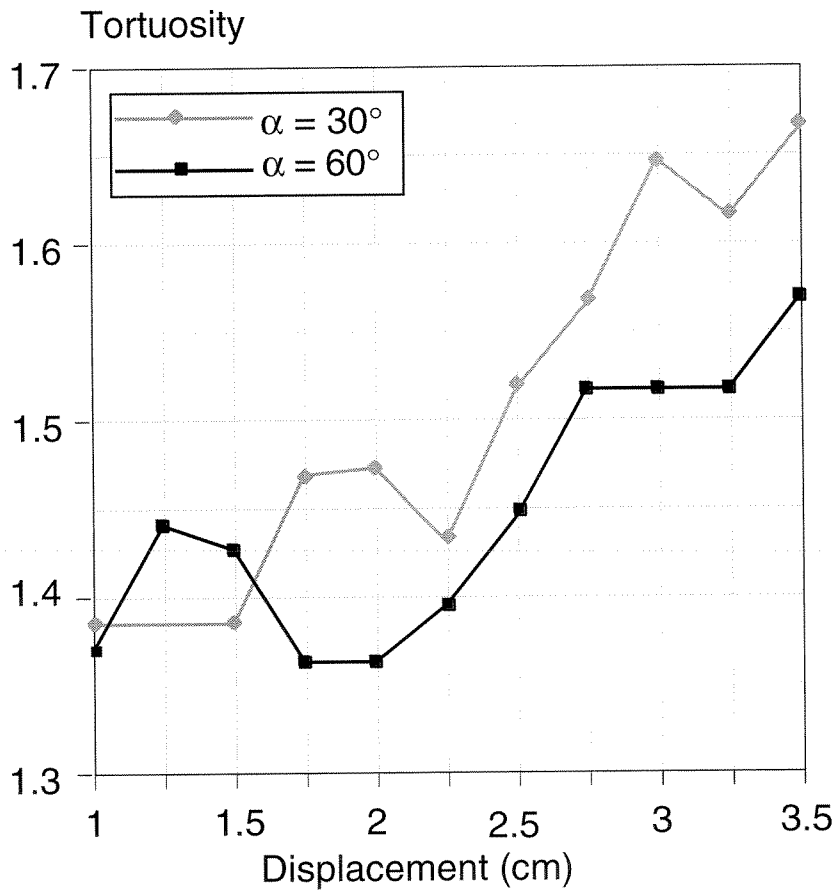


Fig. 2.11 - Summary plot showing how tortuosity changes with increasing displacement in each model.

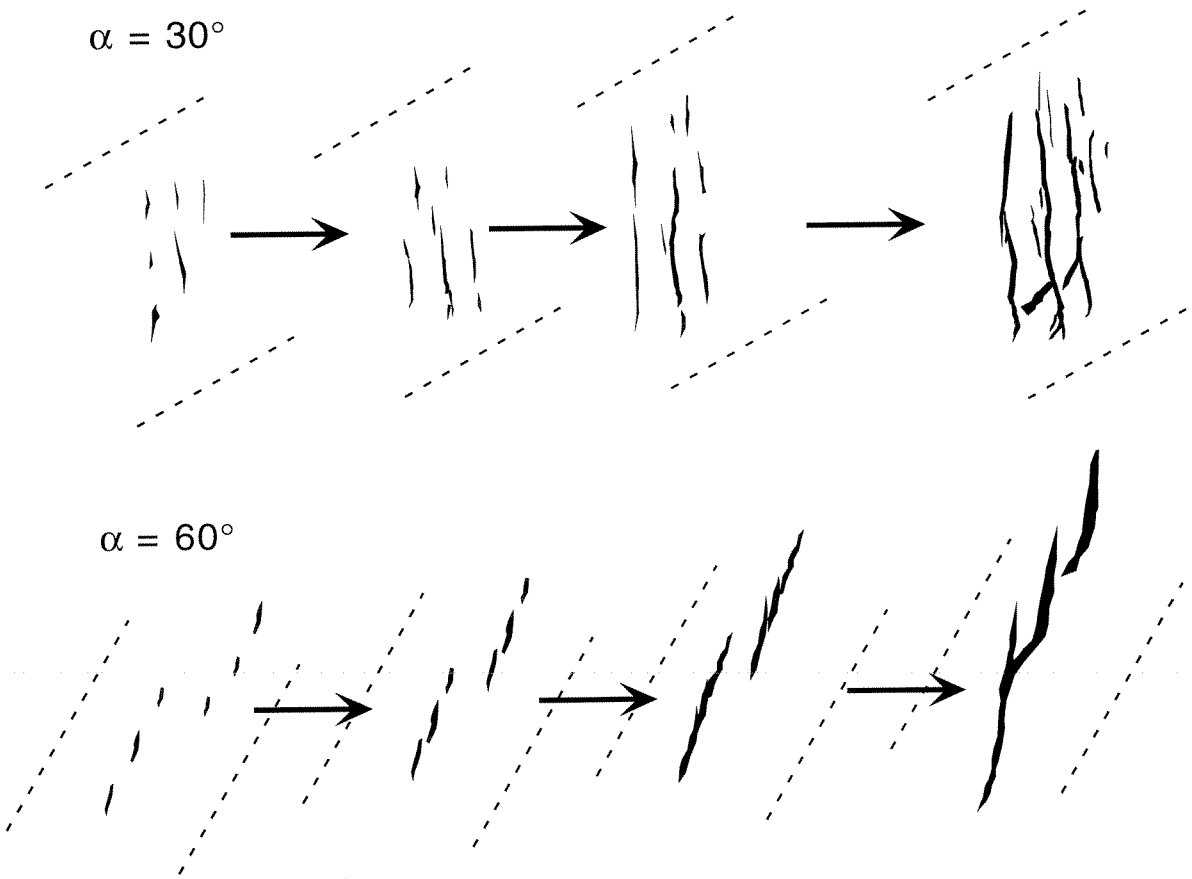


Fig. 2.12 - Cartoon demonstrating the style of fault growth in each model. Dashed lines show rift trend.

Chapter 3 – Population systematics of fractures in the Reykjanes Fissure Swarm, SW Iceland: comparison with experimental clay models of oblique rifting

3.1. Abstract

Population systematics for the Reykjanes Fissure Swarm suggest that fractures are unevenly distributed in time and space in this volcanic zone. Along the margin, fractures are long, highly segmented fissures and normal faults with offset on the order of several meters and an average strike 20° oblique to the trend of the plate boundary (rift axis). In the center of the zone of active volcanism, fractures are generally shorter, straighter, fewer in number and strike approximately perpendicular to the direction of maximum horizontal extension (parallel to the trend of eruptive fissures). Right-lateral oblique-slip faults striking in the spreading-normal direction are present in the center of the rift zone. Results from a scaled experimental model suggest that a significant change in fracture strike at the rift margins is due to the presence of a secondary stress field at the boundary between a weak (highly stretched) and strong (unstretched) crust. The model confirms that right-lateral oblique- or strike-slip faults accommodate a significant amount of left lateral shear across oblique rift zones.

3.2. Introduction

The Mid-Atlantic Ridge (MAR) defines the boundary between the North American and European plates. Its topography is usually quite rough, with high rift mountains bordering a down-faulted median rift valley (e.g., Vogt, 1986). However, the rift valley gradually disappears as the ridge approaches the major hot spots of the Azores and Iceland. Global studies of mid-ocean ridges have revealed that major differences in

ridge morphology can often be attributed to spreading rate. However, overall magma budget (Sempere et al., 1990) and segment orientation with respect to the direction of plate motion (Taylor et al., 1994) also play critical roles in determining the structural architecture of a particular ridge segment.

The segment of the MAR north of the Charlie Gibbs Fracture Zone (CGFZ in Fig. 3.1) is known as the Reykjanes Ridge. North of latitude 57°N, the ridge bends and takes on a trend of 035° so that it is oblique to the direction of plate motion which varies along the length of the ridge from 096° to 100° (DeMets et al., 1994). The acute angle, α , between the rift trend and the direction of plate motion is approximately 60°. At latitude 58°30'N, the topography of the ridge becomes smoother and its median valley disappears, due to a change in lithospheric rheology and an increased magma supply as the ridge approaches the Iceland mantle plume (Malinverno, 1993). At latitude 63°48'N, the ridge comes onshore at Reykjanes Peninsula, Iceland. Here it bends sharply to the east so that it becomes approximately 30° oblique to the direction of plate motion.

Our understanding of how Reykjanes Peninsula fits into the plate tectonic model has evolved considerably, as the model itself has evolved, over the past thirty years. Because of its geometry with respect to adjacent portions of the MAR, early researchers (e.g.Ward, 1971, Courtillot et al., 1974) believed the peninsula to be a transform fault, but problems arose with that model when no through-going strike-slip fault could be found. Nakamura (1970) was one of the first researchers to suggest that it is an oblique rift zone. Based on the geometry of en-echelon extensional structures examined both in the field and with air photos, he proposed that the rift zone undergoes equal amounts of extension and shear, perhaps discontinuously in the short term, but accomplishing the

"average" plate motion in the long term. The tectonic setting and state of stress are now fairly well established and characteristics of both transform and ridge segment are evident. Still unclear are some of the dynamics of this zone, how faulting and magmatism are related in time and space on the Peninsula, how the structures we see at the surface are related to the processes that formed them and what role ridge geometry (i.e., the angle of rift obliquity) plays in the tectonic development of a spreading segment.

Scaled physical models have been used to interpret the geometry and evolution of fracture populations that form on mid-ocean ridges during oblique extension. Dauteuil and Brun (1993, 1996) compared their sand over putty models to the Mohns Ridge, which is 45° oblique to the spreading direction. Applegate and Shor (1994) compared their fracture data for the Reykjanes Ridge to the clay models of oblique rifting of Withjack and Jamison (1986) and the sand-over-putty models of Tron and Brun (1991). All authors noted that the scaled models accurately predict the fault geometry that is present on these oblique ridge segments. The $\alpha = 30°$ model produced in this study, discussed at length in Chapters 1 and 2, is a good experimental analogue for the Reykjanes Peninsula. The models represent distributed deformation of a thin brittle layer above a narrow zone in the substrate that deforms ductilely, analogous to the deformation on the peninsula. Although the models cannot reproduce the deformation resulting from magma injection, they can predict the fracture pattern that results exclusively from far-field tectonic stresses in the absence of magma.

A goal of this study is to determine how the fissure swarms on Reykjanes Peninsula have formed and evolved, by examining the population systematics of fractures in the Reykjanes fissure swarm at different scales and in lava flows of different ages. By then

comparing field data to the experimental model data, we can distinguish the deformation that results principally from remote plate stresses from the deformation related mainly to local, magmatic phenomena. The geometry, evolution and spatial distribution of fractures that form in the experimental model can be used to better understand the structures we see on the Reykjanes Peninsula and the sequence of events that generated them.

3.3. Tectonic Setting and Geologic Background

The center of the Iceland mantle plume lies under the Vatnajokull glacier (Wolfe, et al., 1997) and probably has a major influence on the geometry of the plate boundary in Iceland (see Fig. 3.1). The plate motion direction varies in Iceland from 102.74° at Reykjanes Peninsula to 106.21° along the Northern Volcanic Zone according to the NUVEL-1A model (DeMets et al., 1994). According to the classification of Macdonald (1998), the volcanic zones in Iceland are second-order ridge segments that are approximately 100 km in length and separated from each other by either a segment overlap or a change in strike direction ("rift valley jog"). Each segment has a different orientation with respect to the direction of plate motion and each has a unique character. Along with differences in their magma budget, their differing orientations can account for many of the structural differences between these ridge segments.

A major ridge jump approximately 6-7 million years ago initiated active spreading on Reykjanes Peninsula (Saemundsson, 1979; Johannesson, 1980). A narrow zone of seismicity having an average trend of 075° runs along the length of the peninsula and has been used to define the active plate boundary (Klein et al., 1977; Einarsson, 1991). This zone intersects fissure swarms near the zone of maximum volcanic production and seems

to control the location of geothermal areas on the peninsula (Einarsson, 1991). The peninsula is characterized by arrays of eruptive fissures, spaced on average approximately 5 km apart, and having an average strike of 040° (Fig. 3.2). These have been described in the literature as comprising four distinct volcanic systems (Fig. 3.3; Einarsson and Saemundsson, 1987), each with their own magma supply and high temperature geothermal system.

Sub-glacial and sub-aerial (post-glacial) fissure eruptions have formed prominent NE-trending ridges and crater rows that dominate the topography of the peninsula (Fig. 3.4). Sub-glacial eruptions produce ridges of hyaloclastite that bear an unmistakable resemblance in volume, height and aspect ratio to the Axial Volcanic Ridges (AVRs) that have been described along the Reykjanes Ridge (Murton and Parson, 1993; Searle et al., 1998). A number of table mountains and hyaloclastite cones, products of sub-glacial eruptions from isolated vents, are also present on the peninsula and closely resemble the small seamounts that have been mapped on the MAR. Early post-glacial basaltic (large volume) and picritic (small volume) shield volcanoes have also played a major role in surfacing this ridge segment with voluminous pahoehoe lava flows, which both cover and are covered by the products of fissure eruptions. Shield volcanoes and eruptive fissures have been active on the peninsula during the Holocene, but the last known eruption was in the fourteenth century (Saemundsson, 1995).

Deformation on the peninsula (Fig. 3.2) is accommodated by extensional features that include normal faults, opening mode fissures, and small graben structures (25 to 40 meters wide) that have been closely associated with the eruptive fissures and used to define the boundaries of volcanic systems (see Fig. 3.3; Saemundsson, 1979;

Gudmundsson, 1980). The base of the seismogenic zone is between 5 and 11 km on the Peninsula (Einarsson, 1991) and most seismicity occurs at depths from 1 to 5 km. A narrow zone of seismicity 2 to 5 km wide, characterized by predominantly strike-slip focal mechanisms and extending the entire length of the peninsula, was identified by Einarsson (1991) as the currently active plate boundary. In the eastern part of the Reykjanes Peninsula, seismicity is characterized by focal mechanisms indicating right-lateral strike-slip faulting on N-S planes or left-lateral strike-slip faulting on E-W planes. However, seismicity on the western part of the peninsula is principally characterized by normal faulting on NE-striking planes (Einarsson, 1991). During a large earthquake swarm in 1972, focal mechanisms ranged from normal to oblique to strike-slip faulting (Klein et al., 1977). Geodetic measurements between 1986 and 1998 (Sturkell et al., 1994; Hreinsdottir et al., 1999) show that left-lateral shear is currently accumulating on the peninsula. Data from Satellite Radar Interferometry support this and indicate that below a depth of 5 km plate motion is accommodated by continuous ductile deformation (Vadon and Sigmundsson, 1997).

The Reykjanes fissure swarm (RFS) is located in westernmost Reykjanes Peninsula (Fig. 3.5). It includes three en-echelon sets of eruptive fissures spaced between 2 and 3 km apart. They are, from west to east, the Stampar, Eldvorp and Sundhnukur (after Jonsson, 1978) eruptive fissures, all of which have been active in historic time. Normal faults, hybrid fractures and opening-mode fissures are associated with the eruptive fissures, but most occur on the edges of the area of eruptive activity. This fissure swarm was chosen for study because of the excellent exposures of fractures in sparsely vegetated post-glacial lavas and easy accessibility to large numbers of fractures. Farther to the east,

above. He suggested that fractures originally formed during the Pleistocene from cyclic loading and unloading due to glaciation over weak, thin crust. He believed that most major faults formed in early post-glacial time, after the final retreat of the glaciers, and that virtually all faulting since then has involved reactivation of these same structures. Based primarily on detailed mapping of fractures at the Vogar graben, he outlined a process for the growth of post-glacial fractures that involved en echelon columnar joints opening above buried Pleistocene faults, then lengthening by tip propagation and linkage, and finally propagating to a depth at which they become normal faults.

3.5. Data collection

Data for fracture lengths and azimuths were collected both from air photos and in the field. The areas of Vogar, Grindavik and Stora-Sandvik/Reykjanes were chosen to examine based on availability of photos and accessibility to the field areas. Fracture spacing was measured only in one area.

3.5.1. Air photos

Air photos for all three areas were scanned and analyzed using ERDAS Imagine software (see appendix A). Resolution of the photos was 1 meter per pixel. I used the orthorectified air photos to generate fracture maps from which I was able to measure tip-to-tip azimuth and tip-to-tip length with accuracy on the order of meters. To check the accuracy of measurements made from the air photos, a selection of measurements were checked in the field with tape and compass. Using the air photos, I made an initial attempt to distinguish true normal faults from hybrid fractures and opening mode

much of the activity from eruptive fissures was sub-glacial, resulting in rugged topography and significant post-glacial sedimentary cover that pose problems for field work. The fractures analyzed in this study intersect lava flows ranging in age from 12,500 to 600 years BP (Saemundsson, 1995) allowing a first-order determination of the temporal evolution of the fracture population.

3.4. Previous Work

Kazuaki Nakamura (1970) conducted the first systematic study of fractures on Reykjanes Peninsula using air photos at a scale of 1:36000 and extensive field measurements. He was struck by the abundance of en-echelon extensional structures and noted that those having a left-stepping geometry trend more easterly whereas those with a right-stepping geometry trend more northerly. His histograms of azimuths (Fig. 3.6) show a difference of 30° between left-stepping and right-stepping fractures. The histograms overlap (dashed line) along what he calls the "general trend" (represented by the average trend of crater rows). He also noted that non-eruptive fissures cut older rocks than the crater rows and that displacement along faults is greatest in the oldest rocks, outside the zone of active volcanism. Based on these observations, he concluded the Reykjanes Peninsula to be an oblique rift zone experiencing equal amounts of strike-slip and dilation over time.

During the 1980's, Agust Gudmundsson published several papers on the formation of fractures on Reykanes Peninsula (Gudmundsson, 1980, 1986, 1987a, 1987b). He proposed that the fissure swarms formed when glacial rebound triggered inflation of elliptical magma chambers causing uplift and bending of the brittle crust

fissures, but subsequent fieldwork proved that many structures are in fact complex combinations of all three modes of rupture. In addition, some of the smaller features that I had determined to be fissures from the air photos alone, turned out to be small-displacement normal faults when examined in the field. Therefore, fractures of different mode are treated in this study as one statistical population, and data for all modes are combined. This is justified for several reasons. Based on his study of Tertiary and Pleistocene faults in Iceland, Gudmundsson (1992) has suggested that the large-scale tension fractures which form near or at the free surface propagate downward to a depth of 400 m, at which point they turn into normal faults. Field relationships point to the fact that all of these fractures form closely in time and space in response to the same stress system. In addition, field evidence from this study indicates that faults and fissures interact throughout their growth and often link to form complex structures.

For purposes of this study, I have used the same criterion as Gudmundsson (1987a), whereby any continuous trace of ground rupture is considered an individual fracture. By following the fracture trace at the pixel level, I was able to identify fracture tips with confidence in most cases. Fractures as short as 4 meters in length and less than 1 m wide are clearly resolvable on the air photos; field checking confirmed the accuracy of measurements within 1 m (50 cm at either tip). In spite of the high resolution of the photos, it is certain that small fractures were inevitably missed in areas of particularly thick moss and grasses and in areas of windblown sand.

Most of the longest structures exhibit the characteristics of segmented fault systems (e.g., Trudgill and Cartwright, 1994; see Chapter 1). Many large structures that have been mapped as single fractures at the regional scale (e.g., Saemundsson and Einarsson,

1980) are in fact made up of shorter segments which either overlap or are arranged along strike with gaps of a few meters between them. I attempted to identify segment boundaries along several "major" fractures (greater than 400 meters in length) visible on the air photos for each sub-area. Criteria developed for use with clay models in Chapter 1 were used to identify segment boundaries on the air photos as follows: 1) abrupt changes in fracture strike (>10° of azimuth), 2) abrupt, noticeable changes in fault displacement profiles, 3) abandoned splays, and 4) stranded footwall or hanging-wall rider blocks. Field checking showed that segment boundaries were identified correctly in most cases, but scarp degradation occasionally made it difficult to determine if a location was truly a segment boundary.

3.5.2. Field data

Molvik is a small graben directly south of the Eldvorp eruptive fissure and is included on the Stora-Sandvik/Reykanes air photo (number 4 on Fig.3.5). An Electronic Total Station was used to map the topography of this graben and all visible fractures around three normal faults, using the equipment and procedure described in Schlische and Ackermann (1998). The three normal faults are propagating through a ponded lava flow. The smooth, relatively unvegetated surface of the ponded flow allowed even the smallest cracks to be easily visible. This was particularly true in a wide relay ramp that had developed between two of the faults. Accuracy of the instrument is at the millimeter scale; however, strong winds and slippery rock surfaces at the field site made it impossible to hold the prism pole steady at all times. This error is difficult to quantify and varied from day to day with the weather conditions, but it is thought to be <2 cm.

For this location, fractures were classified as either fault, fissure or generic fracture based on the following definitions. If shear displacement was more than 5 centimeters and was continuous along the trace of the fracture, it was identified as a fault. If there was no perceptible, continuous shear displacement and aperture was greater than 5 millimeters, a fracture was identified as a fissure. Any other continuous "crack" was considered a generic fracture. Fractures were distinguished from columnar cooling joints mainly by their continuity (Fig. 3.7). Fractures surrounding columnar joints were not measured. However, if a fracture followed three or more contiguous columns along strike, it was measured and, depending on its aperture was classified as either a fissure or generic fracture.

3.6. Data

3.6.1. Geological Descriptions

3.6.1.1. Vogar

The area referred to as the Vogar graben lies near the village of Vogar, along the northern coast of western Reykjanes Peninsula (Fig. 3.8). It is on the northwestern edge of the Reykjanes fissure swarm, outside the area of eruptive fissures. It lies mostly within a single compound lava flow erupted from the Thrainsskjoldur shield about 12,500 years BP (Saemundsson, 1995). The study area is approximately 37 square kilometers and was analyzed using air photos at a scale of 1:25,000.

The graben structure is only present in the northern part of the map area, where the fault known as Hrafnagja defines its northwest boundary. The graben axis trends northeasterly. From Hrafnagja to the southwest, the graben both deepens and widens to a maximum

width of 2 km where it becomes covered by early Holocene lavas and historic lavas from the Eldvorp crater row. Therefore, its southern extent cannot be defined. The graben structure narrows and shallows to the northeast and dies out approximately 5 km northeast of the turnoff to the village of Vogar along Road 41. The remainder of the map area consists of tilted fault blocks with steeply dipping faults facing to the northwest, away from the rift center.

All fractures examined in this area cut early post-glacial Thrainsskjoldur shield lavas. Field evidence confirms that fractures in the southwestern part of this study area were present when the Thrainsskjoldur lavas were erupted, and that, at least in that part of the graben, little movement has occurred along those fractures since the eruption of those lavas. Here, pahoehoe flows drape long, smooth, curvilinear fault scarps along which any possible evidence of segment linkage has been either eroded or covered up (Fig. 3.9). These faults bound a small inlier of interglacial shield lavas. The presence of pillow breccia and scoria at the base of the fault scarp shown in Figure 3.9 indicate that lava flowed over the fault and into a lake. Several small, fault-bounded lakes are currently present here. Subsidence along faults in the northeastern part of the study area, on the other hand, has been significant since early post-glacial times. The longer fractures here are complex, highly segmented faults that change character frequently along strike and commonly display a zigzag geometry (Fig. 3.10). Maximum throw measured in this study along a single normal fault is 18 m and average throw for all normal faults in the graben is 4.7 m (Gudmundsson, 1986).

3.6.1.2. Grindavik

The area referred to here as Grindavik (Fig. 3.11) lies just to the west and outside of the town of Grindavik, along the south coast of Reykjanes Peninsula in the southeastern part of the Reykjanes Fissure Swarm. Air photos of this area are at a scale of 1:14,400 and cover an area of 11square kilometers. Fractures here are exposed mainly in pahoehoe lavas of the Sandfellshaed shield (12,500 years BP; Saemundsson, 1995). The map area lies to the southeast of the Eldvorp crater row and to the southwest of the Sundhnukur eruptive fissures. Very few fractures are present in the Eldvorp lavas. Most of the structures in this area are opening-mode fissures with considerable horizontal opening in many places. Normal faults are present (Fig. 3.12) as well, but they are generally short, discontinous and exhibit small vertical offset. Fractures in the map area are of two types. Either they are long, straight, isolated structures or they form complex arrays with parallel, en-echelon and along-strike arrangement in close proximity.

3.6.1.3. Stora-Sandvik/Reykjanes

This area (Fig. 3.13) covers almost the entire southwestern tip of the Reykjanes Peninsula, known as Reykjanes, and the area called Stora-Sandvik, along the west coast of the peninsula. It includes the Stampar eruptive fissure and part of the Elvorp fissure system as well as the northwestern margin of the rift zone. The area was examined using air photos at a scale of 1:36,000 covering an area of 58.5 square kilometers. Fractures here cut seven different lava flows ranging in age from 12,500 to 600 years BP (Saemundsson, 1995). For purposes of this study they have been grouped into flows younger than 3000 years BP, between 3000 and 8000 years BP, and older than 8000 years BP. The nature of the fractures in this area varies considerably from one place to

the next. Fractures at Stora-Sandvik lie at the westernmost edge of the fissure swarm and cut early post-glacial pahoehoe shield lavas. Normal faults here have displacement of several meters, but true displacement is difficult or impossible to determine because of the presence of abundant windblown sand. In fact, dune structures are common in this area and frequently seem to follow the same trend as many faults, perhaps obscuring fault scarps in places. Narrow graben structures up to 40 meters wide are common in this location. Most trend in a northeasterly direction and many interact with ENE-striking normal faults resulting in very complex, zigzag structures at Stora-Sandvik (Fig. 3.14).

The Stampar eruptive fissure lies in the western part of the map area and strikes 035°. The Eldvorp crater row lies 5.6 km to the east and has a strike of 045°. Both were active during historic time, between 600 and 800 years BP (Saemundsson, 1995). Fractures near each of these eruptive fissures strike approximately parallel to the crater rows.

Two of the longer faults on this map cut lava flows of different ages. The Haleyabunga-Klufningahraun Fault and the Tjaldstaedisgja-Haugsvordurgja Fault each cut three distinct flow units. The former shows evidence of reactivation as recently as 800 years BP and the latter was reactivated at least as recently as 2000 years BP.

Also in this study area are two faults that exhibit evidence of right-lateral oblique-slip motion. These lie between Reykjanes and Molvik in Figure 3.13 and are shown in bold. In spite of the rarity of these structures, they appear to play an important role in strain accommodation on the peninsula, so it is worth describing one of them in detail. The more easterly of these two faults was mapped by traditional field methods (with tape and compass) for this study (Fig. 3.15a) The fault trends 010° and is 927 meters in length

where mapped. In general, it appears to be made up of a series of elliptical mounds or push-up structures consisting of blocks of broken lava, each trending in a NW direction, commonly separated by small gashes or normal fault segments trending NE. All normal fault segments exhibit down-to-the-east displacement. However, most normal displacement is minimal (< 1 m). The exception is at the northern end of the fault where the dominant mode of faulting is dip slip. The geometry of the push-ups and gashes is consistent with a right-lateral sense of motion (Fig.3.15 b).

The nature of the fault changes along strike so that there are three segments with different characteristics. Segment 1 is approximately 325 m in length. It begins at the edge of a younger lava flow, so may extend farther to the south, having been buried in part by that flow. At the southernmost end is a very large mound several meters high and quite elongated in the northwesterly direction. The next mound is S-shaped and narrower, but quite long compared to the other mounds on this segment. The rest of the segment consists of four small, rounded mounds separated either by a gash (opening-mode fissure) or a normal fault with small displacement. This segment ends at a diffuse area of normal faulting, about 80 m along strike. Segment 2 is approximately 235 m in length and is made up of several closely spaced mounds arranged in a row along strike. Each mound is highly elongate, some exhibiting distinct S-shape. Mounds are low and indistinct in places, and at the north end of this segment they step gradually to the left (NW). Segment 3 is 294 m in length and is made up predominantly of normal fault segments with significantly more dip-slip displacement than elsewhere on this fault. Although it was clear that maximum displacement occurred at this point on the fault, it

could not be measured accurately due to windblown sand filling the depression in the hanging wall. Location of maximum displacement is about 170 m along the segment.

Although no evidence of lateral offset could be determined along this particular fault, the pattern and trends of alternating mounds and gashes is similar to that described along historically active right-lateral strike-slip faults in the SISZ (e.g., Bjarnasson et al., 1993; see Fig. 3.15b). In several locations in the eastern part of Reykjanes Peninsula, offset has been determined to be right-lateral strike-slip on similar structures (Eyolfsson, 1998; Einarsson et al., in prep).

3.6.2. Fracture azimuth

For the Vogar area, 586 fractures were mapped from the air photos. The range of azimuths for all fractures at Vogar is from 019.6° to 089.6°, with a mean of 051.1° and a standard deviation of 11.5°. Fracture azimuths exhibit a normal distribution with the great majority between 050° and 060° (Fig. 3.16). Fractures less than 200 m in length span the entire range of azimuth, but fractures greater than 600 m in length strike between 040° and 060° (Fig. 3.17). The three longest fractures in the study strike between 055° and 060°.

At Grindavik, 291 fractures were mapped, with a range of azimuths from 005.9° to 068.8°, a mean of 037° and a standard deviation of 10°. Fracture azimuths also show a normal distribution, but with the great majority striking between 035° and 040° (Fig. 3.16). Fractures less than 100 m in length span the entire range, but those above 100 m strike between 020° and 050° (Fig. 3.17).

In the Stora-Sandvik/Reykjanes area, 320 fractures were mapped. The range of azimuths is from 358.2° to 127°, with a mean of 042° and a standard deviation of 13.2°. The peak of the histogram (Fig.3.16) falls at 040°, but the distribution of azimuths is not normal. Rather, it is skewed towards a more easterly trend, with greater than 70% of the fractures having a strike above 040°. This represents the large number of fractures in Stora-Sandvik area relative to the rest of the map. There is no apparent correlation between fracture length and azimuth (Fig. 3.17).

At Molvik, 764 fractures were mapped, with azimuths ranging from 005° to 180°; the overwhelming majority strike between 010° and 040° (Fig. 3.18a). Most fractures are under 5 m in length and these span the full 180° of azimuth (Fig. 3.18b). Azimuths for fractures greater than 4 m long (Fig. 3.18c) show a well-defined peak between 010° and 015° and another smaller peak between 025° and 030°. Thus, although fractures may form initially in any orientation, only those that are suitably oriented will lengthen. All fractures greater than 10 m in length strike between 020° and 040°.

3.6.3. Fracture density

Fracture spacing at Vogar and Grindavik was measured from the air photos along transects spaced 500 m apart and oriented perpendicular to the average trend of fractures in each area. Measurements at Grindavik were made on only a relatively small area of the air photo because young lavas from Eldvorp divide this area in the middle so that spacing across the entire photo would not reflect true fracture spacing. Average spacing measured at Grindavik is 229 m, but the standard deviation is 245 m, indicating a very irregular spacing. At Vogar, fracture spacing is somewhat variable from northeast to southwest

(Fig. 3.19). Average spacing across the entire area is 343 m and the standard deviation is 258 m, indicating a slightly more regular spacing. At Grindavik the number of fractures per unit area averaged over the entire air photo is 26.45/ km^2 in contrast to15.75/ km^2 at Vogar. However, total fracture length per unit area at Vogar is 1813 meters/km^2 whereas at Grindavik it is 1025 meters/ km^2. This is a reflection of the amount of fracture linkage that has occurred at Vogar relative to Grindavik. The longest single fracture measured at Vogar is 1358 m in length, whereas at Grindavik the longest single fracture is 548 m. Fracture spacing and density values are meaningless for the Stora-Sandvik map because this area is so spatially variable, and lava flows younger than 3000 years BP cover almost the entire central part of the map.

3.6.4. Fracture length distribution

Fault and fracture population studies at mid-ocean ridges (e.g. Carbotte and Macdonald, 1994; Cowie et al., 1993a), unlike those in continental settings (e.g., Cladouhos and Marrett, 1996), have concluded that the cumulative frequency distribution of fracture lengths is exponential. In contrast, Gudmundsson (1987) found that a power-law distribution fit his data for fractures on Reykjanes Peninsula. Cowie (1998b) suggests that this discrepency arises because power-law (fractal) distributions in mid-ocean ridge settings only apply to areas smaller than the width of the active rift zone. Experimental models conducted by Ackermann et al. (1997, 2000) have shown that a transition from a power-law to an exponential distribution may occur during the evolution of a population of fractures once the largest fractures have entirely ruptured through the

progresses, evidence of earlier linkage events becomes obscured by scarp degradation. Alternatively, longer fractures may form from longer segments because they are forming within a thicker layer. The depth to the brittle-ductile transition varies across the peninsula and could be significantly different in each sub-area of this study.

3.7. Comparison with models

Several aspects of the deformation seen on Reykjanes Peninsula are also seen in scaled experimental models of oblique deformation (See Chapters 1 and 2 for full explanation of the models). Because we know the boundary conditions of the models and can observe the evolution of their deformation, they provide a comparison with and an opportunity to explain some of the structures that are characteristic of oblique extensional environments in the real world. A fault trace map for the $\alpha = 30°$ model (Fig. 3.22) after 2.5 centimeters of displacement (22 % extension) and rotated into the same attitude as Reykjanes Peninsula, looks similar to the Reykjanes Peninsula map (Fig. 3.2). In particular, the spatial distribution of fractures and the general geometry of fractures can be compared.

3.7.1. Large-scale spacing of fissure swarms

Researchers in Iceland have long recognized that fractures and eruptive fissures in the neo-volcanic zones are arranged in clusters that they have called swarms, each associated with a central volcano containing a high temperature geothermal field and at least some rhyolitic magma. Together these make up a volcanic system (e.g. Saemundsson, 1979). On Reykjanes Peninsula, three fissure swarms have been

recognized, but none are associated with a central volcano (sensu stricto) (see Fig. 3.3). The Hengill swarm does have a central volcano and is located at the junction between Reykjanes Peninsula, the SISZ and the Western Volcanic Zone. The most obvious characteristic of the spatial distribution of fractures on Reykanes Peninsula is the very regular spacing of these swarms. The area between them is relatively free of fractures, even in the oldest lava flows. Why this should be is not agreed upon. Some prefer a model in which the wavelength of mantle upwelling controls the spacing of volcanic systems (e.g. Sigurdsson and Sparks, 1978; Ryan, 1990). Volcanic activity then generates the faults and fissures that make up the swarm. Others prefer a model whereby magma ascent into the upper crust is focused by extension due to faulting at slow spreading ridges. The process may be modulated, but not controlled, by mantle upwelling causing thermal perturbations in the crust and raising the depth of the brittle/ductile transition (e.g., Mutter and Karson, 1992).

On the $\alpha = 30°$ model used in this study (at 2.5 cm of displacement), a clustering of fractures is perceptible, though not immediately obvious. However, when we look at the model in earlier stages of its evolution, a pattern emerges (Fig. 3.23). Results of Chapter 2 indicate that a loose clustering of displacement-normal faults forms very early around the first faults to nucleate, probably due to stress enhancement in the tip zones of these small isolated fractures. At 2.0 cm of displacement, seven small clusters can be seen. These gradually grow and merge to become six and then finally four large clusters at the 2.5 cm displacement increment. These clusters form spontaneously without any pre-existing anisotropies in the modeling medium and without the presence of magma. The areas between the clusters are relatively devoid of faults. These results support a

model of tectonic focusing of magma by faulting and provide a possible explanation for the development of fissure swarms on Reykjanes Peninsula.

3.7.2 Spatial distribution of fractures

Tectonic trends on Reykjanes Peninsula and in the models are summarized in Figure 3.24. If we look in detail at the strike of fractures in the RFS (Fig. 3.2), we see that there is a significant difference in the strike of fractures in the zone of eruptive fissures (within the dashed lines) and those outside of that zone. Experimental models of oblique rifting show how this tectonic pattern can develop. The fault trace map for the model (Fig. 3.22) shows a similar spatial distribution, and a histogram of azimuth for faults along the model rift margin compares well with that of fractures from Vogar (Fig. 3.16).

On Reykjanes Peninsula normal faults and non-eruptive fissures along the margin of the zone of active volcanism strike approximately 20° oblique to the trend of the plate boundary. Mid-ocean ridge researchers have described a similar pattern along the Mohns Ridge (Dauteuil and Brun, 1996) and Reykjanes Ridge (Applegate and Shor, 1994). Searle et al. (1998) and Tuckwell et al. (1998) have suggested that these faults nucleate and grow in the axial zone of the rift, but rotate toward a more rift-parallel trend as they migrate to the rift margin. Our models indicate that such rotation is not necessary to form these rift-subparallel faults.

Jeffris and Voight (1980) found a similar pattern in two sets of fractures in Tertiary and Plio-Pleistocene rocks that have long since migrated out of the neo-volcanic zone north of Reykjavik. They used the mineralogy of vein-filling material to determine that the different fracture sets formed at the same time, during active rifting, and

concluded that there is a change in stress between the "flank zone" and the "active zone". They attribute the change to thermal contraction and bending of the crust. Tuckwell et al. (1998) propose a model whereby this stress is generated by gravitational forces due to a density increase of the crust as it cools. Both models involve a change in stress state induced by a change in crustal properties at the structural boundary between weak crust in the axial zone and stronger crust on the margins.

The results of our modeling experiments support this conclusion. Along the margins of the deformed zone in the model, in the area outboard of the latex sheet, normal faults form approximately 20° oblique to the trend of the deformed zone. A closer look at the model surface (Fig.3.25) shows that a flexure forms at the boundary between the latex sheet and the rigid metal plate. As extension proceeds, a topographic gradient develops between the thinned clay over the highly stretched latex substrate under the rift zone and the thicker clay over the rigid subtrate at the rift margin. As a consequence, the stress state in the clay over the rigid metal plate differs from that over the stretched latex sheet. Normal faults develop along the flexure in response to this change in stress, and because of the oblique geometry of the models, they form oblique to both the rift trend and the normal to E_{hmax}. These faults form relatively late in the model evolution and continue to nucleate and lengthen after fault growth has ceased within the rift zone (see Chapter 2). Additional work is required to determine exactly what the stress state is in the zone of flexure.

A small but significant number of strike-slip faults have been mapped on Reykjanes Peninsula (Sigurdsson, 1985), and at least two of them are present on the Stora-Sandvik/Reykjanes air photo (see section 3.6.1). These occur in the center of the rift zone

and strike sub-parallel to the spreading-normal direction, between 010° and 015°. Farther east on the Peninsula, Einarsson et al. (in prep) have been mapping many of these north-northeast trending, right-lateral strike-slip faults and have interpreted them to be a continuation of the South Iceland Seismic Zone. On Reykjanes Peninsula, these faults appear to be restricted to the zone of active volcanism in the center of the rift, and some are seen intersecting or terminating at volcanic vents (Eyjolfsson, 1998). The westernmost strike-slip fault on the Stora-Sandvik/Reykjanes air photo terminates at the vent called Melur. The fault mapped for this study (Fig. 3.15a) and discussed in section 3.6.1 exhibits a significant component of dip-slip and should in fact be considered an oblique-slip fault with a right-lateral component of motion.

The term "bookshelf" faulting has been used to denote shear deformation accommodated by an array of faults trending perpendicular to the shear direction (Sigmundsson et al., 1995). This style of deformation has been proposed to explain north-trending right-lateral strike-slip faults that have been mapped in the South Iceland Seismic Zone (e.g. Einarsson and Eiriksson, 1982; Bjarnasson et al., 1993). These faults are responsible for large (M>7) historic earthquakes that have occurred every 45 to 112 years since the time of Icelandic settlement 1000 years ago. The SISZ is an east-west trending transform zone that connects the Reykjanes Peninsula and the Eastern Volcanic Zone in South Iceland. GPS measurements confirm that left-lateral strain is accumulating along this zone (Sigmundsson et al., 1995), but no through-going transform fault has ever been mapped here. Hackman et al. (1990) used a boundary element model to confirm that north-trending faults can accommodate this left-lateral strain if they are 10 to 15 km long. Similar faults that have been mapped on Reykjanes Peninsula are much shorter than 10

km, but this difference can be accounted for by the decrease in depth to the brittle-ductile transition when going west from the SISZ into the rift zone.

Bookshelf faulting also occurs in our models. The most prominent structures in the center of the model rift zone are right-lateral oblique-slip faults that strike parallel to the spreading-normal direction. These faults are the longest structures on the model, but do not extend beyond the boundaries of the latex sheet. They are also the most abundant structures on the model early in its development. Also present in the rift center in the models, but absent on the map of Reykjanes Peninsula, are left oblique-slip faults striking sub-parallel to the rift trend. These are shorter and less numerous than the right oblique-slip faults until after 3.0 cm of extension (see Chapter 2). As extension continues, these faults become longer and more abundant and accommodate an increasingly greater proportion of strain in the center of the rift zone (see Figs. 2.6 and 2.8). Einarsson and Eiriksson (1982) suggested that the lack of east-west trending left-lateral faults in the South Iceland Seismic Zone is due to the transient nature of the zone as it migrates southward in response to ridge propagation. The same explanation may not apply to the Reykjanes Peninsula as it has been an active spreading center for 6 to 7 million years, but it is not clear how much time would be needed for left-lateral faults to develop in this rift zone.

In the center of the rift zone on Reykjanes the predominant strike of eruptive fissures, non-eruptive fissures and normal faults is perpendicular to γ, the direction of maximum horizontal extension (E_{hmax}) (Fig.3.16). Notice that E_{hmax} is not parallel to the spreading direction (Fig.3.24). Withjack and Jamison (1986) determined that oblique rifting combines both extension and shear, the relative contributions of which are controlled by

the acute angle, α, between the rift trend and the direction of displacement of the rift walls. As α decreases from 90°, γ rotates towards the rift trend according to the equation:

$$\gamma = 90° - 1/2 \tan^{-1}(\cot \alpha) \qquad (4)$$

This analytical model predicts that E_{hmax} will be 60° clockwise from the rift trend when $\alpha = 30°$. For Reykjanes, the average trend of eruptive fissures suggests that the direction of E_{hmax} is 55° clockwise from rift trend.

There are very few structures in the center of the model rift that strike perpendicular to E_{hmax} at this point in its evolution. However, with continued extension, high-displacement normal faults do form along this trend (Fig. 3.26). As short left oblique-slip faults link up, some of them rotate until they are perpendicular to E_{hmax}. Once in this orientation, they gain displacement quickly and become very large normal faults. Tuckwell et al. (1998) have proposed a similar mechanism of linkage for the origin of eruptive fissures along the Reykjanes Ridge. Because magma is not present in the clay models, these structures become normal faults and not eruptive fissures. With the stress perturbation caused by the presence of magma, it is easy to see how these large structures could become sites of eruption.

3.8. Discussion

There are, of course, several important differences between the experimental models and Reykjanes Peninsula (Table 1). Most are attributable to the presence of magma in the latter and its absence in the former. One significant difference that may not

relate to the presence of magma is the absence of left lateral oblique- or strike-slip faults on Reykjanes Peninsula. In the experimental models, these faults do not become numerous until right lateral oblique-slip faults have reached their maximum length. The only place where east-west striking faults were seen during this study is Stora-Sandvik. There is no question that faults with this strike form a distinct sub-population in that location, but there is no evidence of any lateral offset along them. It is possible that small east-west striking oblique-slip faults are present on Reykjanes Peninsula but their presence has not been noticed, either because their surface expression is too subtle or because they have been covered by young flows.

A comparison of the pattern of fractures in Vogar with those in Grindavik (Figs. 3.8 and 3.11 respectively) shows that there are obvious differences, not only in the predominant strike direction but also in the degree of development of fractures. Fractures in Vogar tend to be long, complex, anastomosing structures made up of many hard- and soft-linked segments with a wide range of azimuth. The average length of fracture segments is also greater at Vogar than at Grindavik, and most of the normal faults there have high displacement. Fractures in Grindavik, on the other hand, are shorter, straighter and more discontinuous. Few normal faults are present, but those that are have low displacement (e.g. Fig. 3.12). The longest structures in the area are relatively wide arrays of parallel and en echelon opening mode fissures.

Total fracture length per unit area is 40 percent greater in Vogar than in Grindavik, even though fractures in both areas are cutting similar age, early post-glacial shield lavas. A map of the Stora-Sandvik/ Reykjanes area (Fig. 3.13) shows the absence of large numbers of faults and fractures in the youngest lavas. This has often been attributed to the

fact that old faults are being covered by fresh lava flows (Wright, 1998; Rubin, 1990). This is undoubtedly true to some extent, as young flows drape old faults in several locations, and, in a few cases, old faults propagate through the youngest flows (Fig. 3.27). However, low fracture density in the oldest (early post-glacial) lavas at Grindavik compared with high fracture density in similar age lavas at Vogar implies that fractures are not evenly distributed within the rift zone either in space or time, thus making it difficult to determine whether or not faults are being covered in the center of the rift zone. In spite of being in the zone of active volcanism for more than 10,000 years, there are relatively few fractures at Grindavik, even in the youngest lavas. They are in the zone of active volcanism where the brittle crust is weak and thin. The strike of most fractures here parallels that of eruptive fissures, suggesting that their origin is related to volcanic activity. Fracture development in the Grindavik area is probably related to dike injection events during activity at the Sundhnukur eruptive fissure which lies along strike just a few kilometers to the northeast. If another eruption occurs in this location it is possible that growth of fractures at Grindavik would be a consequence. However, it is just as likely that this area will either be covered with fresh lava flows or rafted unchanged out of the zone of active volcanism.

The presence of magma at shallow crustal levels in Iceland perturbs the magnitude of the stress field and allows dikes to form episodically, perpendicular to the direction of E_{hmax}. Studies conducted during the Krafla eruptions in northern Iceland during the 1970's and 1980's (e.g., Einarsson and Brandsdottir, 1980; Rubin, 1990) showed the direct relationship between dike injection and faulting. Based on their

morphology and spatial distribution, many of the structures mapped during this study are believed to be a result of similar but smaller scale dike injection events.

At Molvik, it is possible to determine a sequence of events that shows this relationship of faulting to volcanism in the center of the neo-volcanic zone. Detailed mapping by Whitlock (1999) indicates that most, and perhaps all, of the faulting in this graben occurred during a sequence of at least three eruptions from a single vent close to the Eldvorp eruptive fissure. Displacement along a given fault in the graben is no more than 1.5 m, and individual fault segments are on the order of 100 m long. Graben width is approximately 25 m.

Graben structures at Stora-Sandvik have similar dimensions, although some are as wide as 40 m and are several meters deep. Such narrow graben structures have been mapped along the Juan deFuca Ridge (Chadwick and Embley, 1998). Pollard et al. (1983) have shown that graben width is a function of the depth of the dike tip at the time faulting occurs. Chadwick and Embley (1998) suggest that narrow grabens result when the ambient tectonic stress field is not so close to failure. During the 1974 to 1984 events at Krafla, 250 years worth of tensional strain had accumulated since the last volcanic event and the crust was near to failure when dike injection occurred. Consequently, graben faults could form while the dike tip was still at depth, as only a small stress perturbation was necessary to allow faulting. Some grabens formed during diking events at Krafla were greater than 1 km wide (Rubin, 1992). After many diking events, compressive stress may increase around the dike faster than it can be accommodated by extension due to plate motion (Rubin, 1990). Chadwick and Embley (1998) propose that narrow grabens along the Juan deFuca Ridge are a result of the compressive stress that builds up there

due to frequent diking events. This is a plausible explanation for the narrow grabens at Stora-Sandvik because they are numerous in this particular location and may be a result of a series of diking events that were closely spaced in time.

An alternative, or perhaps additional, explanation is afforded by the oblique orientation of the rift zone on Reykjanes Peninsula. If graben width is truly a reflection of the ambient state of stress before dike injection, then it implies that extensional faulting is difficult on Reykjanes. In a rift zone oriented 30° oblique to the spreading direction, the secondary horizontal strain is contractional and deformation is dominated by oblique-slip and strike-slip faulting (Withjack and Jamison, 1986). The temporal evolution of the α = 30° models in this study show that it is harder for faults to nucleate and grow in this strain state (see Chapter 2) and that most faults in the center of the model rift are oblique-slip faults. If it is harder for normal faults to form, it is likely that it is also harder for magma to rise. The same explanation may be invoked to account for the lack of true central volcanoes on Reykjanes Peninsula.

Nakamura (1970) proposed that, as an oblique rift zone, Reykjanes Peninsula experienced equal amounts of extension and shear. In fact, this is not far from what geodetic data indicates. On Reykjanes Peninsula, GPS measurements during the period from 1993 to 1998 indicate that left-lateral shear is presently accumulating at a rate of – 0.2 μstrain/yr (Hreinsdottir, 1999). This accounts for 1.3 cm/year of plate velocity in the average direction of 095°, which is a major component of the 1.85 cm/year spreading velocity and 103° spreading direction determined by the NUVEL-1A model for this plate boundary. Hreinsdottir (1999) concludes that episodic activity in the volcanic systems can account for the "missing" plate motion and that, on a long time scale, the average

plate motion would equal that determined by the NUVEL-1A model. When magma is not present in the system, left-lateral shear is accommodated primarily by right-lateral strike-slip or oblique-slip faults. When magma is present extension occurs along eruptive fissures and normal faults in the fissure swarms. The results of this study support her conclusions. The models also show that fault growth along the rift margins occurs throughout rifting. This suggests that faults in areas like Vogar and Stora-Sandvik may be active even when there is no magma present.

3.9. Summary and Conclusions

Analysis of air photos and field data have been used to characterize the fracture population of the Reykjanes Fissure Swarm and the spatial distribution of fractures on Reykjanes Peninsula. Comparison with scaled clay models of oblique deformation is useful in interpreting the data. Data are summarized as follows:

1) Eruptive fissures form perpendicular to the direction of maximum horizontal extension (E_{hmax}) and occur in the axial zone of the rift.

2) Fractures in the zone of active volcanism are few, and most trend sub-parallel to the strike of nearby eruptive fissures. Fractures here consist primarily of short segments in parallel or en echelon arrays.

3) Right lateral strike-slip or oblique-slip faults are confined to a narrow zone in the center of the rift.

4) Fracture density is highest at the rift margins. Fractures here curve towards a rift sub-parallel trend and have an average strike that is 20° oblique to the rift trend. Normal faults are more common here and tend to form long, complex structures with a wide range of azimuth and high displacement.

Differences in the fracture pattern between the model and Reykjanes Peninsula are attributable to the presence of magma in the latter and its absence in the former. The presence of magma in the axial zone of the rift allows dikes to form episodically, perpendicular to the direction of maximum horizontal extension. Narrow grabens and faults form sub-parallel to the dikes. However, the highly oblique orientation of this ridge segment makes it difficult for dikes to reach the surface and probably inhibits the development of central volcanoes on Reykjanes Peninsula.

The clay models confirm that right-lateral oblique or strike-slip faults accommodate significant strain in a stress system dominated by left lateral shear when deformation is distributed across an oblique rift zone. Although only two right lateral oblique-slip faults have been mapped in the Reykjanes fissure swarm, evidence from farther east on the Peninsula indicates that they are more common than previously thought (Einarsson et al., in prep.). Because the surface expression of these faults is so subtle, it is expected that more of them exist but have not yet been recognized in the field. It is likely that these faults play an important role in accommodating left-lateral strain on Reykjanes Peninsula. Left-lateral oblique slip faults form in the model but are absent on Reykjanes Peninsula. It is possible that the presence small east-west striking oblique-slip faults has not been noticed, either because their surface expression is too subtle or because they have been covered by young flows.

Experimental clay models predict a significant change in fault strike at the margins of oblique ridge segments, as stresses related to plate motion are modulated and reoriented by a secondary stress field related to changes in topography and crustal rheology. A change in fault strike in the northern part of the Reykjanes Fissure Swarm

marks the boundary between a thin brittle layer over a hot, weak lower crust and a thicker brittle layer over a cooler, stronger lower crust. Eruptive fissures, non-eruptive fissures and normal faults form perpendicular to E_{hmax} where crust is hottest and weakest (e.g., near Grindavik), whereas large normal faults and non-eruptive fissures form at the rift margin where the crust is stronger and colder (e.g., Vogar).

	Models	Reykjanes Peninsula
Right – lateral faults	Long oblique-slip structures cross the rift center	Small number of strike-slip structures confined to a narrow zone in the rift center
Left-lateral faults	Comparatively short oblique-slip structures in the rift center	None mapped, but focal mechanisms have been determined for a few faults
Rift parallel structures	Left-lateral oblique slip faults (see above)	Few mapped
Structures perpendicular to E_{hmax}	Rare, high-displacement normal faults form late in model evolution	Eruptive fissures, non-eruptive fissures and normal faults within the active volcanic zone
Structures 20° oblique to the rift trend	Form outboard of the latex sheet.	Form outside of the zone of active volcanism

Table 1

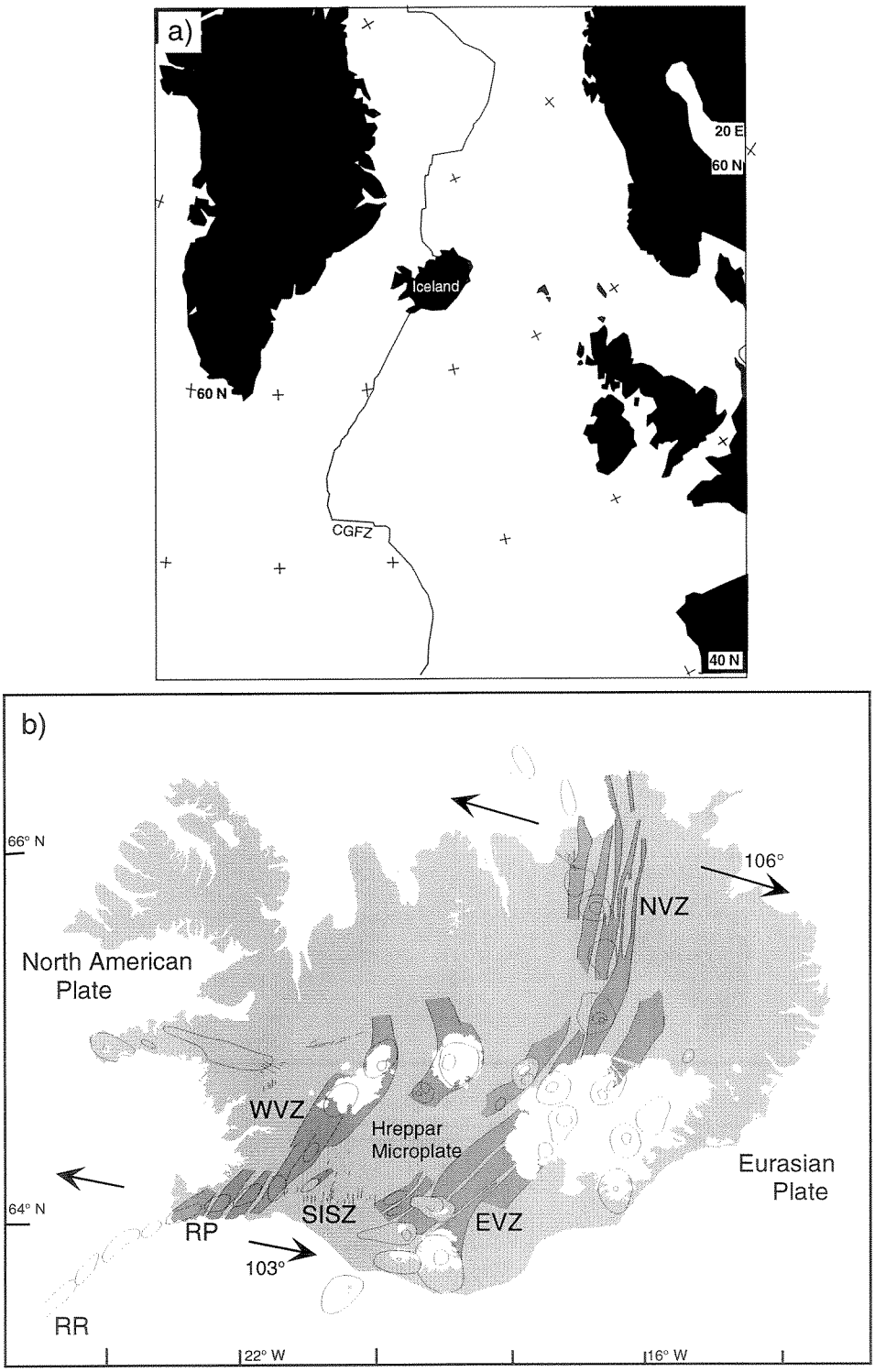


Fig. 3.1 - a) Map showing the location of Iceland along the Mid-Atlantic Ridge. CGFZ is Charlie Gibbs Fracture Zone. b) Map showing the geometry of ridge segments on Iceland. RR = Reykjanes Ridge; RP = Reykjanes Peninsula; WVZ = Western volcanic zone; EVZ = Eastern volcanic Zone; NVZ = Northern volcanic zone; arrows show the direction of plate motion according to NUVEL-1A; areas shown in white are covered by glaciers. (modified from Einarsson and Saemundsson, 1987)

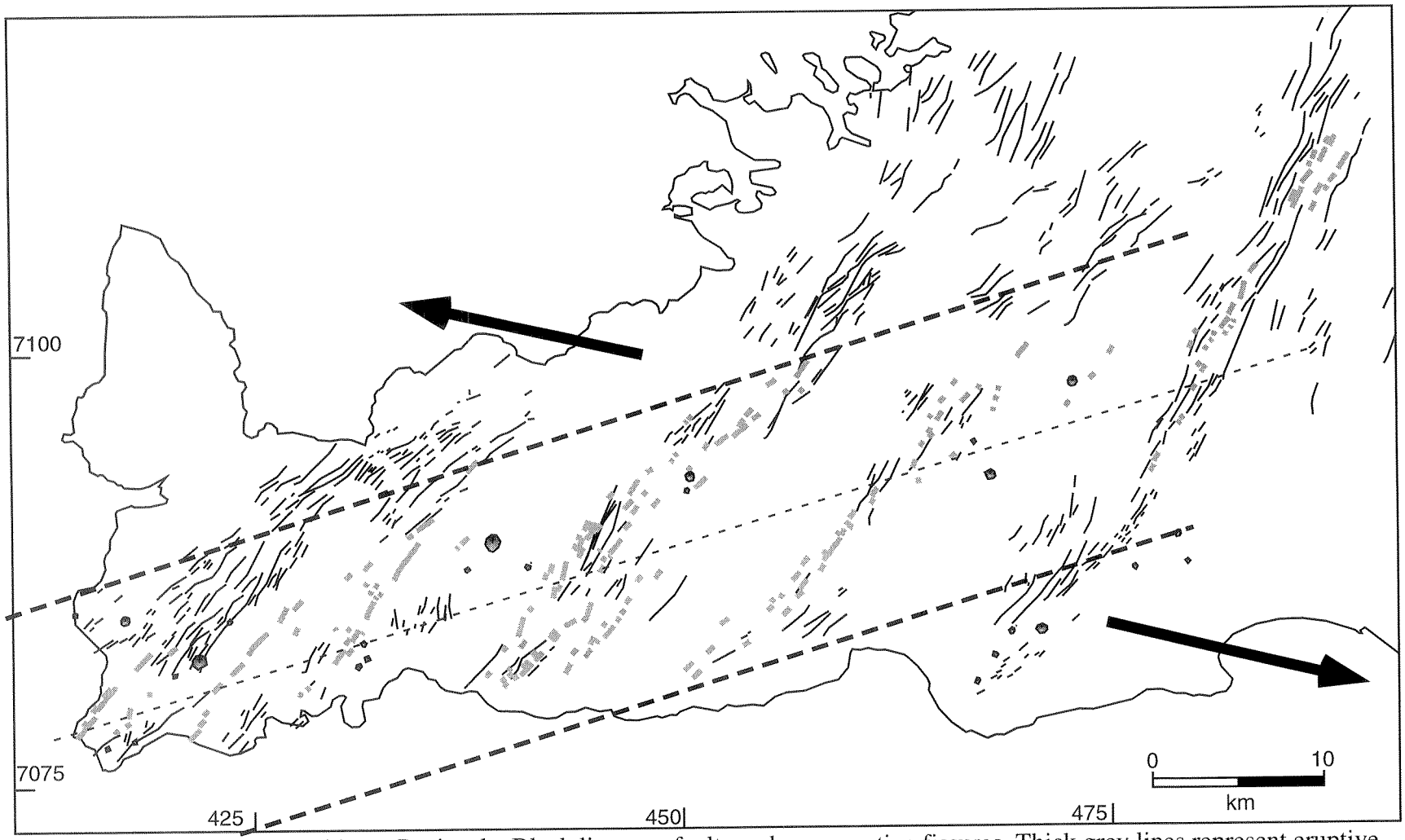


Fig. 3.2. Tectonic map of Reykjanes Peninsula. Black lines are faults and non-eruptive fissures. Thick grey lines represent eruptive fissures and vents. Textured circles represent shield volcanoes. Thick dashed lines mark the zone of active volcanism. Thin dashed line represents the axis of the ridge segment. Arrows show the direction of plate motion. Grid in UTM, Lambert Projection. Data from Saemundsson and Einarsson (1980).

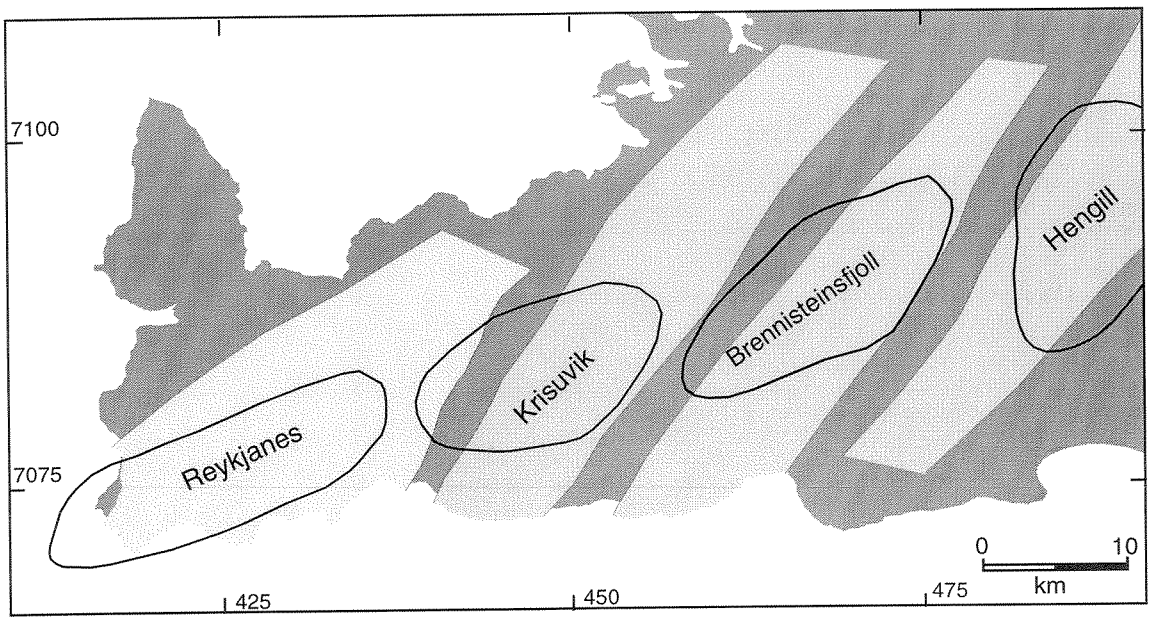


Fig. 3.3 - Volcanic systems of Reykjanes Peninsula. Areas shown in light grey outline the volcanic systems including fissure swarms. Circles outline the area of maximum volcanic production for each volcanic system. Redrawn from Einarsson and Saemundsson, 1987.

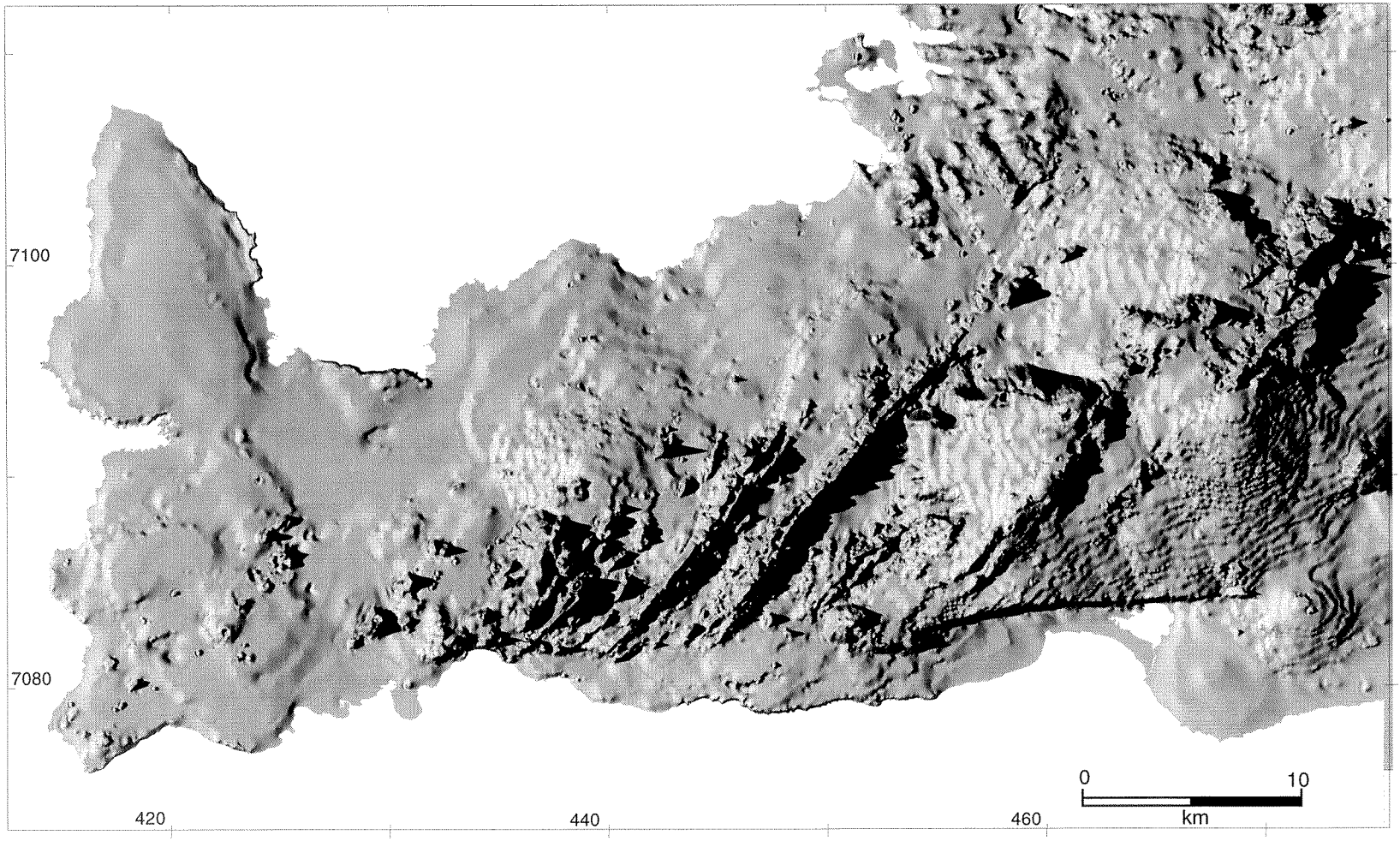


Fig. 3.4 - Shaded Digital Elevation Model of Reykjanes Peninsula. DEM resolution is 20 meters. Grid in UTM, Lambert Projection. Used with permission from Nordic Volcanological Institute.

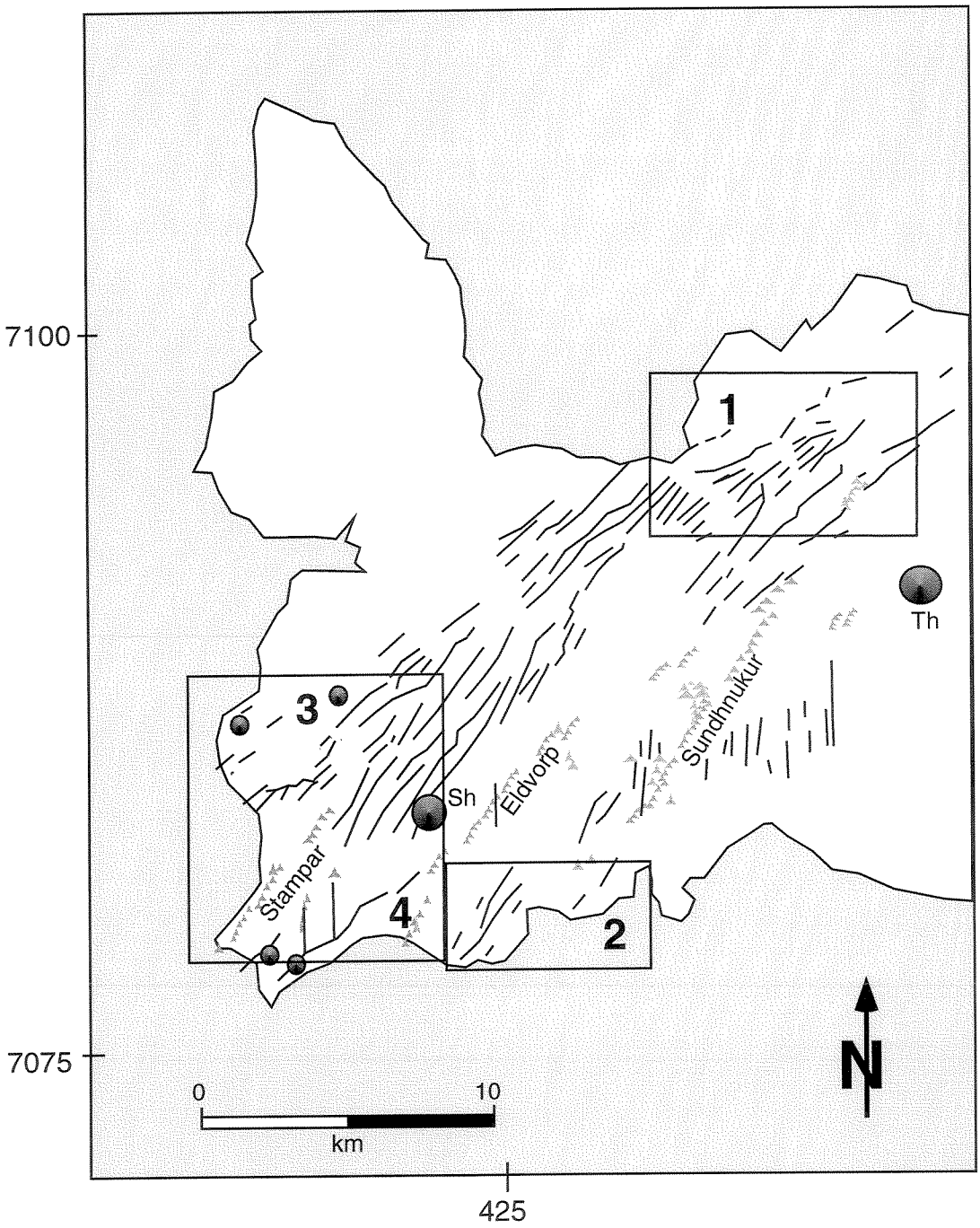


Fig. 3.5 - Map of Reykjanes Fissure Swarm, showing field locations from this study. Boxes surround the approximate areas included on the air photos. 1 is Vogar, 2 is Grindik, The box surrounding 3 and 4 is the area shown on the Stora-Sandvik/Reykjanes air photo. 3 is Stora-Sandvik and 4 is Molvik. Th is the Thrainsskjoldur shield volcano. Sh is the Sandfellsheid shield volcano.

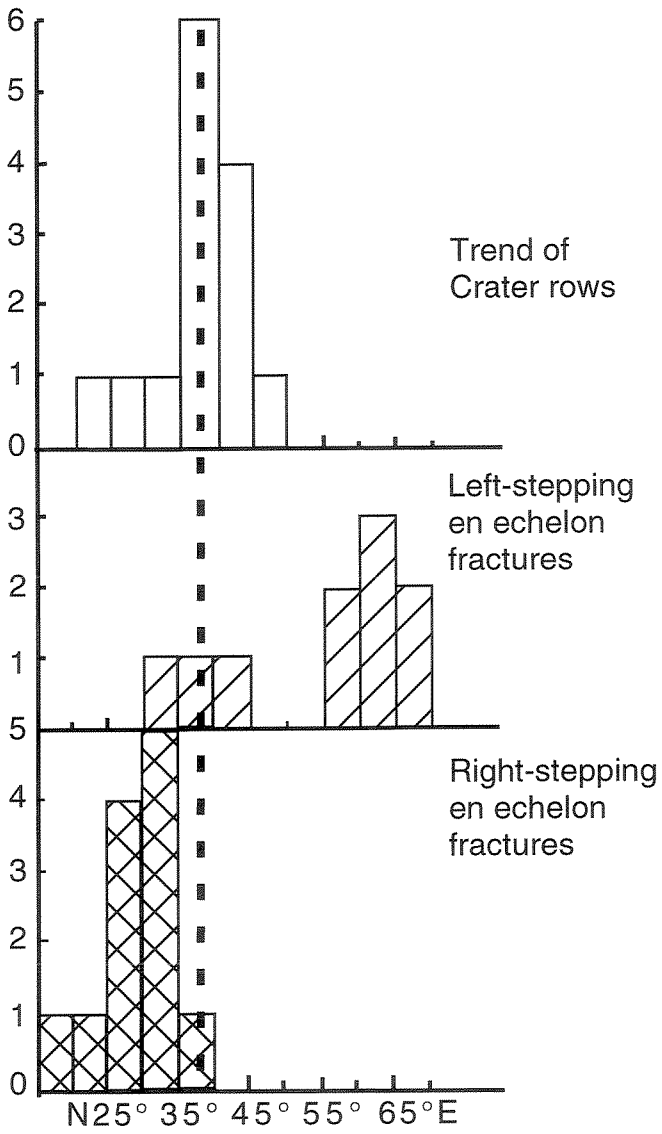


Fig. 3.6 - Histograms of azimuth for structures in the Reykjanes Fissure Swarm, from Nakamura (1970).

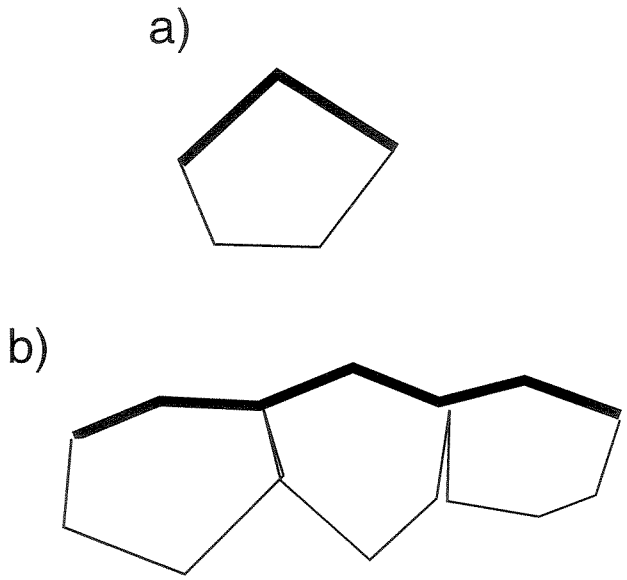


Fig. 3.7 - Criterion used during field mapping at Molvik to distinguish an ordinary cooling joint (a) from a tectonic fracture (b). See text for further discussion.

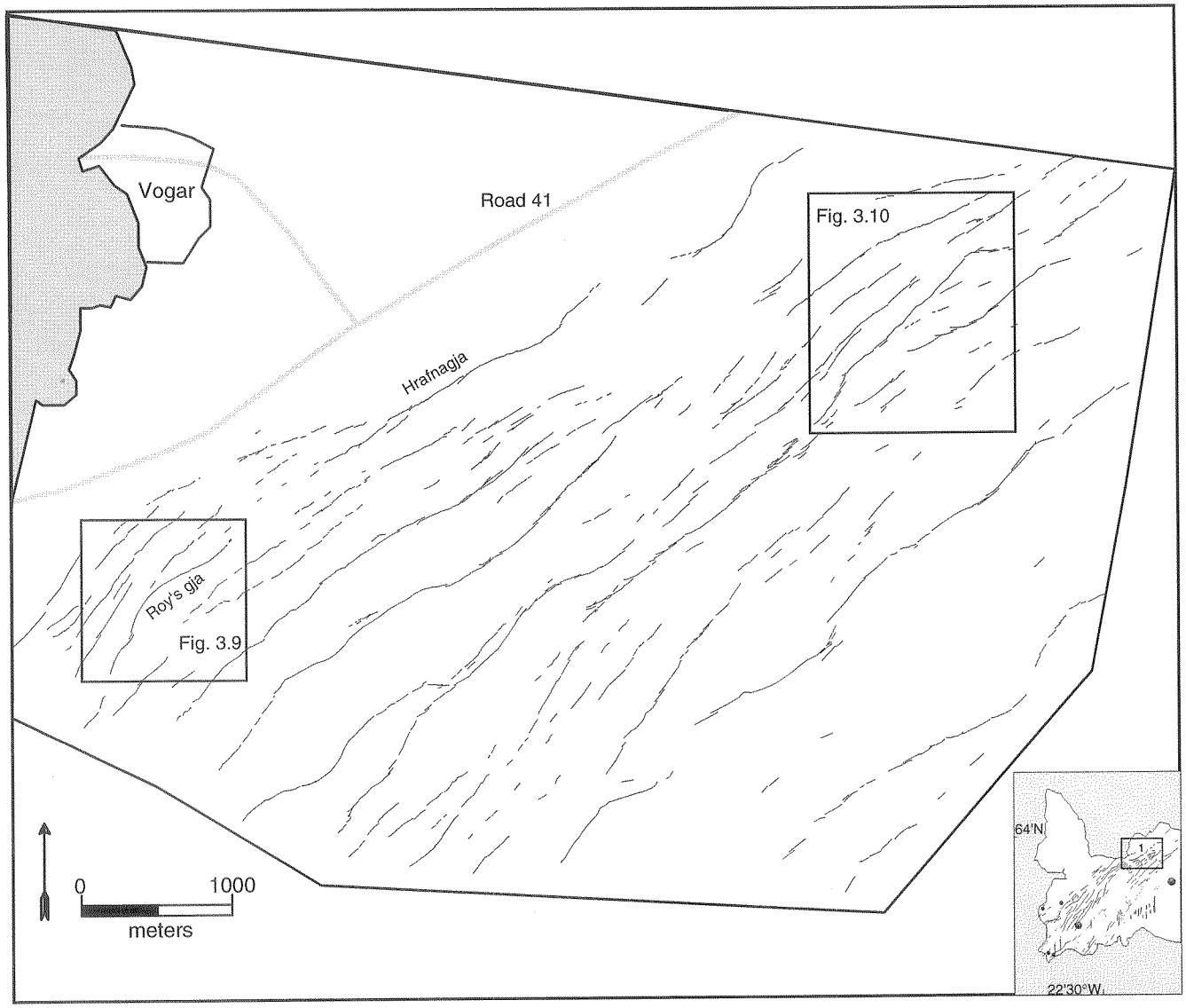


Fig. 3.8 - Fracture trace map for the Vogar photomosaic. Boxes mark areas shown in Figs. 3.9 and 3.10.

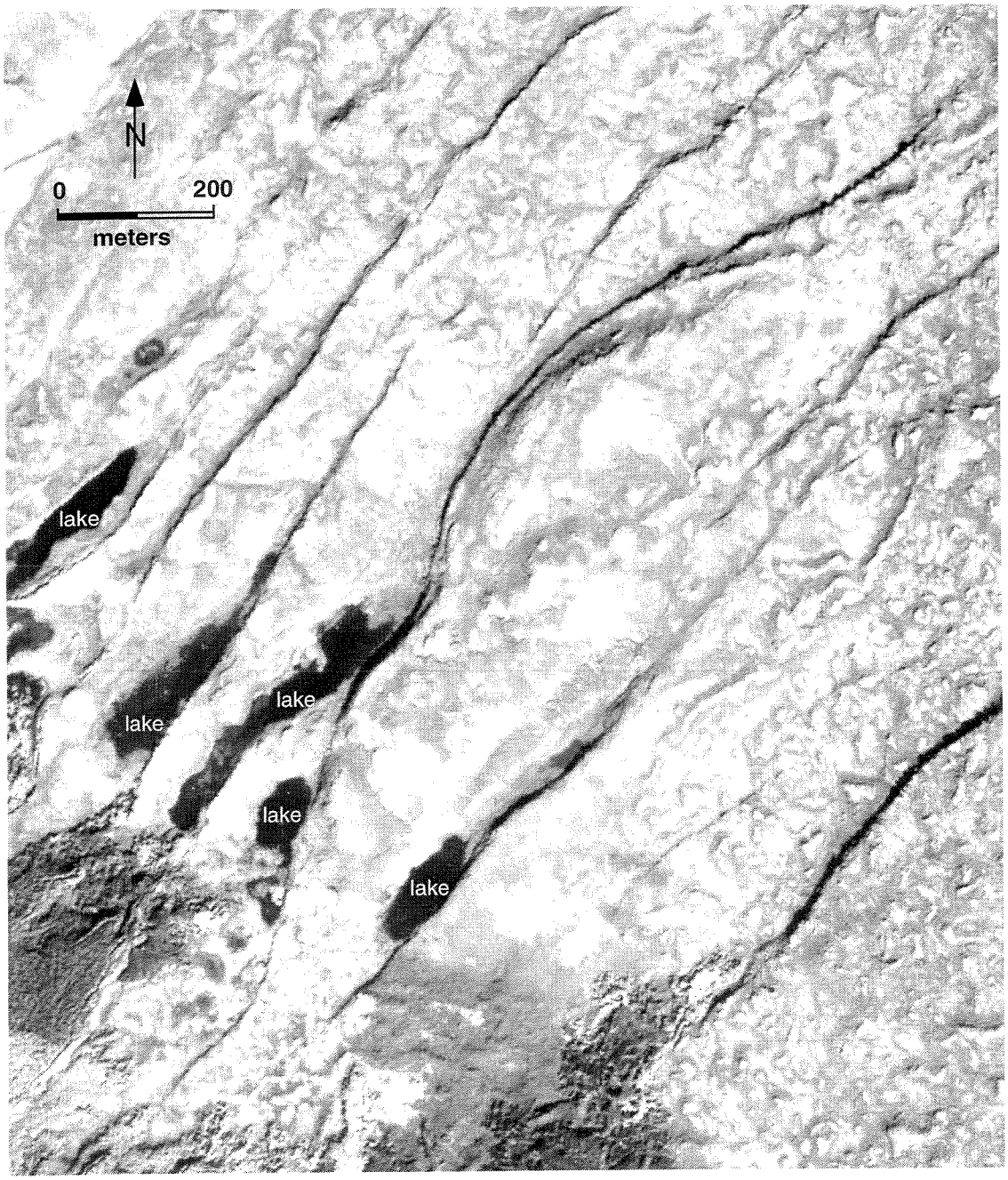


Fig. 3.9 - Air photo sub-image of normal fault in the southwestern part of the Vogar photomosaic. Note the highly curvilinear fault trace. See text for further discussion.



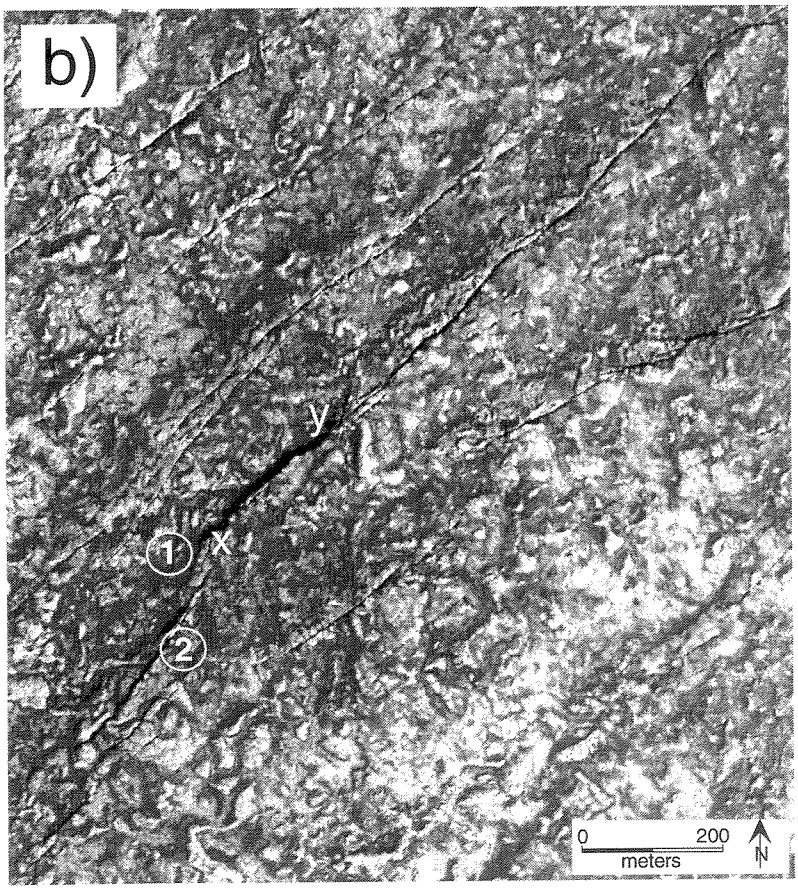


Fig. 3.10 - a) Field photo and b) air photo sub-image of fracture in the northeastern part of the Vogar photomosaic. Note the highly segmented character of this fracture and >10 degree strike difference between two overlapping segments shown in the field photo. Segments 1 and 2 marked in both images. Field photo taken from location marked x on air photo. Note the abrupt change in displacement at location marked y (width of shadow is proportional to displacement).

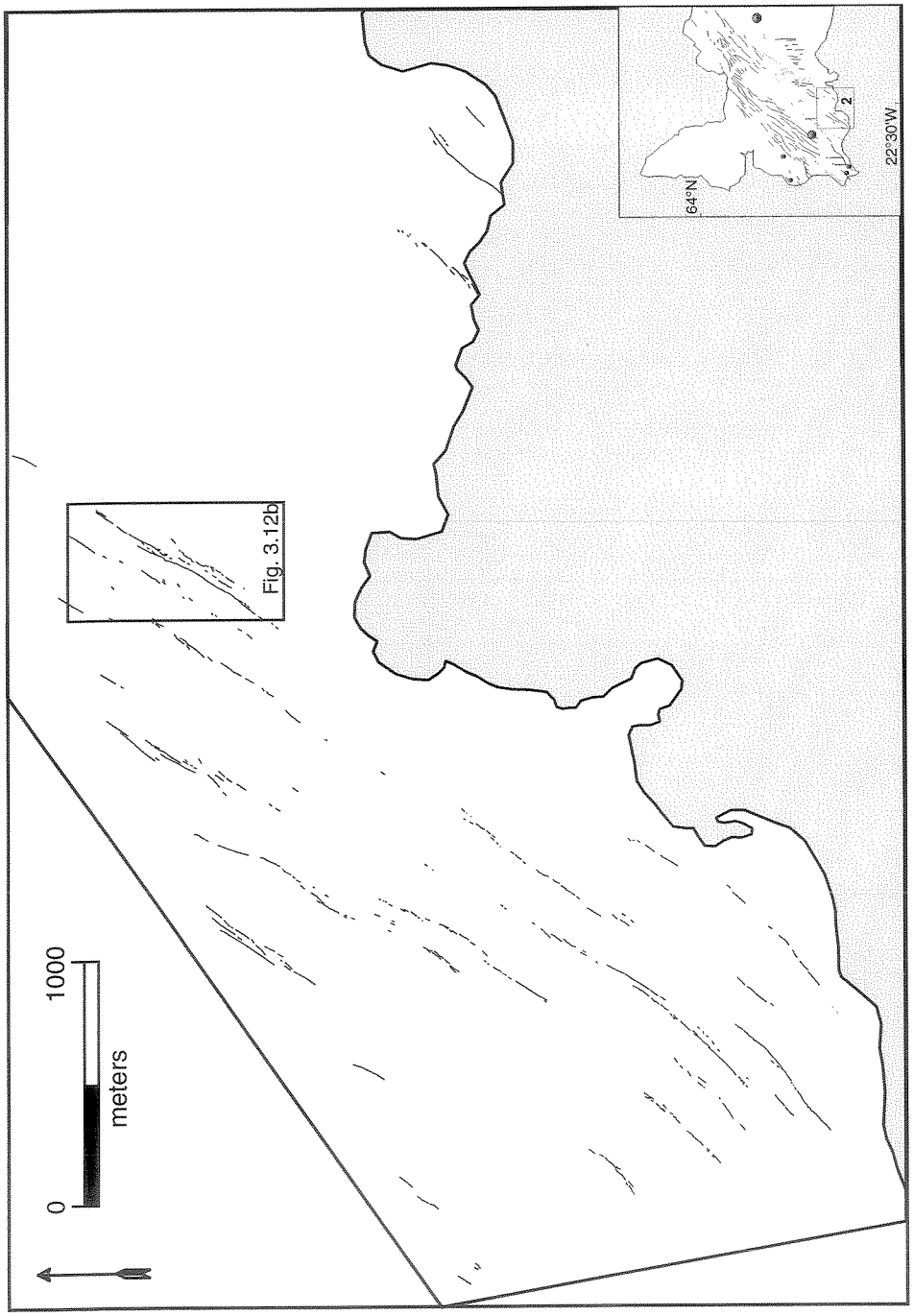


Fig. 3.11 - Fracture trace map for the Grindavik photomosaic. Box shows location of image in Fig. 3.12b.

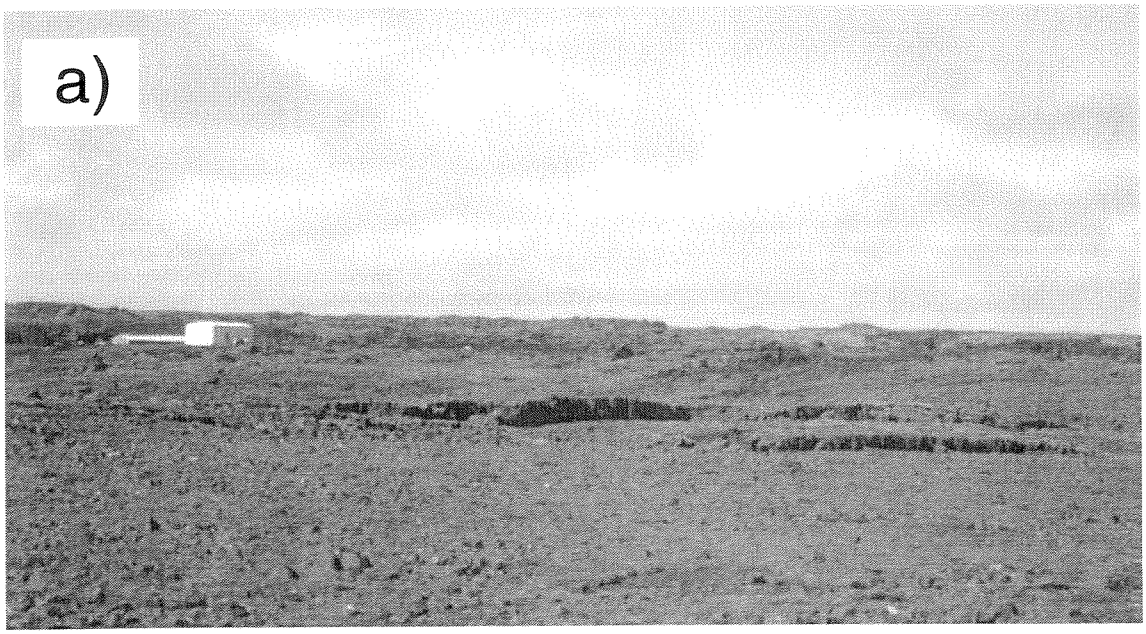




Fig. 3.12 - a) Field photo of a typical normal fault in the area covered by the Grindavik photomosaic.
b) Air photo sub-image from the Grindavik photomosiac showing a typical array of fissures.

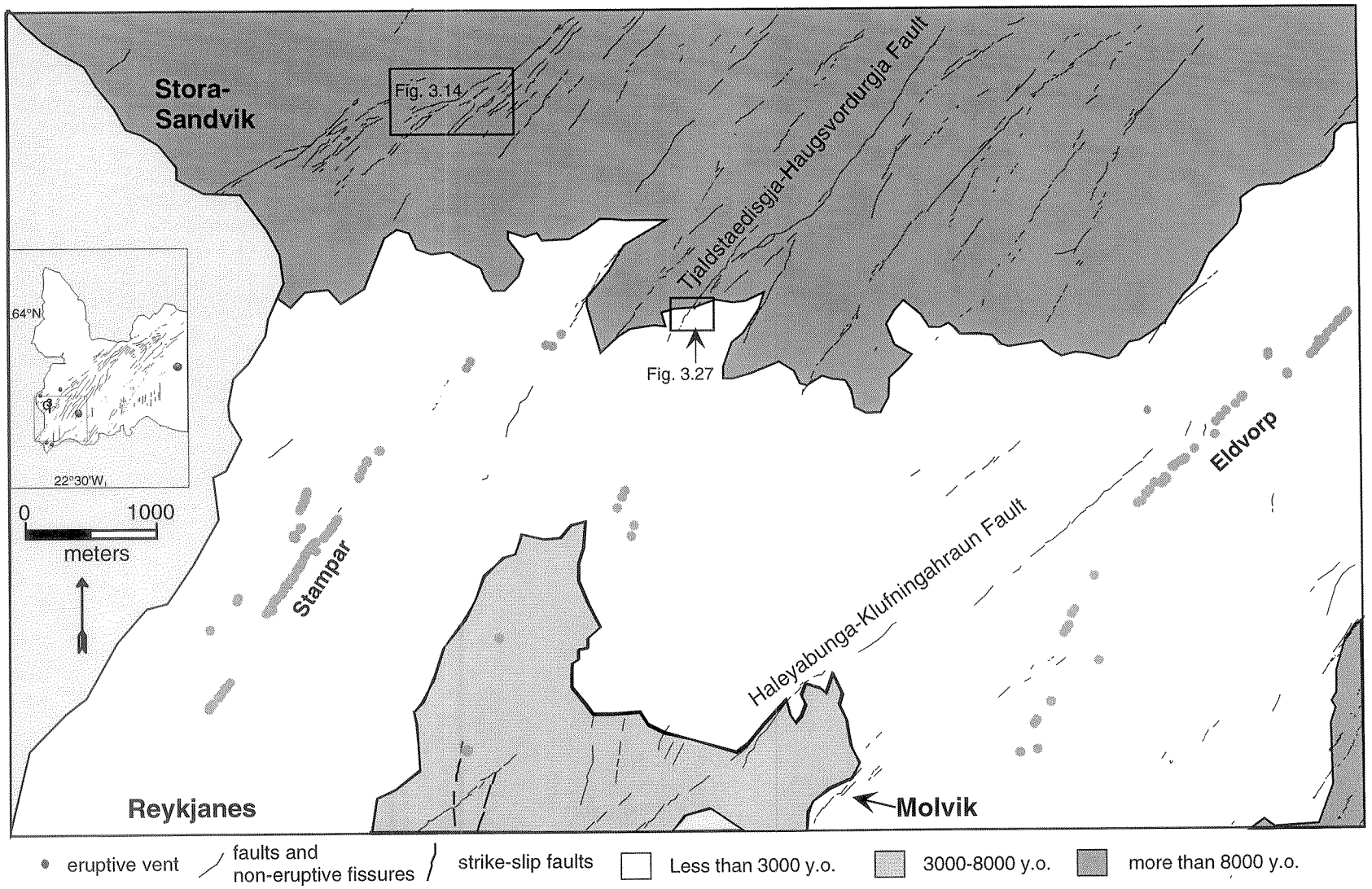


Fig. 3.13 - Fracture trace map for the Stora-Sandvik/Reykjanes photomosaic. Boxes mark locations shown in Figures 3.14 and 3.27.

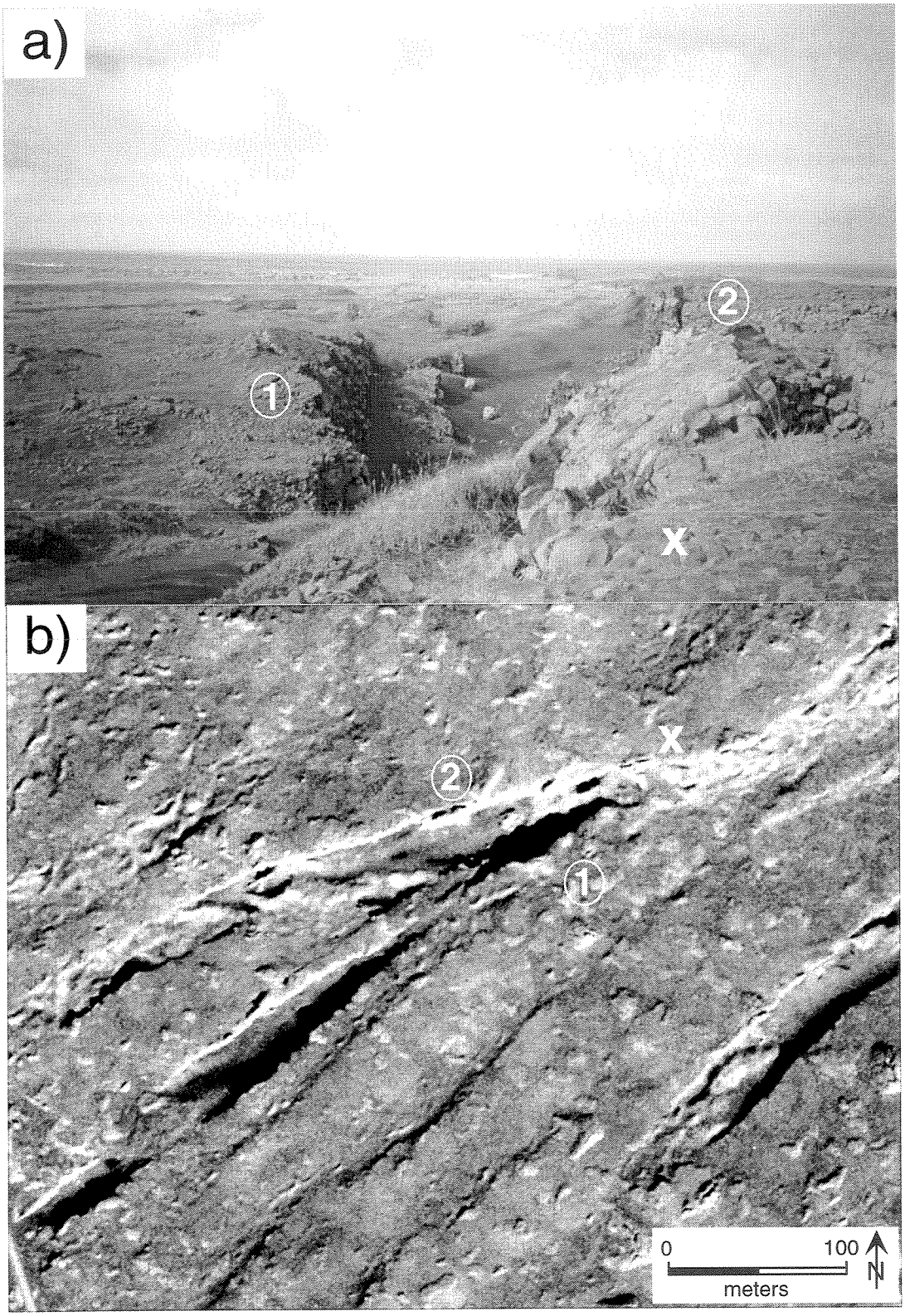


Fig. 3.14 - a) Field photo and b) air photo sub-image of complex interaction between normal fault striking 080° and graben structure striking 040° at Stora-Sandvik. Field shot taken from location marked x on the air photo. Note other narrow graben structures on the air photo. See text for discussion.

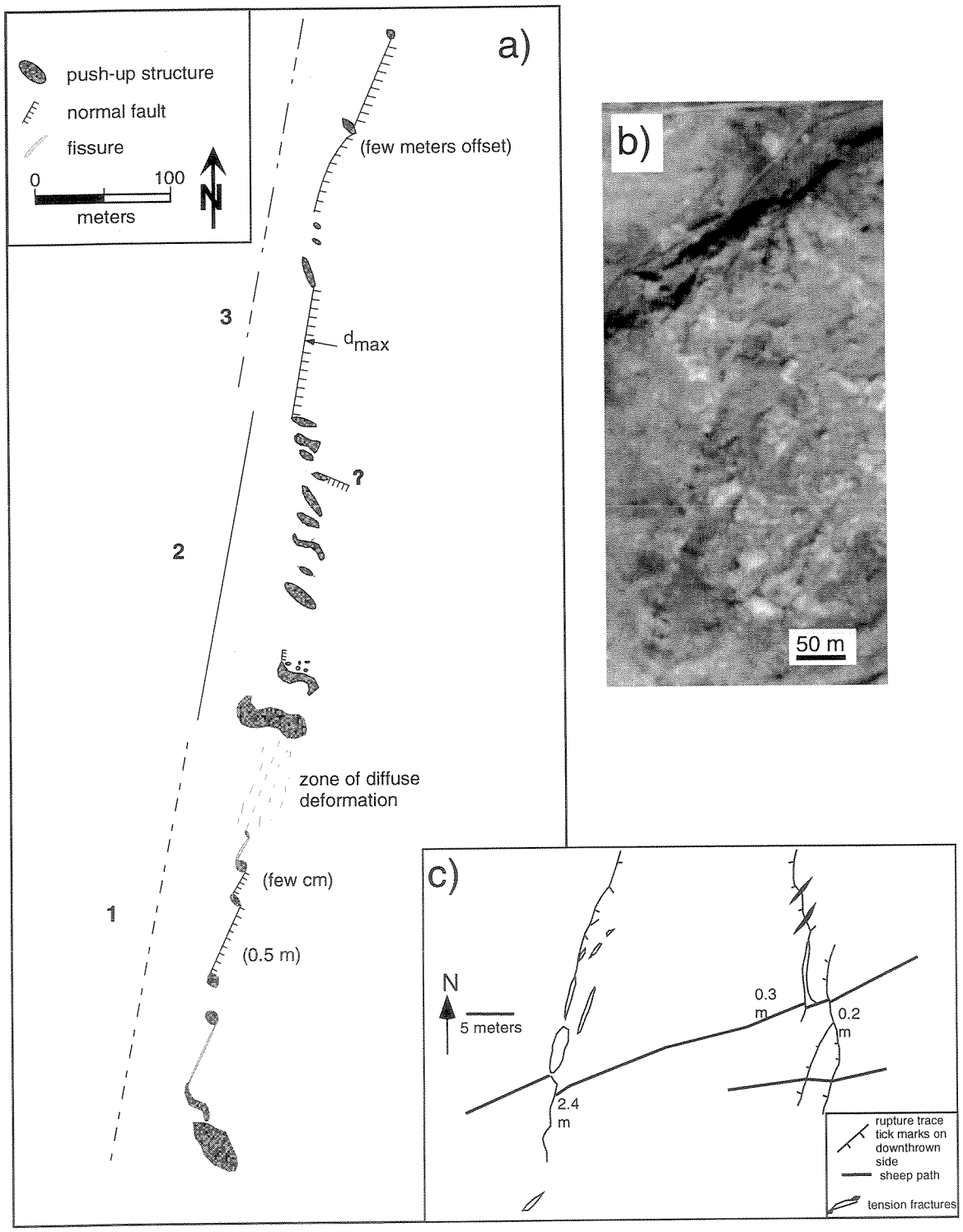


Fig. 3.15 - a) Map of right lateral oblique-slip fault at Reykjanes. b) Sub-image from Stora-Sandvik/Reykjanes air photo showing segments 2 and 3 from map. c) Map of strike-slip fault in SISZ showing right-lateral offset of 2.4 m (redrawn from Bjarnason et al., 1993).

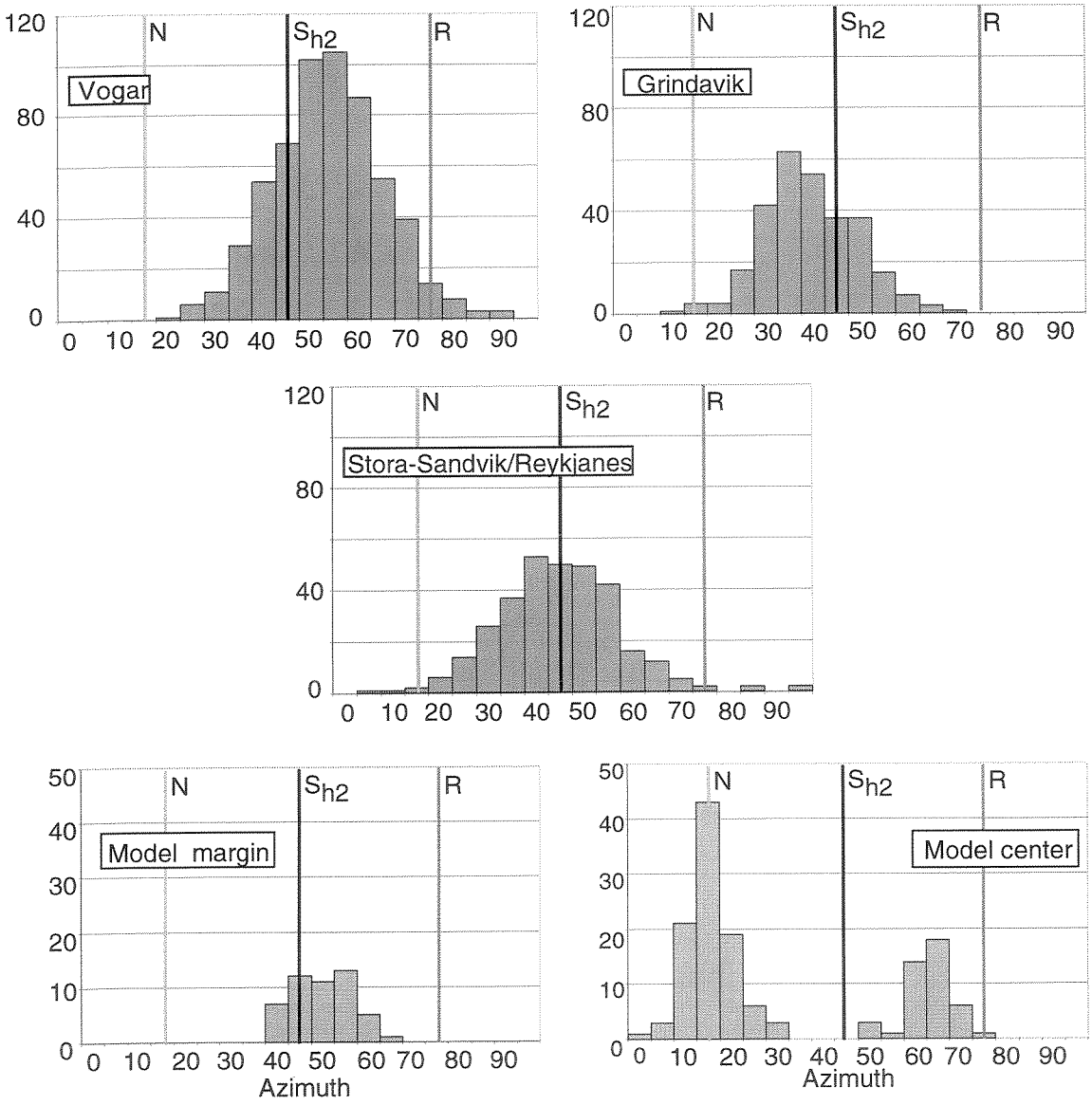


Fig. 3.16. Histograms of azimuth for data from air photos and $\alpha = 30°$ model. N is the displacement-normal direction, S_{h2} is the direction of the minimum horizontal stress within the rift zone (perpendicular to E_{hmax}) and R is the trend of the rift zone.

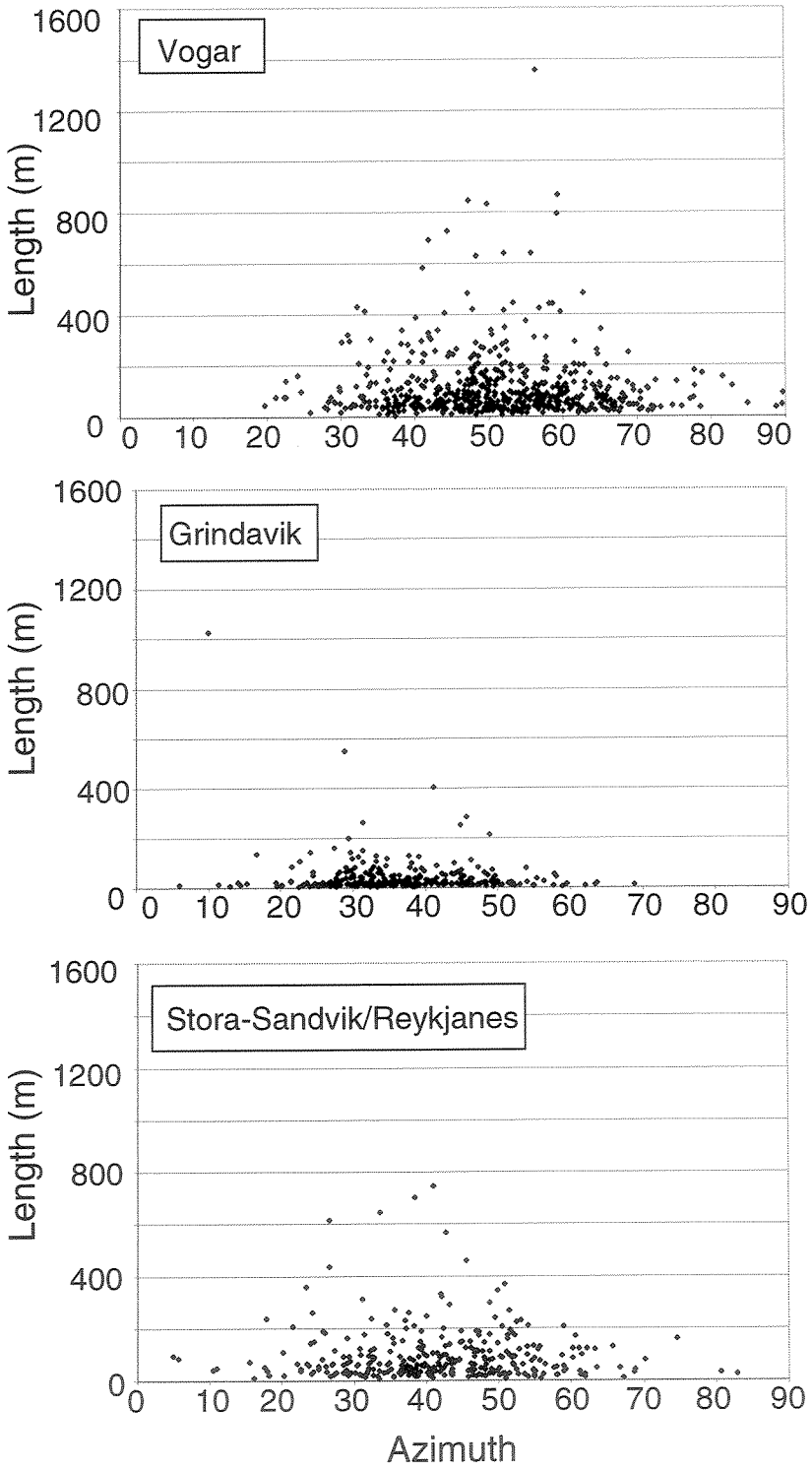


Fig. 3.17 - Plots of length vs. azimuth for data from air photos.

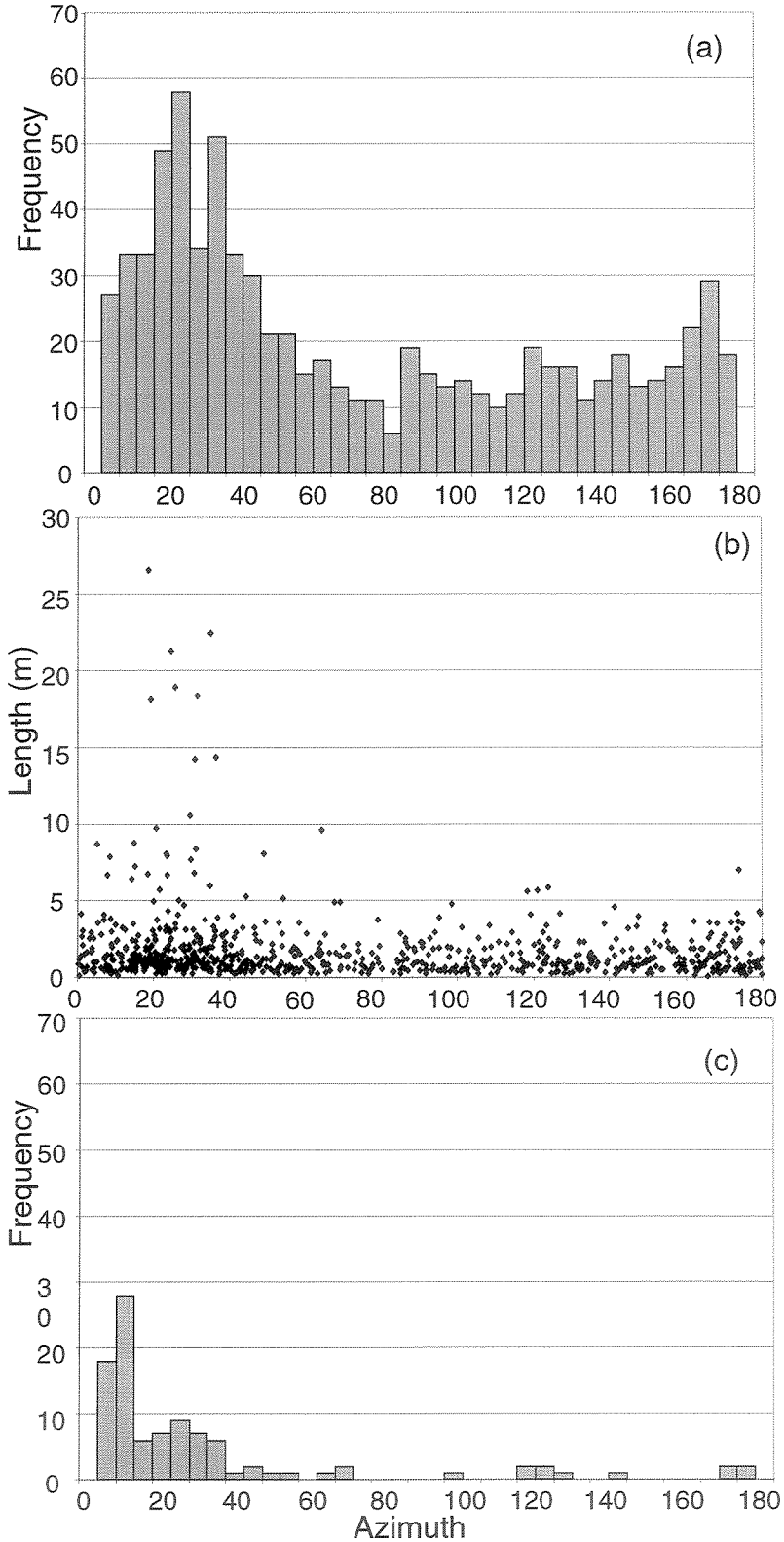


Fig. 3.18 - a) Histogram of azimuths for data from Molvik. b) Plot of length vs. azimuth for data from Molvik. c) Histogram of azimuth for fractures at Molvik greater than 4 meters in length.

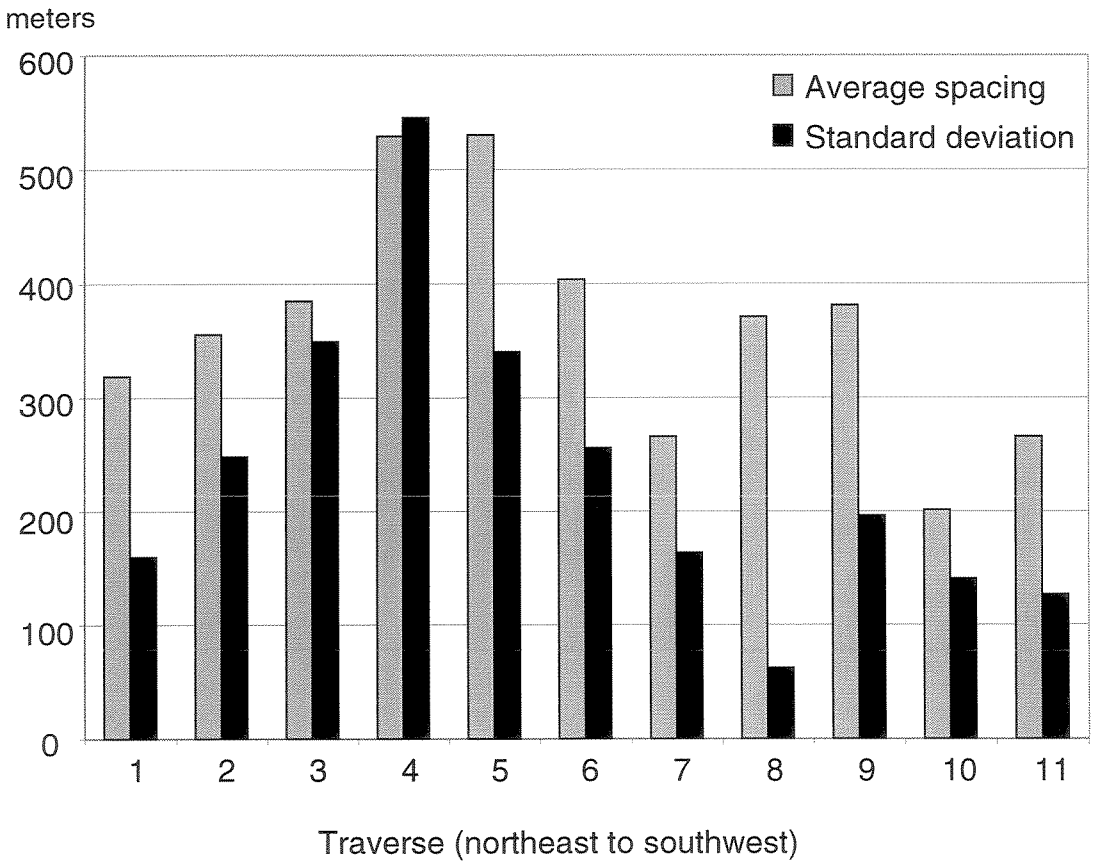


Fig. 3.19 - Graph showing fracture spacing and standard deviation of fracture spacing for the Vogar photomosaic. Measurements were made along 11 transects oriented perpendicular to the average trend of fissures, and spaced approximately 500 meters apart.

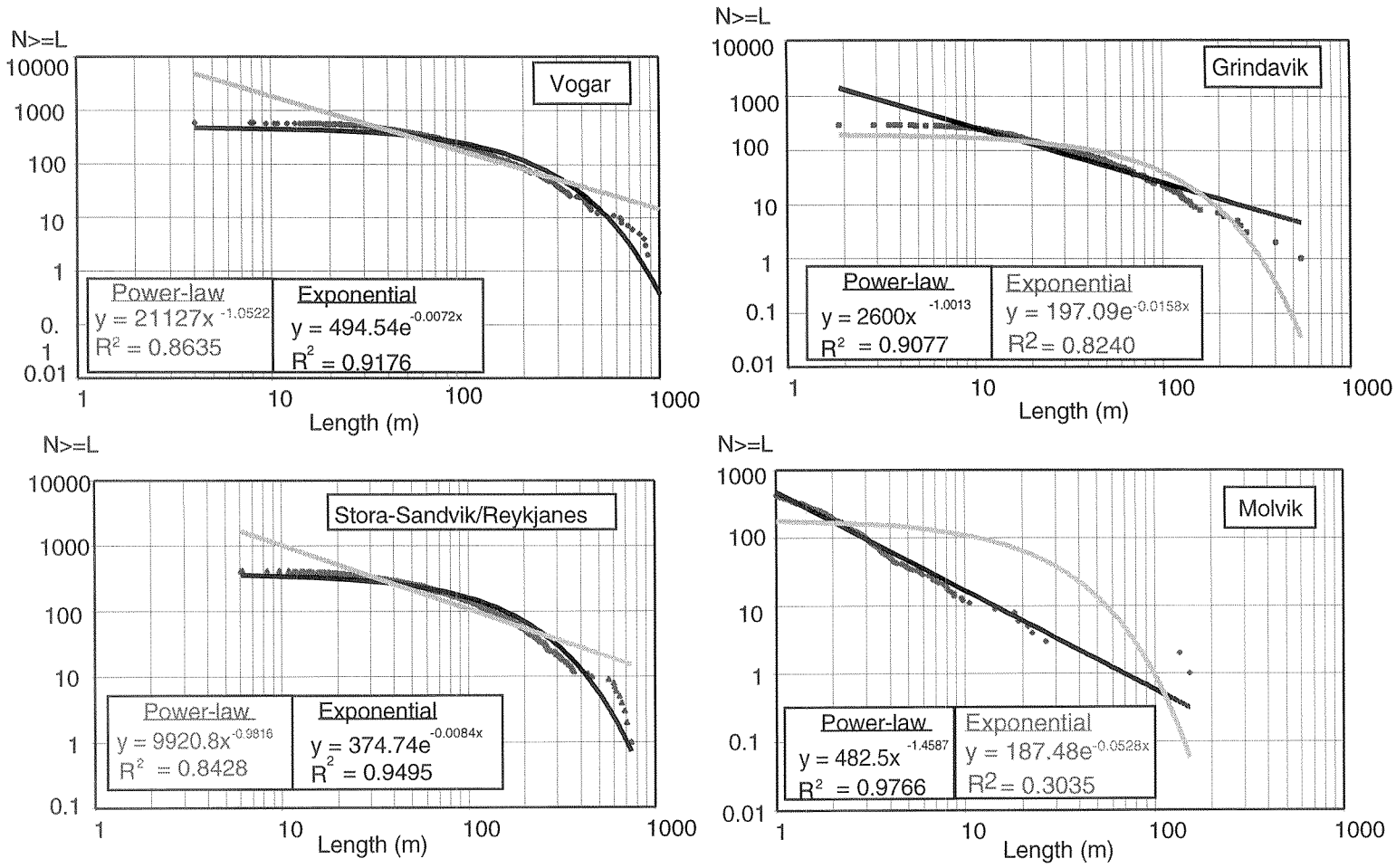


Fig 3.20 - Log-log plots of cumulative frequency of fracture lengths for data from air photos and field data from Molvik. Least squares fit for both power-law and exponential curves are shown. The best fit curve is indicated in black, and the other is grey.

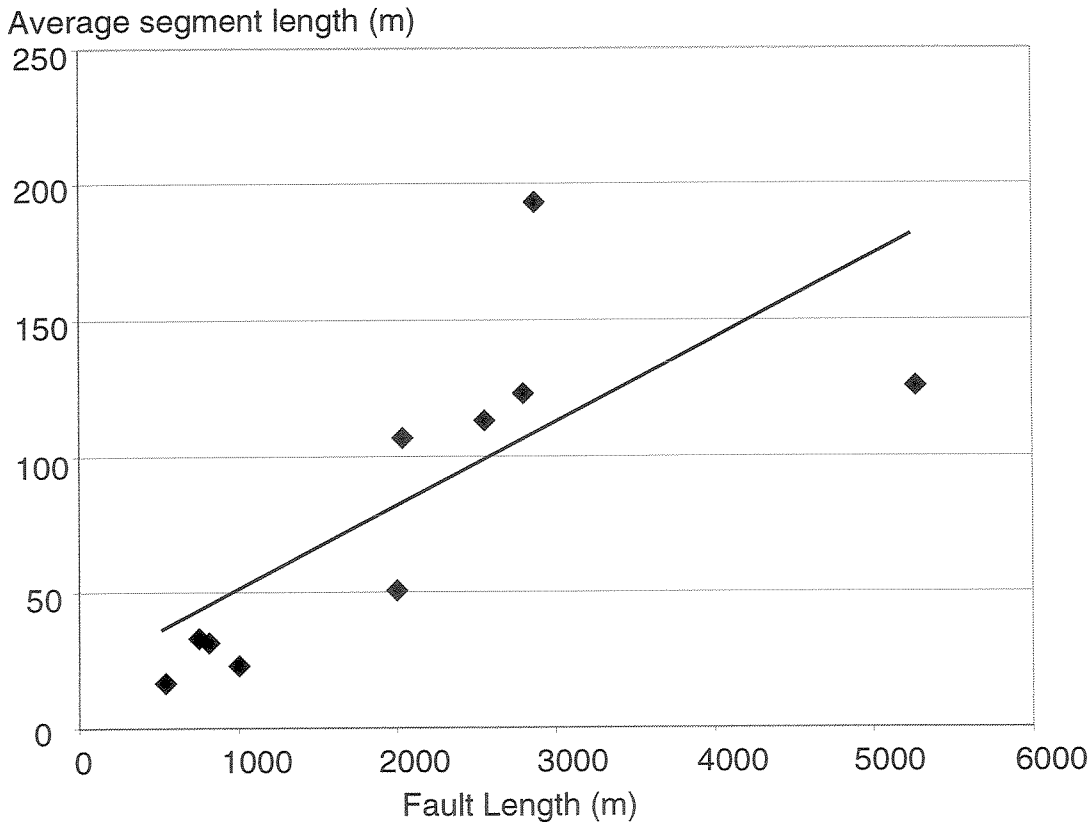


Fig. 3.21 - Plot of segment length vs. total fracture length for the three longest fractures on each air photo.

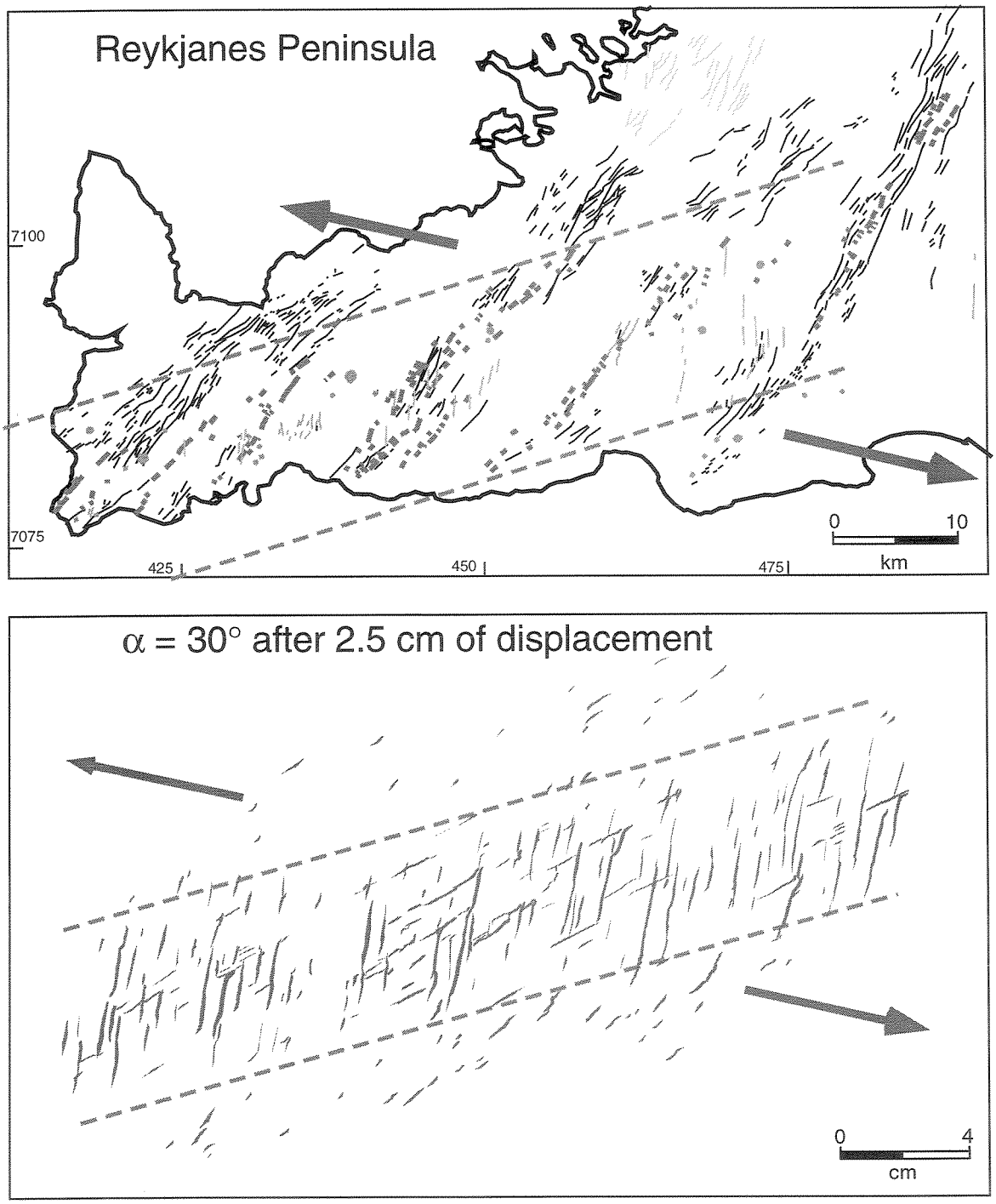


Fig. 3.22 - Tectonic map of Reykjanes Peninsula and fault trace map for $\alpha = 30°$ after 2.5 cm of displacement and rotated 15° clockwise. Arrows show the displacement direction. Dashed lines mark approximate locations of the edge of the zone of volcanic acitivity and the latex sheet respectively. Symbols on Reykjanes map same as in Fig.3.2

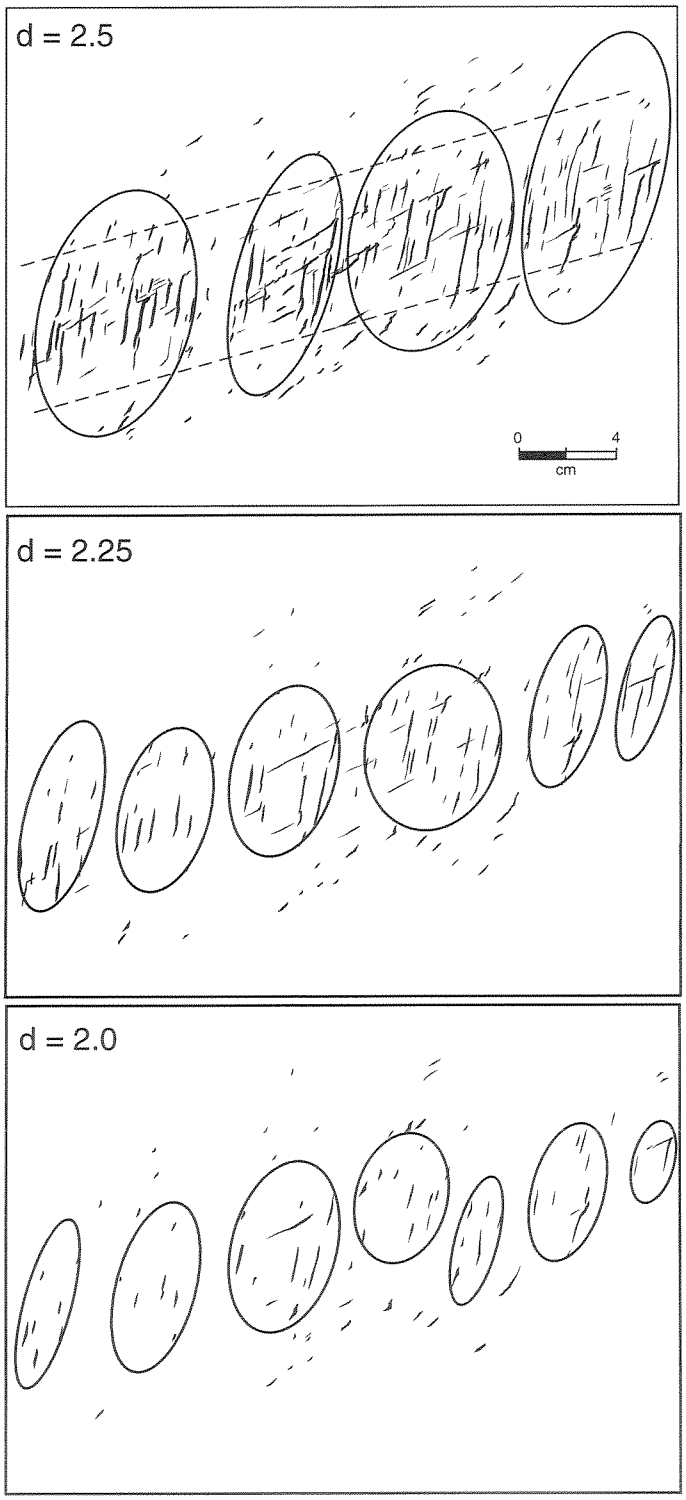


Fig. 3.23 Fault trace maps for the $\alpha = 30°$ model at 2.0, 2.25 and 2.5 cm of displacement. Ellipses surround clusters of faults. See text for further discussion.

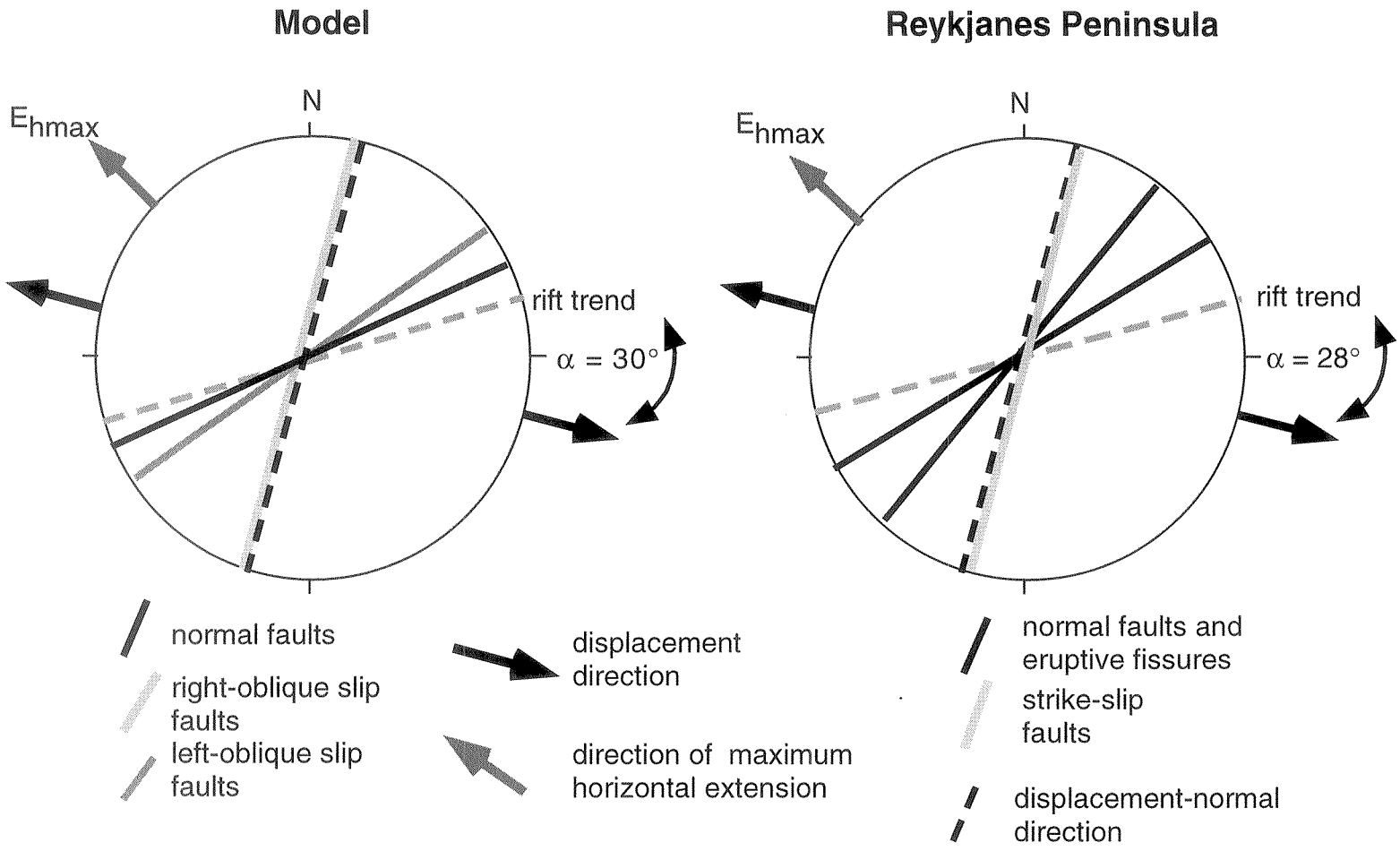


Fig. 3.24 - Summary of average tectonic trends for the $\alpha = 30°$ model and Reykjanes Peninsula.

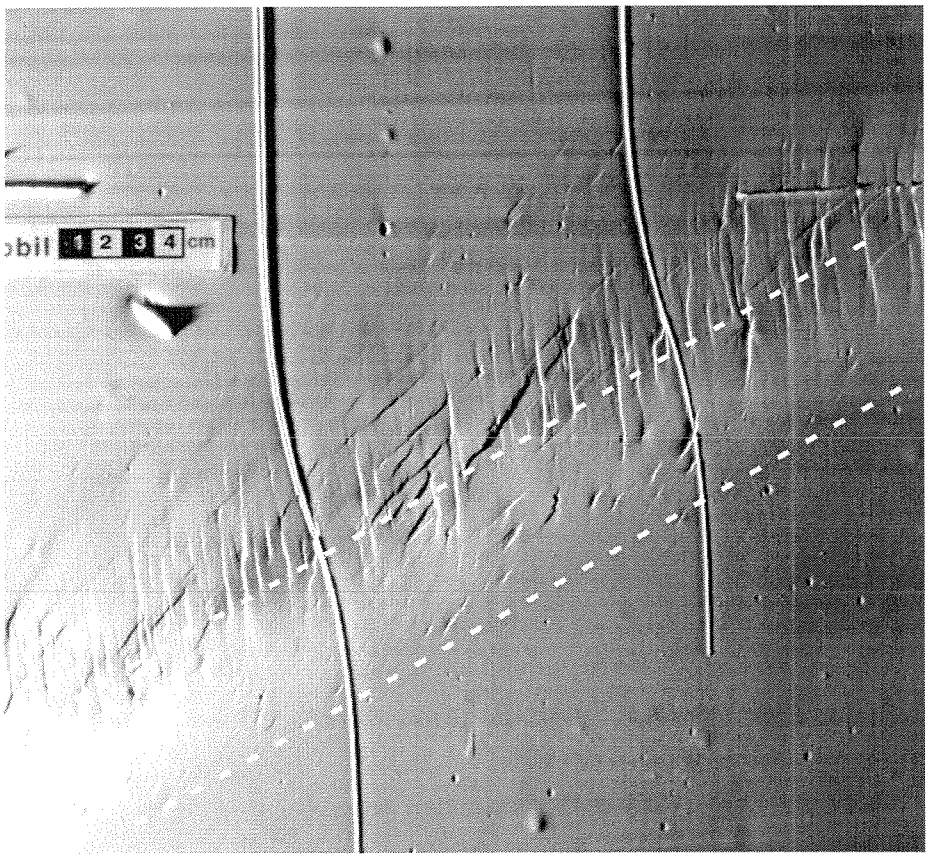


Fig. 3.25 - Close-up of flexure forming in the α= 30° model. Dashed lines enclose the area of flexure on the bottom half of the rift zone. Flexure is less well developed on the top half and does not show up well on the photo show here.

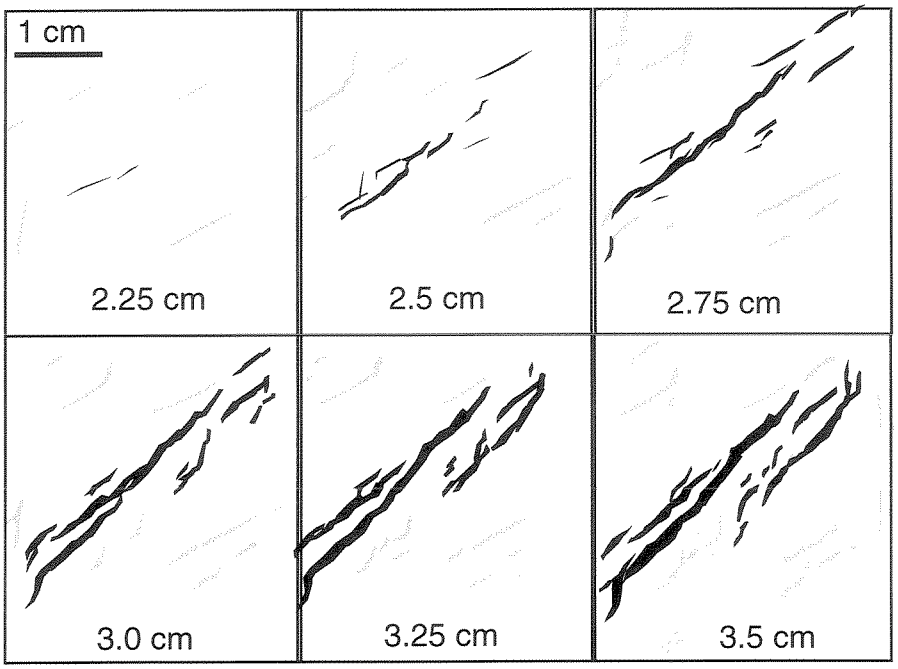


Fig. 3.26 - Detail from fault trace maps for the $\alpha = 30°$ model between 2.25 and 3.5 cm of displacement. Shown in black are left lateral oblique-slip faults linking and rotating to become large-displacement normal faults. Faults shown in grey do not grow significantly during the same time period.

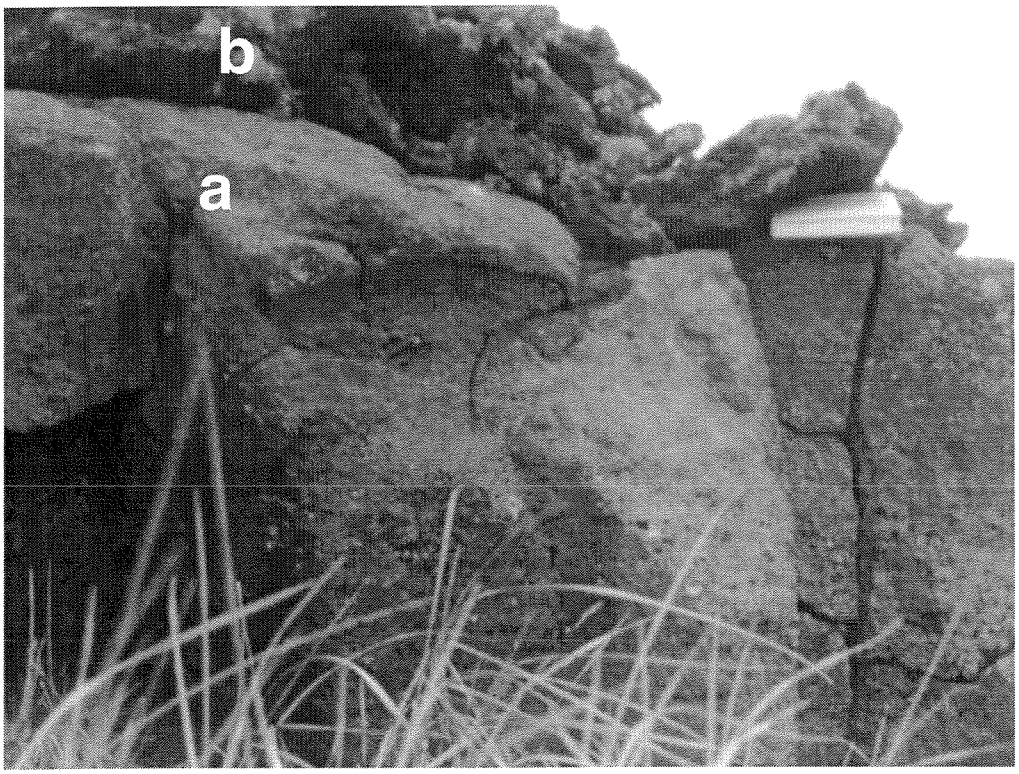


Fig. 3.27 - Photograph of a) a thin fissure-erupted lava flow (approximately 2000 ybp) and b) a thick pahoehoe flow from the Sandfellshaed shield (approximately 12,500 ybp), both cut by a northeast striking normal fault. Field evidence indicates the fault was present when flow b) erupted and was subsequently reactivated.

Epilogue

No scientific research is ever complete, and this body of work is no exception. Many questions have been raised as a result of this study and possibilities for future work are plentiful. Results of Chapter 1 suggest that one or more of the constant boundary conditions in the modeling process is controlling the characteristic length of fault segments, whereas rift obliquity controls how segments link. Boundary conditions that can be tested include width of the latex sheet, rate of displacement of the moving wall, thickness of the clay layer and strength of the clay. The latter can be accomplished by using the same batch of clay for all experiments, but varying the amount of water added for each model.

The discrepancy between imposed extensional strain and fault related strain remains puzzling, and further investigation using the experimental models can be done. More accurate measurements of fault dip could be obtained if it were possible to calibrate images of the model surface. This would also make it possible to determine how length/displacement scaling varies with α. It would be of interest to see how the proportion of "hidden extension" changes during the evolution of the model. It would also be useful to run layered models and examine serial sections, both horizontal and vertical, to look for small faults that have not propagated to the surface and to look at continuous deformation related to folding.

Results of Chapter 2 suggest that faults tend to cluster very early during fault nucleation, but it is not clear whether this is always true or if it was only a random occurrence in these particular models. Existing photographs of other models should be

examined to see if this is a common occurrence, and a way to better quantify the amount of clustering should be developed. If clustering is indeed a common occurrence in all of the models, then we need to determine whether or not it is due to unwanted edge effects at the base of the model, such as folding of the latex sheet during extension. In addition, data from Chapter 2 can be used to determine how cumulative size distributions change with strain.

Several aspects of the work from Chapter 3 bear further investigation. Detailed data from this study come only from one of the fissure swarms on Reykjanes Peninsula. It would be of great importance to see if and how fracture population systematics vary along the axis of the Peninsula. It would also be useful to conduct similar studies in some of the other, less oblique volcanic zones in Iceland. Work in Iceland has shown that bookshelf faulting accommodates significant left-lateral strain both on Reykjanes Peninsula and in the South Iceland Seismic Zone. By varying the thickness of the clay layer in experimental models, we can try to answer the question why right-lateral strike slip faults are shorter on Reykjanes Peninsula than they are in the South Iceland Seismic Zone. We can also test to see whether the width of the deforming zone plays any role in the formation of these bookshelf faults.

Data from Chapter 3 indicate that the size distribution of faults differs between the margin and the center of oblique rifts. Fault trace maps from this study can be used to test this by separately analyzing data from faults on the margins and those in the center of the rift.

These are only a few of the many possibilities afforded by using experimental models of oblique rifting. The amount of work that remains to be done could provide data for countless dissertations.

APPENDIX A

Procedure for Orthorectification of Air Photos

The first step in the process was to make a Digital Elevation Model (DEM) of the area covered by the air photos. Digitized topographic maps in ArcInfo format were obtained from Landmælingar Íslands, The Icelandic Geodetic Survey. Only the 20-meter contours had correct elevation values. The 5-meter contours were incomplete and had not been assigned elevation values.

For the Vogar area, I cleaned up and assigned elevation values to all 5-meter contours, using ArcInfo software (Arc Info version 7.2 ESRI Corporation) and a paper map as reference, so that a high resolution DEM could be made. For the other two photo pairs I deleted the 5-meter contour lines and used only 20-meter contours to make the DEM. This was justified because the study areas have generally low topographic relief and little accuracy would be gained by digitizing the 5-meter contours. I used the TOPOGRID aml script within ArcInfo to make the DEM. Drainage features were not taken into account and the grid output cell size used was 10 meters per pixel. The DEM was then imported into ERDAS Imagine for use in the orthorectification process. Topographic maps at a scale of 1:25000 were obtained from the Iceland Geodetic Survey and scanned on a flat bedscanner for all three field areas. Only the parts of the map that included the study area were scanned. Scanned maps were then georeferenced by keyboarding in ground control points (GCPs) that consisted of coordinates that were clearly marked on the map grid. A second order polynomial model was used to resample

the image. The map projection used by Landmælingar for their 1:25000 maps is Transverse Mercator Gauss-Kreuger, and the Spheroid is International 1909.

Black and white air photos obtained from Landmaelingar Islands were scanned at 600 dpi on a flatbed scanner and saved as TIFF files. These were imported into ERDAS Imagine (version 8.3.1. ERDAS Inc. Atlanta, Ga.) and opened as Imagine raster files.

I followed the step by step procedure outlined for rectifying camera images in the Imagine Tour Guide (1997) manual on page 215. I used a minimum of eight ground control points for each photo and sampled the image with a second order polynomial camera model. Output cell size was 1 meter per pixel. GCPs were collected from the scanned topographic map. Whenever possible, easily identified man-made features were used as GCPs. However, there are few man-made features in this part of Iceland, so that most GCPs were, by necessity, distinctive topographic features.

Once orthorectified, the two photos were made into a photo-mosaic following the procedure outlined in the Imagine Tour Guide (1997) on p. 235

REFERENCES

Ackermann, R.V., and Schlische, R.W., 1997, Anticlustering of small normal faults around larger faults: Geology 25, 1127-1130.

Ackermann, R.V., Schlische, R.W., and Withjack, M.O., 1997, Systematics of an evolving population of normal faults in scaled physical models: Geological Society of America Abstracts with programs, A-198.

Ackermann, R.V., Withjack, M.O. and Schlische, R.W., 2000, The geometric and statistical evolution of normal fault systems: an experimental study of the effects of mechanical layer thickness on scaling laws: Journal of Structural Geology (in review).

Angelier, J., and Bergerat, F., 1983, Systemes de contrainte et extension intracontinentale. Societe Nationale Elf Acquitaine (Production), F-64018, p. 137-147.

Applegate, B. and Shor, A.N., 1994, The northern Mid-Atlantic and Reykjanes Ridges: spreading center morphology between 55°50'N and 63°00'N. Journal of Geophysical Resaerch 99, 17,935-17,956.

Aviles, C.A., Scholz, C.H., and Boatwright, J., 1987, Fractal analysis applied to characteristic segments of the San Andreas Fault. Journal of Geophysical Research 92, 331-344.

Aydin, A., and Schultz, R.A., 1990, Effect of mechanical interaction on the development of strike-slip faults with echelon patterns: Journal of Structural Geology 12, 123-129.

Bjarnason, I. Th., Cowie, P.A., Anders, M.H., Seeber, L., and Scholz, C.H., 1993, The 1912 Iceland Earthquake rupture:growth and developmenet of a nascent transform system: Bulletin of the Seismological Society of America 83, 416-435.

Bowman, D.D., Ouillon, G., Sammis, C.G., Sornette, A., and Sornette, D., 1998, An observational test of the critical earthquake concept. Journal of Geophysical Research 103, p.24,359-24,372.

Carbotte, S.M., and Macdonald, K., 1994, Comparison of seafloor tectonic fabric at intermediate, fast and super fast spreading ridges: Influence of spreading rate, plate motions and ridge segmentation on fault patterns: Journal of Geophysical Research 99, 13,609-13,631.

Cartwright, J.A., Trudgill, B.D., and Mansfield, C.S., 1995, Fault growth by segment linkage: an explanation for scatter in maximum displacement and trace length data from the Canyonlands: Journal of Structural Geology 17, 1319-1326.

Chadwick, W.W. Jr., and Embley, R.W.,1998, Graben formation associated with recent dike intrusions and volcanic eruptions on the mid-ocean ridge: Journal of Geophysical Research 103, 9807-9825.

Chorowicz, J., and Sorlien, C., 1992, Oblique extensional tectonics in the Malawi Rift, Africa:Geological Society of America Bulletin 104, 1015-1023.

Cladouhos, T.T., and Marrett, R., 1996, Are fault growth and linkage models consistent with power-law distributions of fault lengths?: Journal of Structural Geology 18, 281-293.

Clifton, A.E., 1987, Tectonic analysis of the western border fault zone of the Mesozoic Hartford Basin, Connecticut and Massachusetts, M.A. thesis, Wesleyan University.

Clifton, A.E., and Schlische, R.W. 1997, Using scaled physical models of oblique deformation to analyze the spatial and temporal evolution of fault systems: Geological Society of America Abstracts with Programs, A-258.

Clifton, A.E., R.W. Schlische, M.O. Withjack, and R.V. Ackermann, 2000, Influence of rift obliquity on fault-population systematics: results of experimental clay models: Journal of Structural Geology, in press.

Clifton, A.E., Schlische, R.W., M.O. Withjack, and Ackermann, R.V. 1998, Using Scaled Physical Models of Oblique Extension to Study the Temporal Evolution of Segmented Fault Systems: EOS Transactions 79, F648.

Courtillot, V. Tapponier, P. and Varet, J., 1974, Surface features associated with transform faults: a comparison between observed examples and an experimental model: Tectonophysics 24, 317-329.

Cowie, P.A., 1998a, A healing-reloading feedback control on the growth rate of seismogenic faults: Journal of Structural Geology 20, 1075-1087.

Cowie, P.A., 1998b, Normal fault growth in three dimensions in continental and oceanic crust. In: Buck, W.R., Delaney, P.T., Karson, J.A. and Lagabrielle, Y. (eds) Faulting and Magmatism at Mid-Ocean Ridges, Geophysical Monograph 106, American Geophysical Union.

Cowie, P.A., and Scholz, C.H., 1992, Physical explanation for displacement-length relationship of faults using a post-yield fracture mechanics model: Journal of Structural Geology 14, 1133-1148.

Cowie, P.A, Knipe, R.J., and Main, I.G., 1996, Introduction to the Special Issue: Journal of Structural Geology 18, v-xi.

Cowie, P.A., Sornette, D., and Vanneste, C., 1995, Multifractal scaling properties of a growing fault population: Geophysical Journal International 122, 457-469.

Cowie, P.A., Scholz, C.H., Edwards, M., and Malinverno, A., 1993a, Fault strain and seismic coupling on mid-ocean ridges: Journal of Geophysical Research 98, 17,911-17,920.

Cowie, P.A., Vanneste,C., and Sornette, D., 1993b, Statistical physics model for the spatiotemporal evolution of faults: Journal of Geophysical Research 98, 21,809-21,821.

Dauteuil, O., and Brun, J.-P., 1993, Oblique rifting in a slow-spreading ridge: Nature 361, 145-148.

Dauteuil, O., and Brun, J.-P., 1996, Deformation partitioning in a slow spreading ridge undergoing oblique extension: Mohns Ridge, Norwegian Sea. Tectonics 15, 870-884.

Davy, P., 1993, On the frequency-length distribution of the San Andreas Fault System. Journal of Geophysical Research 98, 12,141-12,151.

Dawers, N.H., 1996, Observations of fault growth scaling relations. Ph.D. thesis, Columbia University.

deBoer, J.Z., and Clifton, A.E., 1988, Mesozoic tectogenesis: development and deformation of 'Newark' rift zones in the Appalachians (with special emphasis on the Hartford basin, Connecticut). In: W. Manspeizer (Ed.), Developments in Geotectonics 22, Triassic - Jurassic Rifting, Continental Breakup and the Origin of the Atlantic and Passive Margins, Part A. Elsevier. pp. 275-302 (*published as deBoer and Clifford, due to editing error).

DeMets, C., Gordon, R., Argus, D. and Stein, S., 1994, Effect of recent revisions to the geomagnetic reversal time scalel on estimates of current plate motions: Geophysical Research Letters 21, 2191-2194.

Einarsson, P., 1991, Earthquakes and present-day tectonism in Iceland: Tectonophysics 189, 261-279.

Einarsson, P., and Brandsdottir, B., 1980, Seismological evidence for lateral magma intrusion during the July 1978 deflation of the Krafla volcano in NE Iceland: Journal of Geophysics 47, 160-165.

Einarsson, P., and Eiriksson, J., 1982, Earthquake fractures in the districts Land and Rangárvellir in the south Iceland seismic zone: Jökull 32, 113-120.

Einarsson, P., and Saemundsson, K., 1987, Earthquake epicenters 1982-1987 and volcanic systems in Iceland (map). In: Í hlutarins edli, Thortsteinn I.Sígfusson (ed) Menningarsjódur, Reykjavik.

Eisenstadt, G., and Withjack, M.O., 1995, Estimating inversion: results from clay models: Geological Society of London Special Publication 88, 119-136.

Eyolfsson, V., 1998, Kortlagning sprungna og nútíma eldvarpa í Fagradalsfjalli á vestanverðum Reykjanesskaga (Mapping of fractures and Holocene volcanic vents in Fagradalsfjall, Western Reykjanes Peninsula. In Icelandic). B.Sc. thesis, University of Iceland, Department of Geology and Geography, 70 pp.

Faerseth, R.B., Knudsen, B.-E., Liljedahl, T., Midbøe, P.S., and Søderstrøm, B., 1997, Oblique rifting and sequential faulting in the Jurassic development of the northern North Sea: Journal of Structural Geology 19, 1285-1302.

Freed, A.M., and Lin, J., 1998, Time-dependent changes in failure stress following thrust earthquakes: Journal of Geophysical Research 103, p.24,393-24,409.

Gudmundsson, A., 1980, The Vogar fissure swarm, Reykjanes Peninsula, SW-Iceland: Jökull 30, 43-63.

Gudmundsson, A., 1986, Mechanical aspects of postglacial volcanism and tectonics of the Reykjanes Peninsula, SW Iceland. Joural of Geophysical Research 91, 12,711-12,721.

Gudmundsson, A., 1987a, Tectonics of the Thingvellir fissure swarm, SW Iceland. Journal of Structural Geology 9, 61-69

Gudmundsson, A., 1987b, Geometry, formation and development of tectonic fractures on the Reykjanes Peninsula, Southwest Iceland: Tectonophysics, v.139, p.295-308.

Gudmundsson, A., 1992, Formation and growth of normal faults at the divergent plate boundary in Iceland: Terra Nova 4, 464-471.

Gupta, A. and Scholz, C.H., 2000, A model of normal fault interaction based on observations and theory: Journal of Geophysical Research, in press.

Hackman, M.C., King, G.C.P. and Bilham, R., 1990, The mechanics of the south Iceland seismic zone: Journal of Geophysical Research 95, 17,339-17,351.

Hardebeck, J.L., Nazareth, J.J. and Hauksson, E., 1998, The static stress change triggering model: Contraints from two southern California aftershock sequences: Journal of Geophysical Research 103, p.24,427-24,437.

Hatton, C.G., Main, I.G., and Meredith, P.G., 1994, Non-universal scaling of fracture length and opening displacement: Nature 367, 160-162.

Hirata, T., 1989, Fractal dimension of fault systems in Japan: Fractal structure in rock fracture geometry at various scales: PAGEOPH 131, 157-170.

Hreinsdottir, S., 1999, GPS geodetic measurements on the Reykjanes Peninsula, SW Iceland: crustal deformation from 1993 to 1998. M.Sc. Thesis, University of Iceland, 114 pp.

Hreinsdottir, S., Einarsson, P., and Sigmundsson, F., 1999, Crustal deformation at the oblique Reykjanes Peninsula plate boundary, SW-Iceland, 1993-1998, observed with GPS geodetic measurements: EOS Transactions 80, S340.

Hubbert, M. K., 1937, Theory of scale models as applied to the study of geologic structures: Geological Society of America Bulletin 48, 1459-1520.

Jackson, J.A, and White, N.J., 1989, Normal faulting in the upper continental crust: observations from regions of active extension. Journal of Structural Geology 11, 15-36.

Jaumé, S.C., and Sykes, L.R., 1992, Changes in the state of stress on the southern San Andreas fault resulting from the California earthquake sequence of April to June 1992: Science 258, p.1325-1328.

Jeffris, R.G., and Voight, B.,1981, Fracture analysis near the mid-ocean plate boundary, Reykjavik-Hvalfjördur area, Iceland: Tectonophysics 76, 171-236.

Johannesson, H., 1980, Jardlagaskipan og thróun rekbelta á Versturlandi (Evolution of rift zones in western Iceland, in Icelandic with English summary). Náttúrufraedingurinn 50, 13-31.

Jonsson, J., 1978, Jardfraedikort af Reykjanesskaga (Report on the geology of Reykjanes Peninsula) in Icelandic. Orkustofnun report OS-JHD-7831, Reykjavik.

Kautz, S.A., and Sclater, J.G., 1988, Internal deformation in clay models of extension by block faulting: Tectonics 7, 823-832.

Klein, F.W, Einarsson, P. and Wyss, M., 1977, The Reykjanes Peninsula, Iceland earthquake swarm of September 1972 and its tectonic significance: Journal of Geophysical Research 78, 5084-5099.

Lindholm, R.C., 1978, Triassic-Jurassic faulting in eastern North America- a model based on pre-Triassic structures: Geology 6, 365-368.

Macdonald, K., 1998, Linkages between faulting, volcanism, hydrothermal activity and segmentation on frast spreading centers. In: Buck, W.R., Delaney, P.T., Karson, J.A. and Lagabrielle, Y. (eds) Faulting and Magmatism at Mid-Ocean Ridges, Geophysical Monograph 106, American Geophysical Union, pp.27-58.

Main, I., 1996, Statistical physics, seismogenesis, and seismic hazard: Reviews of Geophysics, v. 34, p. 433-462.

Malinverno, A., 1993, Transition between a valley and a high at the axis of mid-ocean ridges: Geology, v.21, p.639-642.

McAllister, E., Cann, J., and Spencer, S., 1995, The evolution of crustal deformation in an oceanic extensional environment: Journal of Structural Geology 17, 183-199.

McClay, K.R., and White, M.J., 1995, Analogue modelling of orthogonal and oblique rifting. Marine and Petroleum Geology 12, 147-151.

Morley, C.K., 1995, Developments in the structural geology of rifts over the last decade and their impact on hydrocarbon exploration. In: Lambiase, J.J., (ed.) Hydrocarbon Habitat in Rift Basins, Geological Society Special Publication no. 80, pp. 1-32.

Moustafa, A.D., 1996, Internal structure and deformation of an accommodation zone in the northern part of the Suez rift: Journal of Structural Geology 18, 93-107.

Murton, B.J., and Parson, L.M., 1993, Segmentation, volcanism and deformation of oblique spreading centers: a quantitative study of the Reykjanes Ridge: Tectonophysics 222, 237-257.

Mutter, J.C., and Karson, J.A., 1992, Structural Processes at slow-spreading ridges: Science 257, 627-634.

Nakamura, K., 1970, En echelon features of Icelandic ground fissures: Acta Naturalia Islandica, Vol. II, no.8, Reykjavik.

Okobu, P.G., and Aki, K., 1987, Fractal geometry in the San Andreas fault system: Journal of Geophysical Research 92, 345-355.

Peacock, D.C.P., and Sanderson, D.J., 1991, Displacements, segment linkage and relay ramps in normal fault zones: Journal of Structural Geology 13, 721-733.

Pickering, G., Bull, J.M., and Sanderson, D.J., 1995, Sampling power-law distributions: Tectonophysics, 248, 1-20.

Pollard, D.D., Delaney, P.T., Duffield, P.T., Endo, E.T. and Okamura, A.T., 1983, Surface deformation in volcanic rift zones: Tectonophysics 94, 541-584.

Rubin, A.M. 1990, A comparison of rift zone tectonics in Iceland and Hawaii: Bulletin of Volcanology 52, 302-319.

Rubin, A.M., 1992, Dike-induced faulting and graben subsidence in volcanic rift zones: Journal of Geophysical Research 97, 1839-1858.

Ryan, M.P., 1990. The physical nature of the Icelandic magma transport system. In: Ryan, M.P. (ed). Magma Transport and Storage, John Wiley & Sons, NY, p.175-224.

Saemundsson, K., 1979, Outline of the geology of Iceland: Jökull 29, 7-28.

Saemundsson, K., 1995, Svartsengi geological map (bedrock) 1:25000. Orkustofnun, Hitaveita Sudurnesja and Landmaelingar Islands. Reykjavik.

Saemundsson, K., and Einarsson, S., 1980, Geological map of Iceland, sheet 3, SW-Iceland, second edition. Museum of Natural History and the Iceland Geodetic Survey, Reykjavik.

Schlische, R.W., 1993, Anatomy and evolution of the Triassic-Jurassic continental rift system, eastern North America. Tectonics 12, 1026-1042.

Schlische, R.W., and Ackermann, R.V., 1998, Integrating computers into the field geology curriculum: Journal of Geoscience Education, 46, 30-40.

Schlische, R.W., and Anders, M.H., 1996, Stratigraphic effects and tectonic implications of the growth of normal faults and extensional basins. In: Beratan, K.K., (ed.), Reconstructing the Structural History of Basin and Range Extension Using Sedimentology and Stratigraphy: GSA Special Paper 303, pp. 183-203.

Schlische, R.W., Withjack, M.O., and Eisenstadt, G., 1999, An experimental study of the secondary fault patterns produced by oblique-slip faulting: EOS Transactions 80, S339.

Scholz, C.H., and Contreras, J.C., 1998, Mechanics of continental rift architecture: Geology 26, 967-970.

Searle, R.C., Keeton, J.A., Owens, R.B., White, R.S, Mecklenburgh, R., Parsons, B. and Lee, S.M., 1998, The Reykjanes Ridge: structure and tectonics of a hot-spot influenced, slow-spreading ridge, from multibeam bathymetery, gravity and magnetic investigations: Earth and Planetary Science Letters 160, 463-478.

Sempere, J-C., Purdy, G.M., and Schouten, H.,1990, Segmentation of the mid-Atlantic ridge between 24°N and 30°40'N: Nature 344, 427-431.

Sigmundsson, F. Einarsson, P., Bilham, R. and Sturkell, E., 1995, Rift-transorm kinematics in south Iceland: deformation from Global Positioning System measurements, 1986 to 1992: Journal of Geophysical Research 100, 6235-6248.

Sigurdsson, F. 1985, Jardvatn og vatnajardfraedi á utanverdum Reykjanesskaga. (in Icelandic). Orkustofnun Report OS-85075/VOD-06, Reykjavik

Sigursdsson, H. and Sparks, S.R.J., 1978, Lateral magma flow within rifted Icelandic crust: Nature 274, 126-130.

Sornette, D., Davy, P., and Sornette, A., 1990, Structuration of the lithosphere in plate tectonics as a self-organized critical phenomenon: Journal of Geophysical Research 95, 17,353-17,361.

Sturkell, E., Sigmundsson, F., Einarsson, P., and Bilham, R., 1994, Strain accumulation 1986-1992 across the Reykjanes Peninsula plate coundary, Iceland, determined from GPS measurements: Geophysical Research Letters 21, 125-128.

Takayasu, H., 1986, Pattern formation of dendritic fractals in fracture and electrical breakdown. In: L. Pietronero and E. Tosattic, editors, Fractals in Physics, Elsevier, pp. 181-184.

Taylor, B., Crook, K. and Sinton, J., 1994, Extensional transform zones and oblique spreading centers: Journal of Geophysical Research 99, 19,707-19,718.

Tron, V., and Brun, J.-P., 1991, Experiments on oblique rifting in brittle-ductile systems: Tectonophysics 188, 71-84.

Trudgill, B., and Cartwright, J., 1994, Relay ramp morphologies and normal fault linkages, Canyonlands National Park, Utah: Geological Society of America Bulletin 106, 1143-1157.

TruSoft International, 1997, Benoit v. 1.1, St. Petersburg, Florida..

Tuckwell, G.W., Bull, J.M. and Sanderson, D.J., 1996, Models of fracture orientation at oblique spreading centres: Journal of the Geological Society, London 153, 185-189.

Tuckwell, G.W., Bull, J.M. and Sanderson, D.J., 1998, Numerical models of faulting at oblique spreading centers: Journal of Geophysical Research 103, 15,473-15,482.

Umhoefer, P.J. and Stone, K.A., 1996, Description and kinematics of the SE Loreto basin fault array, Baja California Sur, Mexico: a positive field test of oblique-rift models: Journal of Structural Geology 18, p.595-614.

Vadon, H. and Sigmundsson, F., 1997, Crustal deformation from 1992 to 1995 at the Mid-Atlantic Ridge, Southwest Iceland, mapped by satellite radar interferometry: Science 275, 193-197.

Vogt, P.R., 1986, The present plate boundary configuration. In: Vogt., P.R., Tucholke, B.E., editors, The Geology of North America, Volume M, The Western North Atlantic Region.Geological Society of America, pp.189-204.

Ward, P.L., 1971, New interpretation of the geology of Iceland: Geological Society of America Bulletin 82, 2991-3012.

Whitlock, J.S., 1999, The tectonic geomorphology of the Molvik graben, Reykjanes Peninsula, Iceland. B.S. Thesis, Cook College, Rutgers University.

Willemse, E.J.M., 1997, Segmented normal faults: Correspondence between three-dimensional mechanical models and field data: Journal of Geophysical Research 102, 675-692.

Withjack, M.O. and Callaway, J.S., 2000, Active normal faulting beneath a salt layer: An experimental study of deformation in the cover sequence: American Association of Petroleum Geologists Bulletin, in press.

Withjack, M.O., and Jamison, W.R., 1986, Deformation produced by oblique rifting: Tectonophysics 126, 99-124.

Withjack, M.O., Schlische, R.W., and Olsen, P.E., 1998, Diachronous rifting, drifting and inversion on the passive margin of eastern North America: An analog for other passive margins: American Association of Petroleum Geologists Bulletin 82, 817-835.

Wojtal, S.F., 1996, Changes in fault displacement populations correlated to linkage between faults: Journal of Structural Geology 18, 265-279.

Wolfe, C.J., Bjarnason, I.Th., VanDecar, J.C., and Solomon, S.C., 1997, Seismic structure of the Iceland mantle plume: Nature 385, 245-247.

Wright, D., 1998, Formation and development of fissures at the East Pacific Rise: implications for faulting and magmatism at mid-ocean ridges. In: Buck, W.R., Delaney, P.T., Karson, J.A. and Lagabrielle, Y. (eds) Faulting and Magmatism at Mid-Ocean Ridges, Geophysical Monograph 106, American Geophysical Union. pp.137-152.

CURRICULUM VITAE
AMY ELIZABETH CLIFTON

EDUCATION

Institution and Location	Degree/Year Conferred		Field of Study
Rutgers University, New Brunswick, NJ	Ph.D.	2000	Structure/Tectonics
Wesleyan University, Middletown, CT	M.A.	1987	Structure/Tectonics
Central CT State University, New Britain, CT	B.A.	1982	Geology

POSITIONS HELD

1999-2000: Fulbright Fellow, Nordic Volcanological Institute, Reykjavik, Iceland.
1996-1999: Teaching Assistant, Rutgers University
1986-1996: Teacher, Renbrook School, West Hartford, CT
1987-1991: Project Adventure Instructor
1993-1996: Adjunct Lecturer, Western Connecticut State University
1985-1986: Teacher of Earth Science, Farmington High School, Farmington, CT

PUBLICATIONS

Clifton, Amy E., Roy W. Schlische, Martha O. Withjack, Rolf V. Ackermann, 2000, Influence of rift obliquity on fault-population systematics: results of experimental clay models. Journal of Structural Geology, in press

Clifton, A. E., 1999, Spatial distribution of fractures in the Reykjanes Fissure Swarm; comparison with scaled experimental models: EOS, Transactions, American Geophysical Union 1999 Fall Meeting, v.80, F970

Clifton, A.E., R.W. Schlische, M.O.Withjack and R.V.Ackerman, 1999, Nucleation, growth, and linkage of faults in oblique rift zones: results from scaled clay models: EOS, Transactions, American Geophysical Union 1999 Spring Meeting, v.80, S-340

Clifton, A.E., Schlische, R.W., Withjack, M.O. and Ackermann, R.V., 1998, Using scaled physical models of oblique extension to study the temporal evolution of segmented fault systems: EOS, Transactions, v.79, F648-649.

Clifton, A.E. and Schlische, R.W., 1998, Fracture population systematics of an oblique rift zone: field mapping and air photo analysis of the Reykjanes fissure swarm, Iceland: EOS, Transactions, v.79, p. S-231

Clifton, A.E. and Schlische, R.W. 1997, Using scaled physical models of oblique deformation to analyze the spatial and temporal evolution of fault systems: GSA Abstracts with Programs, v.29, p.A-258

DeBoer, J.Z. and Clifton, A.E., 1988. Mesozoic tectogenesis: development and deformation of 'Newark' rift zones in the Appalachians (with special emphasis on the Hartford basin, Connecticut). In *Developments in Geotectonics 22* , W. Manspeizer (Editor) *Triassic - Jurassic Rifting, Continental Breakup and the Origin of the Atlantic and Passive Margins, Part A.* Elsevier. (*published as deBoer and Clifford, due to editing error)